Central molecular zones in galaxies: 12CO-to-13CO ratios, carbon budget, and X factors

Israel, F.P.

Citation

Israel, F. P. (2020). Central molecular zones in galaxies: 12CO-to-13CO ratios, carbon budget, and X factors. *Astronomy And Astrophysics*, *635*, A131. doi:10.1051/0004-6361/201834198

Version: Accepted Manuscript
License: Leiden University Non-exclusive license
Downloaded from: https://hdl.handle.net/1887/3134290

Note: To cite this publication please use the final published version (if applicable).

Astronomy & Astrophysics manuscript no. 34198corrac
January 15, 2020

©ESO 2020

Central molecular zones in galaxies: ^{12}CO-to- ^{13}CO ratios, carbon budget, and X factors

F.P. Israel[1]

Sterrewacht Leiden, P.O. Box 9513, 2300 RA Leiden, the Netherlands

Accepted December 19. 2019

arXiv:2001.04975v1 [astro-ph.GA] 14 Jan 2020

ABSTRACT

We present ground-based measurements of 126 nearby galaxy centers in ^{12}CO and 92 in ^{13}CO in various low-J transitions. More than 60 galaxies were measured in at least four lines. The average relative intensities of the first four ^{12}CO J transitions are 1.00 : 0.92 : 0.70 : 0.57. In the first three J transitions, the average ^{12}CO-to- ^{13}CO intensity ratios are 13.0, 11.6, and 12.8, with individual values in any transition ranging from 5 to 25. The sizes of central CO concentrations are well defined in maps, but poorly determined by multi-aperture photometry. On average, the J=1-0 ^{12}CO fluxes increase linearly with the size of the observing beam, but CO emission covers only a quarter of the HI galaxy disks. Using radiative transfer models (*RADEX*), we derived model gas parameters. The assumed carbon elemental abundances and carbon gas depletion onto dust are the main causes of uncertainty. The new CO data and published [CI] and [CII] data imply that CO, C°, and C$^+$ each represent about one-third of the gas-phase carbon in the molecular interstellar medium. The mean beam-averaged molecular hydrogen column density is $N(\mathrm{H_2}) = (1.5 \pm 0.2) \times 10^{21}$ cm^{-2}. Galaxy center CO-to- H$_2$ conversion factors are typically ten times lower than the 'standard' Milky Way $X_\circ$ disk value, with a mean X(CO) = $(1.9 \pm 0.2) \times 10^{19}$ cm^{-2}/ K km s^{-1} and a dispersion 1.7×10^{19} cm^{-2}/ K km s^{-1}. The corresponding [CI]- H$_2$ factor is five times higher than X(CO), with X[CI] = $(9 \pm 2) \times 10^{19}$ cm^{-2}/ K km s^{-1}. No unique conversion factor can be determined for [CII]. The low molecular gas content of galaxy centers relative to their CO intensities is explained in roughly equal parts by high central gas-phase carbon abundances, elevated gas temperatures, and large gas velocity dispersions relative to the corresponding values in galaxy disks.

Key words. Galaxies: galaxies: centers – interstellar medium: molecules – millimeter lines – CO observations

1. Introduction

The aim of this paper is to determine the carbon budget and the amount of molecular hydrogen in the centers of nearby galaxies as accurately as possible, based on extensive new observations and current chemical and radiative transfer models. The bright inner disks of late-type galaxies contain massive concentrations of circumnuclear molecular hydrogen gas. These reservoirs feed central black holes, outflows, and bursts of star formation. Before their crucial role in inner galaxy evolution can be understood and evaluated, the physical characteristics of the gas must be determined. Cool and quiescent molecular hydrogen (H$_2$) gas is difficult to detect, and studies of the molecular interstellar medium (ISM) in galaxies rely on the observation of tracers such as continuum emission from thermal dust or line emission from the CO molecule. CO is one of the most common molecules in the ISM after H$_2$, even though its relative abundance is only about 10^{-5}. It has become the instrument of choice in the investigation of the molecular ISM because it is comparatively easy to detect and traces molecular gas already at low densities and temperatures.

Following the first detections in the mid-1970s, numerous galaxies have been observed in various transitions of CO and its isotopologue ^{13}CO. Substantial surveys have been conducted in the J=1-0 transition of ^{12}CO (e.g., Stark *et al.* 1987; Braine *et al.* 1993a; Sage 1993; Young *et al.* 1995; Elfhag *et al.* 1996; Nishiyama & Nakai 2001; Sauty *et al.* 2003; Albrecht *et al.* 2007; Kuno *et al.* 2007). These surveys sample the nucleus and sometimes also a limited number of disk positions. Extensive surveys in higher ^{12}CO transitions are fewer in number and usually only sample the nucleus (J=2-1; Braine *et al.* 1993a; Albrecht *et al.* 2007; J=3-2: Mauersberger *et al.* (1999); Yao *et al.* 2003; Mao *et al.* 2010). The survey by Dumke *et al.* (2001) and especially the James Clerk Maxwell Telescope (JCMT) legacy survey of nearby galaxies (NGLS: Wilson *et al.* 2012; Mok *et al.* 2016) are exceptional because they provide maps of almost 100 galaxies in the J=3-2 transition, many of them in the Virgo cluster. Specific surveys of Virgo cluster galaxies have also been published by Stark *et al.* (1986, J=1-0), Kenney and Young (1988, J=1-0), and Hafok & Stutzki (2003, J=2-1 and J=3-2).

The ^{12}CO lines in the survey are optically thick and cannot be used to measure molecular gas column densities or masses. Even the analysis of a whole ladder of multiple ^{12}CO transitions either fails to break the degeneracy between H$_2$ density, kinetic temperature, and CO column density and leaves the mass an undetermined quantity, or samples only a small fraction of the total gas content in the higher J transitions. Consequently, most molecular gas masses quoted in the literature are critically dependent on an assumed value for the relation between velocity-integrated CO line intensity and H$_2$ column density, $X_{\mathrm{CO}} = N(\mathrm{H_2})/I(\mathrm{CO})$. Unfortunately, this so-called X-factor does not follow from basic physical considerations. Instead, its empirically estimated value is rather sensitive to assumptions made in the process, and it varies depending on author and method. The most reliable method uses gamma-ray observations to trace hydrogen nuclei, and a useful overview of X values thus obtained can be found in Table E.1 of Remy *et al.* (2017). The empirically determined X values implicitly include both H$_2$ gas mixed with CO and H$_2$ gas that contains no

---

Send offprint requests to: F.P. Israel

Table 1. Galaxy sample

NGC	Dist.	lgFIR	lgL_{FIR}	D_{25}	NGC	Dist.	lgFIR	lgL_{FIR}	Size	NGC	Dist.	lgFIR	lgL_{FIR}	Size
IC	Mpc	Wm^{-2}	$L_{\odot}$	’	IC	Mpc	Wm^{-2}	$L_{\odot}$	’	IC	Mpc	Wm^{-2}	$L_{\odot}$	’
(1)	(2)	(3)	(4)	(5)	(1)	(2)	(3)	(4)	(5)	(1)	(2)	(3)	(4)	(5)
N 134	21.5	-11.88	10.26	8.1x2.6	N2993	35.9	-12.28	10.31	1.3x0.9	N4666	27.5	-11.74	10.62	4.6x1.3
N 253	3.4	-10.42	10.13	25x7.4	N3034	5.9	-10.28	10.74	11x4.3	N4736	4.8	-11.50	9.35	11x9.1
N 275	23.6	-12.56	9.67	1.5x1.1	N3044	20.4	-12.25	9.86	5.7x0.6	N4826*	3.8	-11.66	9.34	10x5.4
N 278	11.3	-11.87	9.76	2.2x2.1	N3079*	20.7	-11.60	10.51	7.9x1.4	N4835	23.9	-12.00	10.24	4.0x0.9
N 300	1.9	-11.77	8.26	22x16	I2554	16.4	-12.04	9.87	3.2x1.5	N4945*	4.4	-10.67	10.10	20x3.8
N 470	31.7	-12.44	10.04	2.8x1.7	N3175	13.6	-12.10	9.65	5.0x1.3	N5033*	17.2	-12.00	9.95	11x5.0
N 520	30.5	-11.79	10.66	4.5x1.8	N3227*	20.3	-12.32	9.77	5.4x3.6	N5055	8.3	-11.66	9.66	13x7.2
N 613	19.7	-11.90	10.17	5.5x4.2	N3256	37.0	-11.71	10.91	3.8x2.1	N5135*	57.7	-12.04	10.96	2.6x1.8
N 628	9.9	-12.60	8.87	11x9.5	N3281*	44.7	-12.50	10.28	3.3x1.8	N5194*	9.1	-11.59	9.81	11x6.9
N 660	12.2	-11.46	10.20	9.1	N3310	19.2	-11.79	10.26	3.1x2.4	N5218	46.5	-12.38	10.43	1.9x1.0
N 695	130	-12.36	11.35	0.8x0.7	N3351	9.0	-12.00	9.39	3.1x2.9	N5236	4.0	-11.22	9.46	13x12
N 891	9.4	-11.53	9.90	14x2.5	N3504	27.8	-11.98	10.39	2.7x2.2	Circ*	2.9	-10.92	9.48	6.9x3.0
N 908	19.9	-12.00	10.08	6.0x2.6	N3556	14.2	-11.81	9.97	8.7x2.2	N5433	67.8	-12.44	10.70	1.6x0.4
N 972	21.4	-11.75	10.39	3.4x1.7	N3593	5.6	-11.97	9.01	5.75	I4444	23.1	-11.95	10.26	1.7x1.4
Maff2	3.1	-11.23	9.23	5.8x1.6	N3620	20.4	-11.61	10.49	2.8x1.1	N5643*	14.4	-11.93	9.87	4.6x4.0
N1055	13.4	-11.84	9.89	7.6x2.7	N3621	6.5	-11.96	9.15	12x7.1	N5713	31.3	-11.95	10.52	2.8x2.5
N1068*	15.2	-11.04	10.80	7.1x6.0	N3627	6.5	-11.61	9.50	9.1x4.2	N5775	28.9	-11.97	10.43	4.2x1.0
N1084	18.6	-12.33	9.69	3.3x1.2	N3628	8.5	-11.54	9.80	15x3.0	N6000	31.0	-11.71	10.75	1.9x1.6
N1097*	16.5	-11.81	10.10	9.3x6.6	N3690	48.5	-11.32	11.53	2.9x2.1	N6090	126	-12.47	11.21	1.7x0.7
N1317	25.8	-12.62	9.68	2.8x2.4	N3783	36.1	-12.76	9.83	1.9x1.7	N6215	20.2	-11.83	10.26	2.1x1.8
N1365*	21.5	-11.36	10.78	11x6.2	N3982*	21.8	-12.37	9.79	1.7x1.5	N6221*	19.3	-11.65	10.40	3.5x2.5
I342	3.8	-11.36	9.28	21x21	N4030	26.4	-11.95	10.37	4.3	N6240	109	-11.96	11.59	2.1x1.1
N1433*	13.3	-12.55	9.18	6.5x5.9	N4038	23.3	-11.65	10.56	5.2x3.1	N6300*	14.0	-12.02	9.75	4.5x3.0
N1448	14.7	-12.22	9.59	7.6x1.7	N4039	23.3	-11.65	10.56	3.1x1.6	N6744	10.7	-12.55	8.99	20x13
N1482	25.4	-11.79	10.50	2.5x1.4	N4051*	12.9	-12.27	9.43	5.2x3.9	N6764	38.5	-12.44	10.21	2.3x1.3
N1559	16.3	-11.83	10.07	3.5x2.0	N4102	17.3	-11.62	10.34	2.8x1.2	N6810	28.8	-11.99	10.41	3.2x0.9
N1566*	19.4	-12.02	10.04	8.3x6.6	N4254	39.8	-11.78	10.90	5.4x4.7	N6946	5.5	-11.46	9.50	12x9.8
N1614	64.2	-11.82	11.28	1.3x1.1	N4258*	8.0	...	...	19x7.2	N6951*	24.3	-12.04	10.21	3.9x3.2
N1667*	61.2	-12.43	10.62	1.8x1.4	N4293	14.1	-12.55	9.23	5.6x2.6	I5063*	49.4	-12.60	10.27	2.1x1.4
N1672	16.7	-11.70	10.23	6.5x5.5	N4303*	13.6	-11.81	9.94	6.5x5.5	I5179	48.8	-11.96	10.90	2.3x1.1
N1792	15.4	-11.75	10.11	5.2x2.6	N4321	14.1	-11.88	9.90	7.4x6.3	N7331	14.4	-11.78	10.02	11x3.7
N1808	12.3	-11.31	10.35	6.5x3.9	N4385	34.5	-12.64	9.92	2.0x1.0	N7469*	67.0	-11.88	11.25	1.5x1.1
N2146	16.7	-11.16	10.77	6.0x3.4	N4388*	41.4	-12.24	10.47	4.8x0.9	N7541	37.5	-11.96	10.67	3.5x1.2
N2273*	28.5	-12.48	9.91	3.2x2.5	N4414	9.0	-11.77	9.62	3.6x2.0	N7552	22.5	-11.44	10.74	3.4x2.7
N2369	45.2	-11.94	10.85	3.5x1.1	N4418	34.7	-11.73	10.47	1.6x0.7	N7582*	22.0	-11.61	10.55	5.0x2.1
N2397	16.6	-12.29	9.63	2.5x1.2	N4457	13.6	-12.56	9.19	2.7x2.3	N7590*	22.0	-12.33	9.83	2.7x1.0
N2415	54.3	-12.35	10.60	0.9x0.9	N4527	13.5	-11.79	9.95	6.2x2.1	N7599	23.1	-12.37	9.84	4.4x1.3
N2559	21.4	-11.78	10.36	4.1x2.1	N4536	30.8	-11.81	10.65	7.6x3.2	N7632	21.3	-12.63	9.51	2.2x1.1
N2623	79.4	-11.94	11.34	2.4x0.7	N4565	27.2	-12.29	10.06	16x1.9	N7674	117	-12.54	11.08	1.1x1.0
N2798	28.6	-11.96	10.43	2.6x1.0	N4593*	41.3	-12.78	9.93	3.0x2.9	N7714	38.5	-12.30	10.35	1.9x1.4
N2903	7.3	-11.65	9.56	13x6.0	N4631	7.6	-11.50	9.74	16x2.7	N7771	58.0	-11.97	11.04	2.5x1.0
N2992*	34.1	-12.39	10.16	3.5x1.4	N4647	13.9	-12.44	9.33	2.9x2.3	N7793	3.3	-12.22	8.30	9.3x6.3

Notes: Column 1: NGC/IC; Col. 2: corrected distances from the NASA/IPAC Extragalactic Database (NED) (Virgo+Great Attractor+Shapley Super-cluster case, assuming $H_0 = 73.0$ km s^{-1}); Col. 3: *IRAS FIR*; Col. 4: *FIR* luminosity following from Cols. 2 and 3; Col. 5: optical size D_{25} taken from the Second Reference Catalog of Bright Galaxies (2RCBG, de Vaucouleurs *et al.*, 1976). Seyfert galaxies (Huchra & Burg 1992; Maiolino & Rieke, 1995) are marked by an asterisk.

or very little CO (‘CO-dark gas’). There is some confusion in the literature as different X values have been referred to as the ‘standard’ CO-to-H_2 conversion factor. In this paper, we define $X_{\circ}(\mathrm{CO}) = 2 \times 10^{20}$ cm^{-2}/ K km s^{-1} (corresponding to 4.3 M$_{\odot}$ pc^{-2} when it also includes a helium contribution) as the standard factor to convert CO intensity into H_2 column density.

In one form or another, the ‘standard’ factor is frequently applied to other galaxies, often without caveats of any sort. These are essential, however, as the effects of metallicity, irradiation, and excitation may cause X to vary by large factors in different environments such as are found in low-metallicity dwarf galaxies, galaxy centers, luminous star-forming galaxies, molecular outflows, and high-redshift galaxies, as was already explained in the pioneering papers by Maloney & Black (1988) and Maloney (1990). Even the X-factor of our own Galactic center region has been known to be very different since Blitz *et al.* (1985) discussed the remarkably low ratio of gamma-ray to CO intensities in the central few hundred parsecs and suggested that it is caused by H_2/^{12}CO abundances that are an order of magnitude below those in the rest of the disk. These low X values were since confirmed, for instance, by Sodroski *et al.* (1995; $X = 0.22\,X_{\circ}$), Dahmen *et al.* (1998; $X = (0.06 - 0.33)\,X_{\circ}$), and Oka *et al.* (1998; $X = 0.12\,X_{\circ}$).

Conversion factors much lower than the standard Milky Way disk factor have also been ascribed to the central regions of other galaxies. Stacey *et al.* (1991) used a comparison of [CII] and ^{12}CO intensities to suggest a factor of three or more below $X_{\circ}$. Solomon *et al.* (1997) and Downes & Solomon (1998) argued that in ultra-luminous galaxies the X-factor had to be well below standard for the gas mass to avoid exceeding the dynamical mass, and adopted a value five times lower based on dust mass considerations.

Dust emission is relatively easy to measure but not so easy to interpret. Because the nature of the emitting dust grains is poorly known, uncertainties in interstellar dust composition, dielectric properties, size distributions, and dust-to-gas ratios cannot be avoided, and each of these properties may also change with environment. It is not entirely obvious how the measured intensity of infrared continuum emission should be translated into dust column density, let alone gas column density. These uncertainties allowed authors to err on the side of caution and estimate only moderately low values $X \sim 0.5\,X_{\circ}$ (M 82, Smith *et al.* 1991; M 51, Nakai & Kuno, 1995; NGC 7469, Davies *et al.* 2004), although substantially lower values $X \sim 0.1 - 0.2\,X_{\circ}$ (NGC 3079, Braine *et al.* 1997; NGC 7469, Papadopoulos & Allen 2000; NGC 4258, Ogle *et al.* 2014) have also been suggested. Such rather low values were also inferred from the local thermal equilibrium (LTE) analysis of optically thin but weak C^{18}O isotopologue emission (NGC 1068, Papadopoulos, 1999; NGC 6000, Martín *et al.* 2010).

The potentially problematical use of dust continuum emission for determining the properties of molecular gas is thus not preferred when actual molecular line measurements are available. Both observations and models have increasingly allowed the detailed analysis of CO line intensities using the more sophisticated non-LTE large velocity gradient (LVG) radiative transfer codes. An essential step toward reliable molecular gas mass determinations consists of reducing or breaking the crippling temperature-density degeneracies that plague the analysis of ^{12}CO measurements. This is accomplished by including measurements of CO isotopologues with lower optical depth. However, even the strongest of these (^{13}CO) is a relatively weak emitter. Consequently, only the brightest galaxies have been analyzed in this way (M82, Weisz *et al.*, 2001; NGC 4945 and the Circinus galaxy, Curran *et al.* 2001; Hitschfeld *et al.* 2008, Zhang *et al.* 2014; VV 114, Sliwa *et al.* 2013). These all yield values of $X = 0.1 - 0.2\,X_{\circ}$.

Extensive ^{13}CO surveys of external galaxies have so far been lacking in any transition. The survey presented in this paper is therefore a significant addition to the existing CO database on nearby galaxies. The newly determined multi-transition ^{12}CO-to- ^{13}CO isotopologue ratios allow us to determine more accurately the CO gas column densities and their relation to the much more abundant H_2 gas, including the values of X in a large number of galaxy central regions. The analysis of the ^{12}CO and ^{13}CO spectral lines is of particular importance in the interpretation of the Herschel Space Observatory (2009-2013) observations of galaxies in the two submillimeter [CI] lines and the far-infrared [CII] line (Israel *et al.* 2015; Kamenetzky *et al.* 2016; Fernández-Ontiveros *et al.* 2016; Lu *et al.* 2017; Croxall *et al.* 2017; Díaz-Santos *et al.* 2017; and Herrera-Camus *et al.* 2018). With it, we will place significant constraints on the relation between molecular and atomic carbon and determine the carbon budget in the observed galaxy centers.

2. Observations and data handling

2.1. SEST 15m observations

With the 15 m Swedish-ESO Submillimetre Telescope (SEST) at La Silla (Chile) [1] we conducted seven observing runs between May 1988 and January 1992, and another three runs between 1999 and 2003. Observations in the first period were mostly in the J=1-0 ^{12}CO transition, with some J=1-0 ^{13}CO observations of the brightest galaxies. In the second period we obtained additional J=2-1 ^{12}CO and J=1-0 ^{13}CO observations simultaneously. The SEST full width at half-maximum (FWHM) beam sizes were 45″ at 115 GHz (J=1-0 ^{12}CO) and 23″ at 230 GHz (J=2-1 ^{12}CO). All observations were made in a double beam-switching mode with a throw of 12′. Using the CLASS package, we binned the spectra to resolutions of 10-30 $\mathrm{km\,s^{-1}}$ after which third-order baselines were subtracted if the spectral coverage allowed it; otherwise, only a linear baseline was fit. A sample of the SEST observations is shown in Fig. 1. Line parameters were determined by fitting with one or two Gaussians as required by the shape of the profile. In the ^{13}CO profiles, we set the fitting range to be the same as determined in the ^{12}CO profiles with higher signal-to-noise ratios (S/N). Intensities were reduced to main-beam brightness temperatures $T_{\rm mb} = T_A^*/\eta_{\rm mb}$, using main-beam efficiencies at 115 GHz $\eta_{\rm mb}(115) = 0.66$ until October 1988, 0.74 until June 1990, 0.75 until October 1990, and 0.70 thereafter (L.E.B. Johansson, private communication), and $\eta_{\rm mb}(230) = 0.50$ for the whole period. The resulting velocity-integrated line intensities are listed in Tables 2 and 3.

2.2. IRAM 30m observations

Using the IRAM 30 m telescope on Pico de Veleta (Granada, Spain) [2] , we conducted four observing runs between December 2004 and July 2006, simultaneously observing the J=1-0 and J=2-1 transitions of both ^{12}CO and ^{13}CO with the facility 3mm and 1.3mm SIS receivers coupled to 4 MHz backends. All observations were made in beam-switching mode with a throw of 4′. The FWHM beam sizes were 22″ at 110/115 GHz and 11″ at 220/230 GHz. The diameter of the IRAM telescope is twice that of the JCMT (and the SEST) so that J=1-0 (IRAM) and J=2-1 (JCMT) observations are beam-matched, as are the J=2-1 (IRAM) and J=4-3 (JCMT) observations. A sample of the IRAM observations in the J=2-1 transition is shown in Fig. 2. The profile analysis was similar to that described for the SEST. Intensities were converted into main-beam brightness temperatures using main-beam efficiencies $\eta_{\rm mb}$ of 0.79/0.80 at 110/115 GHz and 0.59/0.57 at 220/230 GHz. The resulting velocity-integrated line intensities are listed in Tables 2 and 3.

---

[1] The Swedish-ESO Submm Telescope (SEST) was operated jointly by the European Southern Observatory (ESO) and the Swedish Science Research Council (NFR) from 1987 until 2003.

[2] IRAM is supported by INSU/CNRS (France), MPG (Germany), and IGN (Spain). The IRAM observations in this paper have benefited from research funding by the European Community Sixth Framework Programme under RadioNet R113CT 2003 5058187.

Table 2. Galaxy center J=1-0 line intensities

$\int T_{\rm mb} {\rm d}V$ (K km s^{-1})														
NGC	^{12}CO		^{13}CO		NGC	^{12}CO		^{13}CO		NGC	^{12}CO		^{13}CO	
IC	S45”	I22”	S47”	I23”	IC	S45”	I22”	S47”	I23”	IC	S45”	I22”	S47”	I23”
(1)	(2)	(3)	(4)	(5	(1)	(2)	(3)	(4)	(5	(1)	(2)	(3)	(4)	(5
134	17.1	...	...	...	3044	4.6	11.4	1.33	0.84	4736	...	42.2	...	4.27
253	321	1030	27.3	76.5	3079	93.5^{b}	235	...	14.1	4826	...	90.5	...	10.9
278	...	20.5	...	2.29	2554	11.7	...	...	...	4835	11.1	...	...	...
300	3.0	...	...	...	3175	18.9	42.8	1.69	4.26	4945	523	...	37.0	...
470	...	28.2	...	1.88	3227	...	61.7	...	3.46	5033	...	52.7	...	5.77
520	14.7	113	...	7.96	3256	68.6	...	2.8	...	5055	...	70.4	...	9.37
613	25.0	69.7	2.72	5.04	3281	1.4	...	...	...	5135	18.0	61.8	1.4	2.70
628	...	7.0	...	1.10	3310	...	7.8	...	0.65	5194	...	47.6	...	7.06
660	38.6	154	3.12	9.96	3351	...	17^{c}	...	...	5218	...	...	...	...
891	...	137	...	17.5	3504	20.2^{d}	56.4	...	4.30	5236	78.6	195	...	14.3
908	23.9	29.8	1.22	4.54	3556	...	53.9	...	4.31	Circ	155	...	8.45	...
972	...	66.7	...	5.75	3593	24.5	63.1	...	5.08	4444	9.4	...	1.18	...
Maf2	...	220	20.6	27.5	3620	47.3	...	3.37	...	5643	12.7	...	...	...
1055	28.8	76.7	3.92	10.7	3621	11.6	...	0.73	...	5713	16.8	45.4	0.99	2.87
1068	...	168	...	14.2	3627	27.3	74.4	...	5.59	5775	...	47.9	...	5.28
1084	19.8	30.4	1.52	2.29	3628	74.9	203	7.07	15.2	6000	22.5	74.7	1.83	4.88
1097	68.7	136	...	12.9	3690	...	68.8	3.50	2.97	6215	10.9	...	...	...
1317	2.4	...	...	...	3783	3.4	...	...	...	6221	30.8	...	2.7	...
1365	102	260	9.42	22.8	4030	23.1	42.1	...	6.40	6240	17.5	70.1	...	2.44
342	...	161	...	15.8	4038	30^{e}	46.8	1.9	3.50	6300	28.1	...	1.40	...
1433	14.6	...	2.18	...	4039	31^{e}	45.5	...	2.07	6744	10.3	...	...	...
1448	14.1	...	1.09	...	4051	...	37.8	...	2.08	6764	...	30.3	...	1.64
1482	15.5	32.1^{a}	1.12	...	4102	...	74.7	...	6.00	6810	29.4	...	...	...
1559	5.0	...	0.86	...	4254	31.3	42.7	...	4.79	6946	...	228	...	16.7
1566	23.2	...	1.45	...	4258	...	75.8	...	...	5063	5.4	...	...	...
1614	14.3	43.2	...	1.44	4293	...	36.0	...	3.03	5179	20.9	...	1.70	...
1672	23.5	...	2.21	...	4303	...	55.2	...	2.96	6951	...	50.1	...	4.77
1792	23.2	27.7	4.64	3.07	4321	23.7	81.5	...	8.14	7469	10.7	54.6	...	3.22
1808	92.0	135	3.49	7.57	4388	8.6	...	...	...	7541	21.2	28.4	...	2.90
2146	...	187	...	11.8	4414	...	51.4	...	6.90	7552	38.8	...	3.59	...
2273	...	16.5	...	1.57	4414	...	54.8	...	...	7582	32.5	...	...	...
2369	26.1	...	1.75	...	4457	...	29.5	...	1.94	7590	7.7	...	0.37	...
2397	16.6	...	1.41	...	4527	34.7	88.0	2.77	6.35	7599	2.4	...	...	...
2559	32.1	78.4	3.39	5.81	4536	14.8	61.6	...	3.27	7632	7.8	...	...	...
2623	...	18.2	...	2.6	4565	...	12^{c}	...	...	7714	1.0	3.5	...	0.64
2903	...	79.8	...	7.10	4593	1.7	7.5	...	...	7771	...	99.5	...	7.18
2992	8.2	...	...	...	4631	...	43.9	...	2.91	7793	2.7	1.8	...	...
3034	...	680	...	37	4666	30.7	73.6	...	7.58					

Notes: ^{a} IRAM, Albrecht *et al.* (2007 ^{b} SEST, Elfhag et al. (1996); ^{c} IRAM, Braine *et al.* (1993a) ^{d} SEST, Chini *et al.* (1996) ^{e} SEST, Aalto et al. (1995);

2.3. JCMT 15 m observations

The observations with the 15 m JCMT on Mauna Kea (Hawaii) [3] were obtained at various periods between 1988 and 2005. When the JCMT changed from PI-scheduling to queue-scheduling in the late 1990s, most of the survey measurements were made in back-up service mode. In both the J=2-1 and the J=3-2 transitions, ^{12}CO and ^{13}CO observations were made closely together in time. The JCMT FWHM beam-sizes were 22″ at 220/230 GHz and 14″ at 330/345 GHz. All observations were made in a beam-switching mode with a throw of 3′. We have discarded almost all early observations, preferring to use those obtained after 1992 with more sensitive receivers and the more sophisticated Dutch Autocorrelator System (DAS) back-end. We included data extracted from the CADC/JCMT archives on galaxies relevant to our purpose that had been observed by other observers (e.g., Devereux *et al.* 1994; Papadopoulos & Allen, 2000; Zhu *et al.* 2003; Petitpas & Wilson 2003).

We reduced the JCMT observations using the SPECX package, and subtracted baselines up to order three, depending on source line-width. We determined integrated intensities by summing channel intensities over the full range of emission. In the ^{13}CO profiles, we set this range to be the same as determined in higher S/N ^{12}CO profiles. Antenna temperatures were converted into main-beam brightness temperatures with efficiencies $\eta_{\rm mb}(230)$ = 0.70 and $\eta_{\rm mb}(345)$ = 0.63. The velocity-integrated line intensities are listed in Tables 3 and 4. Available J=4-3 ^{12}CO observations, many of which were discussed in earlier pa-

---

[3] Between 1987 and 2015, the (JCMT was operated by the Joint Astronomy Centre on behalf of the Particle Physics and Astronomy Research Council of the United Kingdom, the Netherlands Organization for Scientific Research (until 2013), and the National Research Council of Canada.

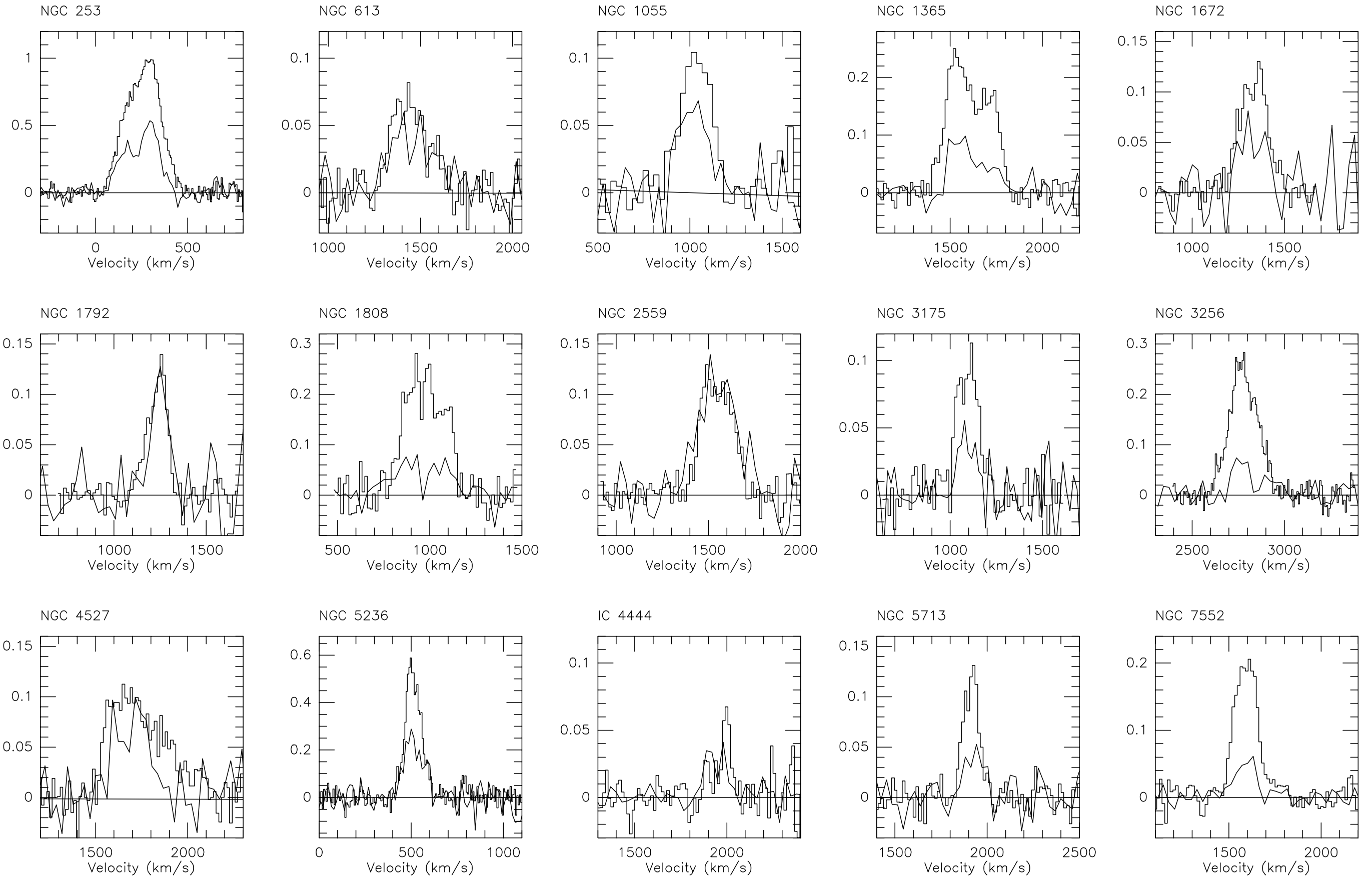

Fig. 1. Sample of SEST J=1-0 CO observations of galaxy centers, showing ^{12}CO (histogram) and superposed ^{13}CO (continuous lines) profiles; the intensities of the latter have been multiplied by a factor 5. Intensities are in $T_{\rm A}^{*}$ (K). Velocities are V(LSR) in km s^{-1}. Galaxies are identified at the top.

pers (Israel *et al.* 2009b, and references therein) were re-reduced and the results are listed in Table 5.

For almost half of the sample, small maps of the J=3-2 and J=2-1 ^{12}CO emission from the central region were obtained in addition to the central profiles. Maps and profiles of more than 16 galaxies have already been published (Israel, 2009a, b, and references therein). A sample of the new JCMT J=3-2 profiles is shown in Fig. 3. All JCMT J=3-2 ^{12}CO maps not included in our previous papers are shown in Fig. 4.

2.4. Observational error

We usually integrated until the peak signal-to-noise ratio in individual 10-20 km s^{-1} channels exceeded a value of 5-10. Especially for ^{13}CO line measurements, this required long integration times, sometimes up to several hours. The JCMT B-band receiver system had a relatively high system temperature spike around 330 GHz, resulting in a decreased sensitivity for the J=3-2 ^{13}CO line. The higher profile noise level and the limited bandwidth of 920 MHz (800 km/s) caused additional uncertainties in the line parameters that could only partly be alleviated using longer integration times. In the SEST 1999-2003 and all IRAM observing runs, the need to obtain a good detection of the ^{13}CO line automatically provided very high S/N for simultaneously observed stronger ^{12}CO lines.

From repeated observations, and from comparison with published measurements by others (summarized in Appendix A), we find the uncertainty in individual intensities obtained with the SEST in 1988-1992 to be about 30%, and those obtained in 1999-2003 to be about 20%. Depending on profile width, galaxies with intensities above 40-70 K km s^{-1} have somewhat lower uncertainties, whereas galaxies with intensities below 10 K km s^{-1} have larger uncertainties of up to 50%. The IRAM profiles in particular were obtained with wide velocity coverage and well-defined baselines, which is especially important for observations of galaxy center profiles with large velocity widths. They have relatively high S/N and are generally superior to those obtained in earlier measurements as well as to our own SEST and JCMT data. The uncertainty in the intensities observed with IRAM is ~ 10% for ^{12}CO, and 20 – 25% for ^{13}CO. Again from repeated observations, individual intensities measured with the JCMT have an uncertainty of 15 – 20%, except for those of J=3-2 ^{13}CO, where uncertainties range from 20% for bright narrow lines to 50% for weak broad lines. However, because the ^{12}CO and ^{13}CO intensities were measured (almost) simultaneously, the uncertainty in their ratio is lower, typically 10 – 20% for the J=1-0 and J=2-1 transitions and 15 – 25% for the J=3-2 transition. A comparison of the ^{12}CO-to-^{13}CO ratios determined in this paper and published in the literature may be found in Appendix B.

Table 3. Galaxy center J=2-1 line intensities

								$\int T_{\mathrm{mb}}\mathrm{d}V$ (K km s^{-1})									
NGC		^{12}CO		^{13}CO		NGC		^{12}CO		^{13}CO		NGC		^{12}CO		^{13}CO	
IC	J45”	J22”	I11”	J23”	I11”	IC	J45”	J22”	I11”	J23”	I11”	IC	J45”	J22”	I11”	J23”	I11”
(1)	(2)	(3)	(4)	(5)	(6)	(1)	(2)	(3)	(4)	(5)	(6)	(1)	(2)	(3)	(4)	(5)	(6)
253	572	1360	1588	120	149	2903	...	59.5	125	8.34	15.3	4647	9.7	15.9	...	...	...
275	3.4	6.3	...	...	...	2992	...	25.1	...	...	...	4666	26.2	53.1	75.5	5.91	6.35
278	12.6	19.6	23.5	2.93	2.34	3034	589	657	928	66.5	81	4736	15.4	42.7	65.7	4.33	6.96
470	...	23.2	62.7	1.65	4.34	3044	6.1	9.8	14.8	1.79	<1.0	4826	49.7	102	75.3	14.3	10.5
520	...	94.9	221	4.75	15.5	3079	89.3	188.2	445	13.4	27.7	4945	640^b	931	...	81.2	...
613	...	74.2	73.7	4.65	6.99	3175	16.4	34.3	54.0	3.20	4.96	5033	...	42.5	50.5	7.19	7.31
628	4.9	4.2	6.4	1.45	0.49	3227	...	48.3	104	5.55	9.37	5055	...	54.9	88.3	8.68	9.80
660	62.0	149	329	11.2	16.6	3256	...	314^b	...	...	...	5135	...	39.1	69.7	4.24	6.58
695	22.2	38.3	...	...	...	3310	...	8.7	12.8	0.74	1.04	5194	46.9	54.2	69.8	5.82	6.84
891	...	61.6	165	5.59	18.3	3504	...	51.9	129	3.84	12.6	5218	17.8	52.6	...	...	...
908	...	18.4	19.2	1.59	2.36	3593	...	41.7	73.5	5.46	8.48	5236	118	251	271	28.5	32.6
972	30.5	70.5	90.8	4.87	7.90	3620	...	76.4^a	...	...	...	Circ	...	234^c	...	...	...
Maf2	104	247	239	26.7	34.3	3621	...	8.5^a	...	...	...	5433	...	21.3	...	<0.6	...
1055	...	54.4	90.1	6.25	10.1	3627	33.0	74.3	89.2	5.43	9.01	4444	...	9.9^d	...	...	...
1068	103	239	236	21.2	16.4	3628	72.4	162	262	15.5	19.6	5713	37.0	56.6	65.9	6.14	4.77
1084	...	30.7	28.4	3.59	3.15	3690	30.0	64.4	63.9	3.2	...	5775	...	34.5	55.9	3.03	6.16
1097	...	119	166	5.93	16.2	3982	...	13.9	...	...	...	6000	...	76.3	132	7.70	12.8
1365	97.9	248	333	21.9	28.5	4030	...	35.1	37.5	3.57	3.81	6215	...	17^c	...	...	...
342	106	173	205	27.2	24.3	4038	40.6	63.6	52.9	3.78	3.80	6221	...	30.4^a	...	...	...
1433	...	14.2^a	...	...	...	4039	...	35	41.7	2.84	3.09	6240	38.3	70.2	...	1.84	...
1448	...	8.7^a	...	...	...	4051	...	22.2	59.3	1.06	2.88	6300	...	20.4^a	...	...	...
1482	...	18.3^a	...	...	...	4102	...	90.4	92.6	6.17	6.81	6764	...	22.6	73.1	1.00	2.98
1559	...	4.4^a	...	...	...	4254	...	40.6	47.4	3.75	6.00	6946	113	240	361	17.7	24.1
1566	...	10.9^a	...	...	...	4258	22.9	44.3	118	...	...	6951	...	39.3	97.7	5.15	13.6
1614	...	32.1	...	...	...	4293	...	26.9	52.3	5.44	6.45	7331	13.0	15.5	...	2.50	...
1667	...	13.6	...	...	...	4303	23.8	42.6	80.0	3.27	7.09	7469	16.7	52.0	117	3.51	6.17
1792	19.8	29.8	33.6	3.98	4.47	4321	31.2	55.6	121	4.87	12.2	7541	...	59.7	30.2	3.80	4.09
1808	1030	165	185	13.5	14.3	4388	...	22.1	...	...	...	7552	...	123^c	...	...	...
2146	55.8	164	203	24.0	18.6	4414	...	37.1	35.4	4.64	3.97	7582	...	116^c	...	...	...
2273	...	16.9	31.6	1.28	2.85	4457	...	27.5	32.6	1.45	1.48	7590	...	7.3^a	...	...	...
2369	...	43.6^a	...	...	...	4527	...	103	89.2	5.26	5.75	7674	...	11.5	...	...	...
2397	...	14.7^a	...	...	...	4536	...	63.5	101	5.04	10.8	7714	...	9.5	2.3	<1.0	...
2415	...	13.5	...	0.9	...	4565	6.61	10.1	...	...	...	7793	...	...	2.6	...	...
2559	32.6	69.7	121	8.24	11.6	4593	...	2.2	6.0	...	...						
2623	...	25.9	22.1	<3	4.75	4631	27.1	34.3	41.1	1.96	3.14						

Notes: [a] SEST, This Paper; [b] SEST, Ott et al. (2001 [c] SEST, Aalto et al. (1995); [d] SEST, Chini et al. (1996);

3. Results

Tables 2 through 5 list all directly observed ^{12}CO intensities measured with the SEST (S), the JCMT (J), and the IRAM 30m (I) telescope, with the resolution in arcseconds indicated in the headers. For comparison purposes, we also listed additional intensities at lower resolutions determined by the convolution of JCMT ^{12}CO maps such as those shown in Fig. 4. In a few cases we have included published measurements obtained by others with the same telescopes; these are identified in the footnotes.

With Tables 2 throughj 4 we have constructed transition line ratios in matched beams. Individual ratios have typical errors of 25% to 30%. The histograms in Fig. 5 show the distributions of the transition line ratios. These are clearly peaked, and their width reflects in roughly equal parts the measurement error and the intrinsic variation. The average (1-0):(2-1):(3-2):(4-3) ^{12}CO line intensities relate to one another as (1.09 ± 0.04):(1.00):(0.76 ± 0.05):(0.62 ± 0.05). As a practical application, the quantities $1.1 \times I_{CO}(2\text{-}1)$ or $1.4 \times I_{CO}(3\text{-}2)$ can thus be used to estimate the central $I_{CO}(1\text{-}0)$ intensities in gas-rich spiral galaxies when these are needed but not measured. Oka *et al.* (2012) found the identical (3-2):(1-0) ratio for the central region of the Milky Way. The central (2-1):(1-0) ratio of 0.9 exceeds the value 0.7 used by Sandstrom *et al.* (2013) for galaxy disks. The bottom diagram in Fig. 5 shows (3-2):(2-1) ratios as a function of the parent galaxy FIR luminosity, ranging from $\log L(FIR) = 9$ for normal galaxies over $\log L(FIR) = 10$ for starburst galaxies to $\log L(FIR) = 11$ for luminous infrared galaxies (LIRGs). It does not reveal a clear dependence on galaxy class, nor does any of the other transition line ratios.

An essential part of this survey is the measurement of ^{12}CO-to-^{13}CO isotopologue ratios in the J=1-0, J=2-1, and J=3-2 transitions; high atmospheric opacities render the J=4-3 ^{13}CO line practically unobservable from the ground. In galaxy disks and centers, the observed ^{12}CO lines are optically thick ($\tau > 1$), but in the observed three lowest transitions, the ^{13}CO lines have optical depths (well) below unity. This is important because including lines with low optical depth reduces the degeneracy that severely limits the analysis of the optically thick ^{12}CO lines. The measured ^{13}CO fluxes are listed in Tables 2-4, and Figs. 1 through 3 show that the ^{13}CO and ^{12}CO line profiles are very

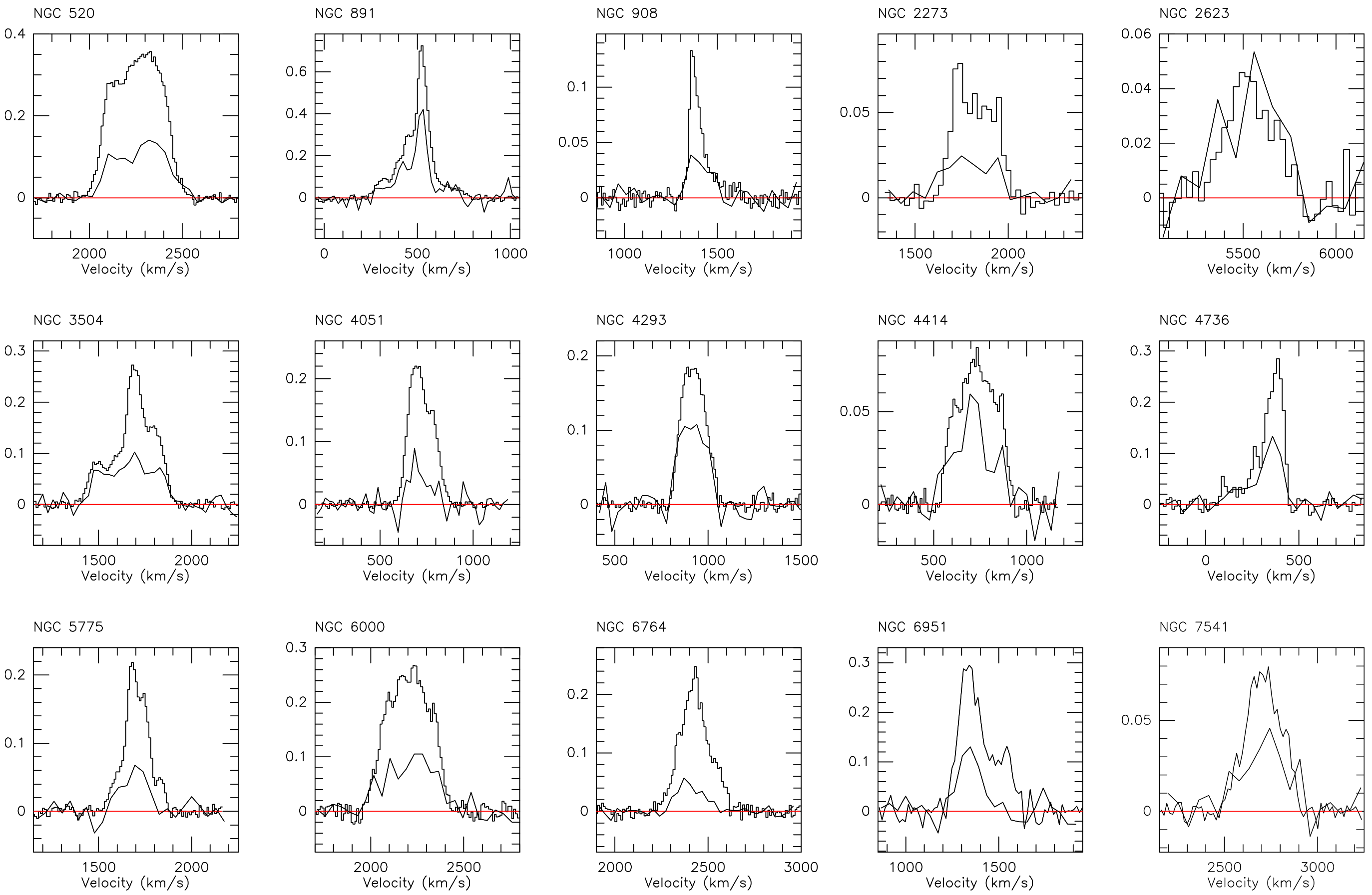

Fig. 2. Sample of IRAM J=2-1 CO observations of galaxy centers, showing ^{12}CO (histogram) and superposed ^{13}CO (continuous lines) profiles; the intensities of the latter have been multiplied by a factor 5. Intensities are in $T_{\rm A}^{*}$ (K). Velocities are V(LSR) in km s^{-1}. Galaxies are identified at the top. IRAM J=1-0 profiles (not shown) are similar, with better S/N.

Table 4. Galaxy center J=3-2 line intensities

							$\int T_{\rm mb} {\rm d}V$ (K km s^{-1})								
NGC	^{12}CO		^{13}CO	NGC	^{12}CO		^{13}CO	NGC	^{12}CO		^{13}CO	NGC	^{12}CO		^{13}CO
IC	J22"	J14"	J14"	IC	J22"	J14"	J14"	IC	J22"	J14"	J14"	IC	J22"	J14"	J14"
(1)	(2)	(3)	(4)	(1)	(2)	(3)	(4)	(1)	(2)	(3)	(4)	(1)	(2)	(3)	(4)
253	850	1449	124	1808	151	270	14.5	3690	40.3	81.4	...	4736	27.4	44.0	3.05
275	...	5.3	...	2146	137	236	17.3	3982	12.7	18.0	...	4826	49.9	91.9	10.9
278	14.0	17.9	1.83	2273	11.4	21.4	...	4030	...	19.1	1.92	4945	...	871	87.9
470	18.3	35.0	...	2415	...	13.6	0.7	4038	52.0	87.6	6.63	5033	24.1	27.7	2.36
520	...	56.1	5.9	2559	40.3	65.8	2.94	4039	23.8	59.5	4.08	5055	...	28.6	3.41
613	...	55.1	4.6	2623	18.9	40.3	<4	4051	29.9	63.4	...	5135	52.4	87.3	3.9
628	2.7	2.8	...	2798	43.6	64.8	...	4102	...	68.0	5.30	5194	31.7	37.3	4.37
660	94.0	128	10.1	2903	53.8	78.8	6.32	4254	...	24.3	4.87	5236	137	233	23.3
695	15.8	32.7	...	2992	18.7	25.8	...	4258	32.7	50.3	...	5433	...	29.0	<1.6
891	...	38.1	3.50	2993	17.4	22.7	...	4293	...	31.7	2.14	5713	27.5	42.8	2.62
908	...	7.2	1.20	3034	548	649	72	4303	23.0	43.8	2.66	5775	20.0	30.0	<0.8
972	39.0	61.4	3.46	3044	4.9	8.7	...	4321	35.3	62.3	5.40	6000	...	58.5	...
Maf2	179	321	33.4	3079	...	154	26	4385	6.11	7.95	...	6090	17.6	45.0	...
1055	...	30.3	2.65	3175	23.2	32.6	2.28	4388	10.9	16.5	...	6240	80.4	127	4.80
1068	101	153	10.7	3227	41.7	92.6	5.32	4414	18.7	20.6	3	6764	20.6	31.4	...
1084	...	17.9	1.8	3256	117	173	...	4418	...	47.4	...	6946	117	201	18.9
1097	107	142	...	3310	11.7	27.9	3.12	4457	19.0	29.7	1.24	6951	46.8	56.5	3.72
1365	170	284	23.3	3351	29.9	45.9	...	4527	...	33.3	3.3	7331	7.1	10.1	1.76
342	121	186	17.3	3504	34.5	57.0	6.26	4536	...	77.3	4.79	7469	40.7	89.6	3.95
1614	...	32.7	...	3593	...	39.4	2.86	4631	23.2	29.6	4.29	7541	...	35.6	3.46
1667	7.1	13.9	...	3627	48.7	84.1	6.93	4647	8.0	11.7	...	7674	9.60	18.3	...
1792	...	16.4	2.13	3628	114	210	23.1	4666	35.3	51.5	3.56	7714	...	8.5	...

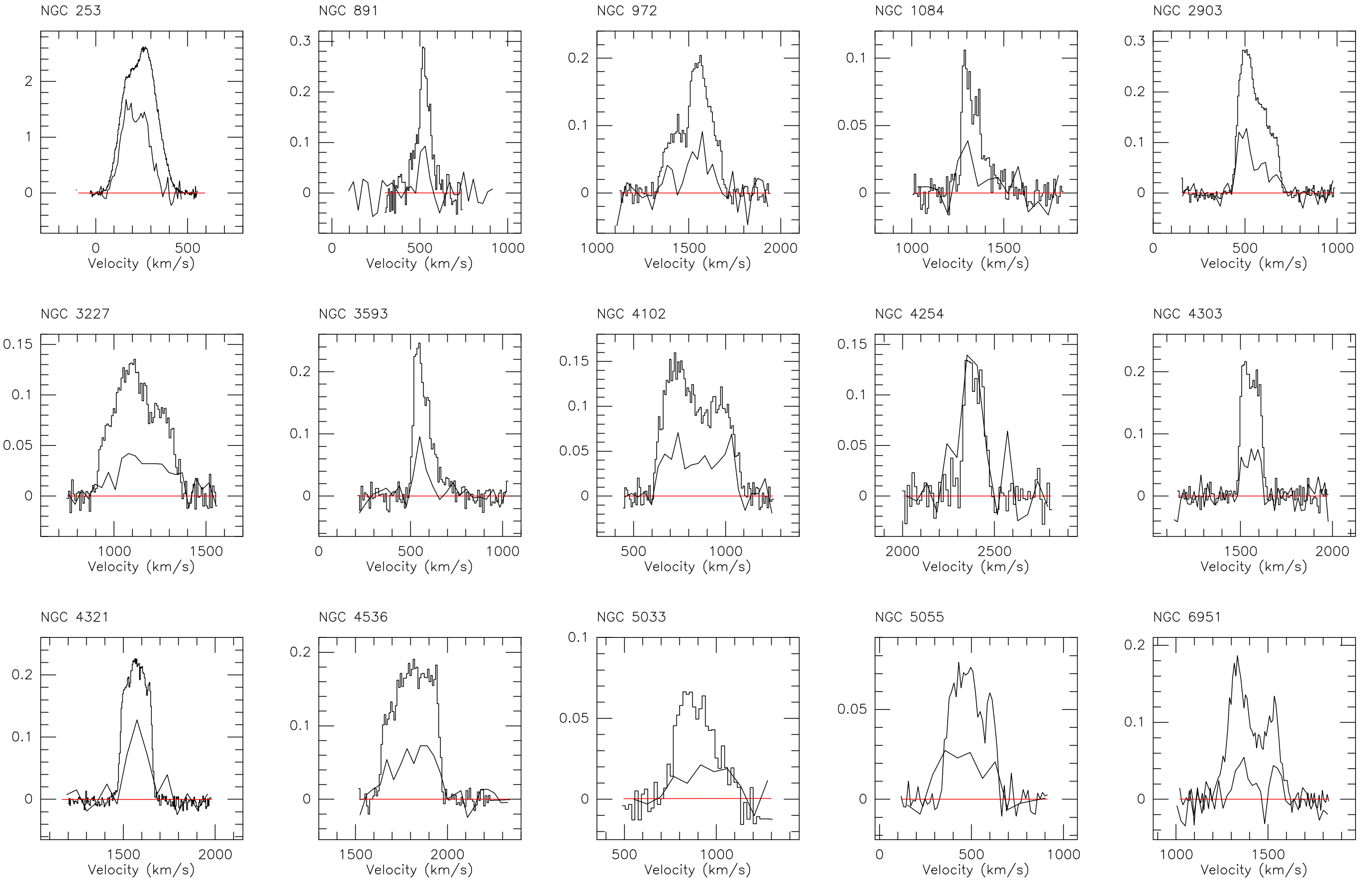

Fig. 3. Sample of JCMT J=3-2 CO observations of galaxy centers, showing ^{12}CO (histogram) and superposed ^{13}CO (continuous lines) profiles; the intensities of the latter have been multiplied by a factor 5. Intensities are in $T^*_{\rm A}$ (K). Velocities are V(LSR) in km s^{-1}. Galaxies are identified at the top. JCMT J=2-1 profiles (not shown) are similar, with better S/N.

Table 5. Galaxy center J=4-3 line intensities

$\int T_{\rm mb}{\rm d}V$ (K km s^{-1})															
NGC IC (1)	J22" (2)	^{12}CO J14" (3)	J11" (4)	NGC IC (1)	J22" (2)	^{12}CO J14" (3)	J11" (4)	NGC IC (1)	J22" (2)	^{12}CO J14" (3)	J11" (4)	NGC IC (1)	J22" (2)	^{12}CO J14" (3)	J11" (4)
253	927	1484	2046	2146	...	122	139	3628	89.2	146	206	4826	66	114	121
278	8.4	9.1	11.5	2273	...	...	6.1	3690	47.2	51.9	59.4	5033	...	...	4.7
660	92	122	161	2623	...	...	18.7	4051	...	...	19.5	5194	25.0	28.3	30.6
Maf2	155	284	407	3034	396	481	547	4321	...	...	12.2	5236	111	192	257
1068	156	219	291	3079	131	208	243	4631	...	14.2	17.0	6946	110	183	245
342	111	190	223	3175	...	...	28.8	4666	15.5	22.8	34.2	7469	47	68	92

similar in width and shape. The single but frequently occurring difference is a dip in the central ^{13}CO profile at the systemic velocity where the ^{12}CO profile shows a flat top. This dip suggests an optical depth decrease in the nuclear line of sight that is consistent with a lack of material (an unresolved 'hole') in the very galaxy center.

Taking into account the errors, the isotopologue ratios in the lower two transitions do not depend on the aperture size. We therefore averaged whenever possible the isotopologue ratios in the 45" and 22" and the 22" and 11" apertures. The resulting distributions in the lower three transitions are shown in Fig. 6. The ^{12}CO-to-^{13}CO ratios peak around R=10 in the J=2-1 transition and well above that in the other two transitions. The isotopologue ratios in the three transitions are clearly related to one another. In all three transitions, most isotopologue ratios occur between R=8 and R=16. Only a few galaxies have $R < 8$, which is characteristic of the relatively high optical depths of dense star-forming molecular clouds in the spiral arm disk of the Milky Way.

4. CO maps and radial extent

4.1. Global CO flux and central fraction

The literature provides J=1-0 ^{12}CO observations at various resolutions for about 50 sample galaxies that are accessible from the northern hemisphere, and CO fluxes of entire galaxies have been published by Stark *et al.* (1987), Sage (1993), Young *et al.*

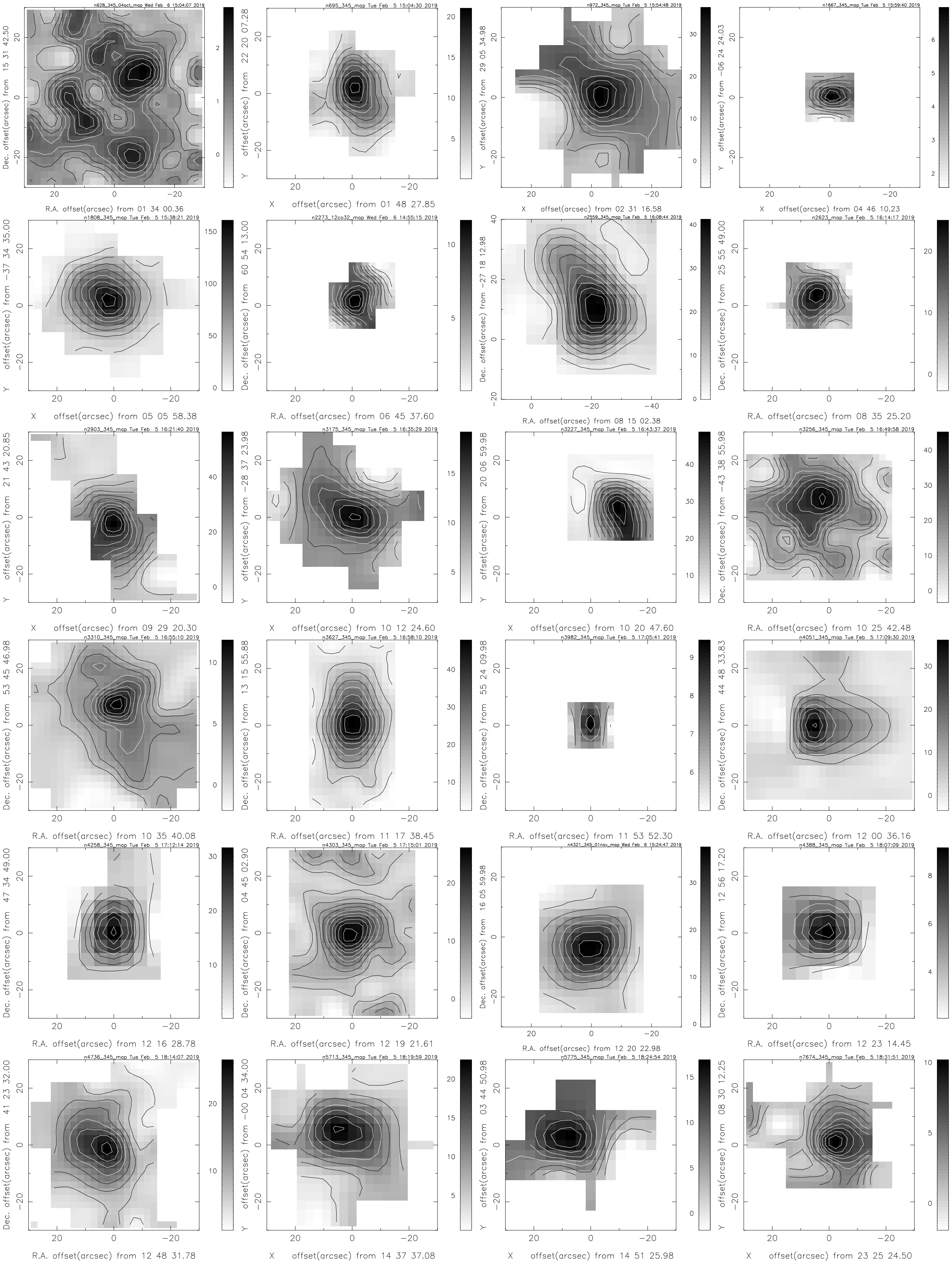

Fig. 4. JCMT ^{12}CO(3-2) $1' \times 1'$ galaxy center maps. Linear contours $\int T_{mb} \mathrm{d}V$ ($\mathrm{K\,km\,s^{-1}}$) are superposed on grayscales $\int T_A^* \mathrm{d}V$ ($\mathrm{K\,km\,s^{-1}}$). Galaxy names, the values of the lowest white contour, and the contour step are as follows: Row 1: NGC 628 (2, 0.5), NGC 695 (20, 4), NGC 972 (24, 6), NGC 1667 (7.5, 1.5); Row 2: NGC 1808 (150, 30), NGC 2273 (12, 2), NGC 2559 (36,6), NGC 2623 (24,4); Row 3: NGC 2903 (48, 8), NGC 3175 (15, 5), NGC 3227 (48, 8), NGC 3256 (48, 8); Row 4: NGC 3310 (12, 3), NGC 3627 (40, 8), NGC 3982 (14, 2), NGC 4051 (32, 8); Row 5: NGC 4258 (30, 6), NGC 4303 (20, 4), NGC 4321 (32, 8), NGC 4388 (9, 1.5); Row 6: NGC 4735 (25, 5), NGC 5713 (20, 5), NGC 5775 (12, 3), NGC 7674 (7.5, 1.5).

Table 6. Spatial distribution of CO emission

	Whole galaxy^a		Central peak^b			Whole galaxy^a		Central peake^b			Whole galaxy^a		Central peak^b	
NGC IC 1)	α (2)	$d_{\rm CO}$ ′ (%) (3)	$\Omega_{\rm CO}$ nsr (4)	$R_{\rm CO}$ kpc (5)	NGC IC (1)	α (2)	$d_{\rm CO}$ ′ (%) (3)	$\Omega_{\rm CO}$ nsr (4)	$R_{\rm CO}$ kpc (5)	NGC IC (1)	α (2)	$d_{\rm CO}$ ′ (%) (3)	$\Omega_{\rm CO}$ nsr (4)	$R_{\rm CO}$ kpc (5)
253	0.6	8.0 (43)	16	0.3	3079	0.7	1.5 (19)	5	0.5	4631	1.3	2.8 (18)	min	...
278	1.9	1.0 (46)	min	...	3175	0.9	...	8	0.9	4647	1.3	2.5 (85)	13	...
470	...	...	13^1	1.1	3227	0.6	3.2 (60)	4	0.6	4666	1	2.8 (60	min	...
520	1	1.3 (29)	11^2	0.9	3256	...	...	12	2.0	4736	1.1	4.5 (40)	5.3	0.5
613	...	...	...	1.1	3310	0.9	1.9 (63)	unr	...	4826	1.2	1.4 (15)	7.4	0.2
628	2	3.4 (33)	min	...	3504	0.6	2.0 (74)	7^7	1.1	4945	...	...	14.4^{14}	0.4
660	0.6	6.5 (71)	12	0.5	3556	0.6	5.2 (60)	...	...	5033	1.1	2.8 (27)	12.4^{15}	0.8
891	0.2	...	19	0.8	3593	0.8	1.5 (26)	5^8	0.5	5055	1.3	3.9 (31)	$4.2^{10,15}$	0.3
908	1.2	2.1 (35)	...	...	3627	1.1	4.7 (51)	8	0.4	5135	0.4	...	4.2^{16}	2.0
972	0.4	...	18	2.3	3628	1.1	2.9 (20)	7	0.5	5194	...	...	min	...
Maf2	...	...	14	0.2	3690	0.7	0.9 (32)	...	...	5236	1.4	3.7 (29)	6.0	0.2
1055	1.3	2.3 (30)	min	...	4030	0.8	2.7 (62)	...	...	Circ	...	...	...	0.3
1068	1.2	5.0 (70)	23	1.0	4038	1.4	1.2 (23)	4^9	0.7	4444	...	...	...	1.2
1084	0.8	3.4 (100)	...	...	4039	1.2	1.1 (36)	5^9	0.6	5713	1.6	1.1 (40)	9.8	1.8
1097	0.5	2.3 (30)	21^3	0.9	4051	0.8	3.3 (62)	6	0.7	5775	0.6	2.1 (50)	7.4	1.5
1365	0.8	...	17^4	1.2	4102	0.2	...	11^{10}	0.8	6000	...	0.8 (40)	unr	...
I342	1.3	8.7 (41)	13	0.2	4254	1.4	2.8 (52)	6^{11}	2.1	6240	0	...	unr	...
1482	1.6	0.8 (30)	...	...	4258	0.7	3.3 (17)	5^{12}	0.2	6764	0.8	...	4.7^{17}	1.1
1614	0.4	0.9 (71)	unr	...	4293	0.7	0.8 (10)	...	...	6946	1.0	6.5 (57)	5.3	0.2
1672	...	...	...	2.3	4303	1.0	2.0 (41)	7	0.5	6951	0.8	3.1 (80)	6.7^{10}	0.9
1808	1.4	...	11	0.3	4321	1.1	4.0 (55)	6	0.4	7469	...	0.9 (60)	4.7	2.6
2146	1.1	1.2 (20)	14	1.1	4388	...	...	6	1.0	7541	1.2	1.2 (34)	...	9.9
2273	0.7	1.1 (35)	11	1.0	4414	1.4	1.6 (44)	min	...	7674	...	...	7.4	4.5
2559	0.9	1.3 (30)	11	1.2	4457	0.5	...	...	...	7714	...	0.9 (50)	...	...
2623	1.0	0.7 (32)	5	2.3	4527	1.0	1.8 (30)	5^{13}	0.6	7771	0	...	unr	...
2903	0.8	2.6 (21)	5	0.2	4536	0.1	...	4^{10}	1.0					
3034	1.1	1.8 (17)	23^6	0.7	4565	1.5	...	min	...					

Notes: ^{a} For an explanation of the columns, see Section 4.1. ^{b}: For an explanation of the columns, see Section 4.2. ^{c}: See Section 5. References: 1. Rampazzo *et al.* (2006); 2. Yun & Hibbard (2001); 3. Gerin *et al.* (1988); 4. Sandquist, Aa, (1999); 6. Seaquist & Clark (2001); 7. Kuno *et al.* (2000); 8. García-Burillo *et al.* (2000); 9. Wilson *et al.* (2000); Zhu *et al.* (2003); Schulz *et al.* (2007); 10. Kuno *et al.* (2007); 11. Sofue *et al.* (2003); 12. Cox & Downes (1996); 13. Shibatsuka *et al.* (2003); 14. Ott *et al.* (2001) 15. Helfer *et al.* (2003); 16. Regan *et al.* (1999); 17. Eckart *et al.* (1991);

(1995), and Chung *et al.* (2009). These are summarized in Appendix A, and examples of the multi-aperture photometry diagrams that can be constructed from them are shown in Fig. 7. In this section CO intensities are expressed as line fluxes (Jy km/s) per beam in order to emphasize their increase as larger areas are covered.

We determined slopes α_{CO} (defined by $F \propto \theta^{\alpha}$) describing the increase of flux F with beam-width θ [4]. In extended sources much larger than the sampling beams, the measured flux increases with the beam surface area so that $\alpha = 2$. Point-like sources much smaller than the sampling beams have identical fluxes in all beams so that $\alpha_{CO} = 0$. The observed CO emission does not represent either extreme, as Figs. 7 and 8 illustrate. The average slope is close to unity, $\alpha_{CO} = 0.96 \pm 0.06$, with a standard deviation of 0.42 (see Col. 2 in Table 6 and Fig. 9) and is independent of galaxy distance. Assuming that this sample is representative, we conclude that CO fluxes of gas-rich spiral galaxies can be extrapolated from one beam to another with a modest uncertainty of about 30% by taking the linear beam width ratio.

The galaxy CO extent ($d_{\rm CO}$) equals the angular size at which the extrapolated CO flux in Fig. 7, for instance, reaches the total CO flux taken from the literature. From internal consistency, we find that the average error in the total fluxes is 26% (cf. Appendix A), which dominates the error in the global size. We list the extrapolated global sizes in Col. 3 of Table 6, both as an angular size in arcminutes and as a fraction of the optical galaxy size D_{25} (taken from Col. 5 in Table 1). The distribution in Fig. 9 is distinctly peaked at 0.35 D_{25} but the average value is slightly higher at $(0.44 \pm 0.03)\,D_{25}$. As the average HI disk radius is 1.7 D_{25} (cf. van der Kruit & Freeman, 2011), the extent of CO-emitting gas is typically only 25% that of HI: in late-type galaxies, the molecular gas is much more concentrated than the atomic gas.

4.2. Inner galaxy CO concentrations

For more than half of the sample galaxies, small maps of the central CO emission at the relatively high resolution of 14" are provided by JCMT J=3-2 ^{12}CO observations. These include the 24 galaxies shown in Fig. 4, the 16 galaxies published in earlier papers (Israel *et al.* 1995, 2006; Israel & Baas 1999, 2001, 2003; Israel, 2009a, b), and some 20 more by the authors identified in the notes to Table 6. The resolution of these maps is sufficient to separate the emission of a central compact source from the extended disk emission discussed in the previous section. We determined both the projected solid angle subtended by the central compact sources and their radial extent (FWHM along the

---

[4] When we express CO intensities in temperature (K km s^{-1}) instead of flux units (Jy km s^{-1}), we have $\alpha' = \alpha$-2.

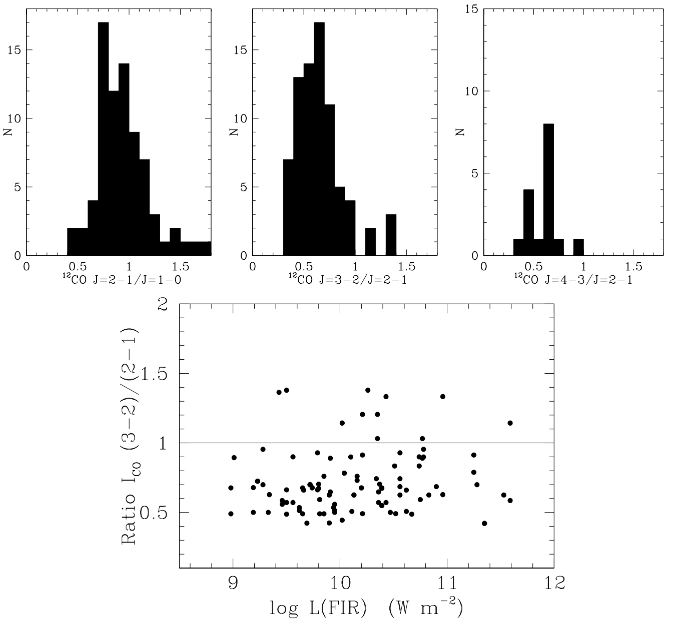

Fig. 5. Distribution of the J=2-1/J=1-0, the J=3-2/J=2-1, and the J=4-3/J=2-1 ^{12}CO intensities. Bottom: J=3-2 intensities relative to the J=2-1 ^{12}CO intensity as a function of galaxy total FIR luminosity.

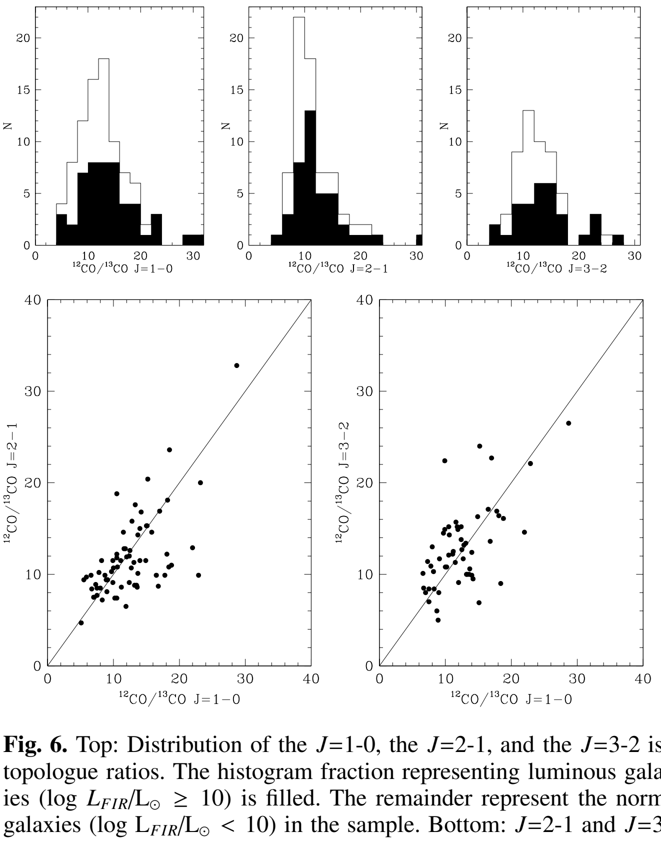

Fig. 6. Top: Distribution of the J=1-0, the J=2-1, and the J=3-2 isotopologue ratios. The histogram fraction representing luminous galaxies (log L_{FIR}/L$_\odot$ $\geq$ 10) is filled. The remainder represent the normal galaxies (log L$_{FIR}$/L$_\odot$ < 10) in the sample. Bottom: J=2-1 and J=3-2 isotopologue ratio as a function of the J=1-0 ratio.

major axis). We have at least partial information for 73 galaxies in Table 6. Ten of these do not have a central CO peak, but a central CO minimum instead (e.g., NGC 628 in the upper left corner in Fig. 4). In 6 galaxies, the central CO peak is unresolved. Except for NGC 3310, all are very distant galaxies, at distances of 60 Mpc or more. The observed central peak solid angle ($\Omega_{\rm CO}$) of 52 galaxies is listed in Col. 4 of Table 6. We corrected the central peak FWHM radius ($R_{\rm CO}$) observed in 57 galaxies for finite resolution by (Gaussian) deconvolution. Column 5 lists the resulting angular radii as well as the corresponding linear radii using the distances from Table 1. The distribution of the linear radii is shown in Fig. 10. As also shown in Fig. 4, in most of the sample galaxies, a significant amount of molecular gas is concentrated within a kiloparsec from the nucleus (mean radius of 400 pc). Another group of CO peak radii 2 $\leq$ $R_{\rm CO}$ $\leq$ 4.5 kpc represents galaxies with more extended inner disk features such as 'rings' (e.g., NGC 1068 and NGC 1097) or bars (e.g., NGC 1365). All galaxies with a central CO minimum, absent in the first group, are present in the second group with bright CO emission. Sakamoto *et al.*. (1999) obtained a similar result for 20 nearby spiral galaxies, many of which are also included in our sample. Their average 'local' scale length r_e = 0.53 kpc and average 'global' scale length R_e = 2.6 kpc closely correspond to the first two peaks in Fig. 10. The occurrence of compact circumnuclear molecular gas is probably more frequent than suggested by Fig. 10 because galaxies with distances beyond 15-20 Mpc are imaged with relatively limited linear resolution, making it hard to separate compact circumnuclear and extended inner disk emission.

4.3. CO size and beam-dependent intensity ratio

In the absence of maps, beam-dependent intensity ratios are sometimes used to estimate sizes. The map-derived solid angles in Table 6 can be used to determine the reliability of (effective) source sizes recovered from the ratio of line intensities in different apertures. In Fig. 11 we show the ratio of the ^{12}CO(3-2) intensities in 14" and 22" beams (Table 4) as a function of the measured solid angle (Table 6). In each case, both intensities were derived from the same map data-set. The observed points roughly follow the dashed line that marks the expected relation for circularly symmetric isolated compact peaks. The observational scatter is increased by the non-circularity of the peaks (points above the dashed line) and by the presence of extended emission especially in case of barely resolved peaks (points below the dashed line).

Figure 11 suggests that the central peak diameters estimated from homogeneous beam intensity ratios have errors of up to $\sim$ 40% that are mostly caused by unknown emission structure. In reality, the errors are larger because this method is used precisely when no map is available. In this case, the combination of heterogeneous data results in additional scatter. In Fig. 12 we compare 22"-to-11" beam intensity ratios from unrelated J=2-1 ^{12}CO JCMT and IRAM measurements (center panel) with 45"-to-22" (J=2-1, left panel) and 22-to-"/14" (J=3-2, right panel) beam intensity ratios extracted from the same JCMT map datasets. The dispersion of the ratios from the heterogeneous data in the center panel is twice that of the homogeneous ratios based on the same map data, which is especially clear for the J=3-2 ratios in the rightmost panel. The additional errors in the heterogeneous intensity beam ratios increase the errors in the derived source size to 70% or more. As long as the actual morphology of the emission remains unknown, more sophisticated treatments of the problem (e.g., Yamashita *et al.* 2017) do not significantly change these uncertainties. With such uncertainties, the multi-aperture method is only useful when no great accuracy is required.

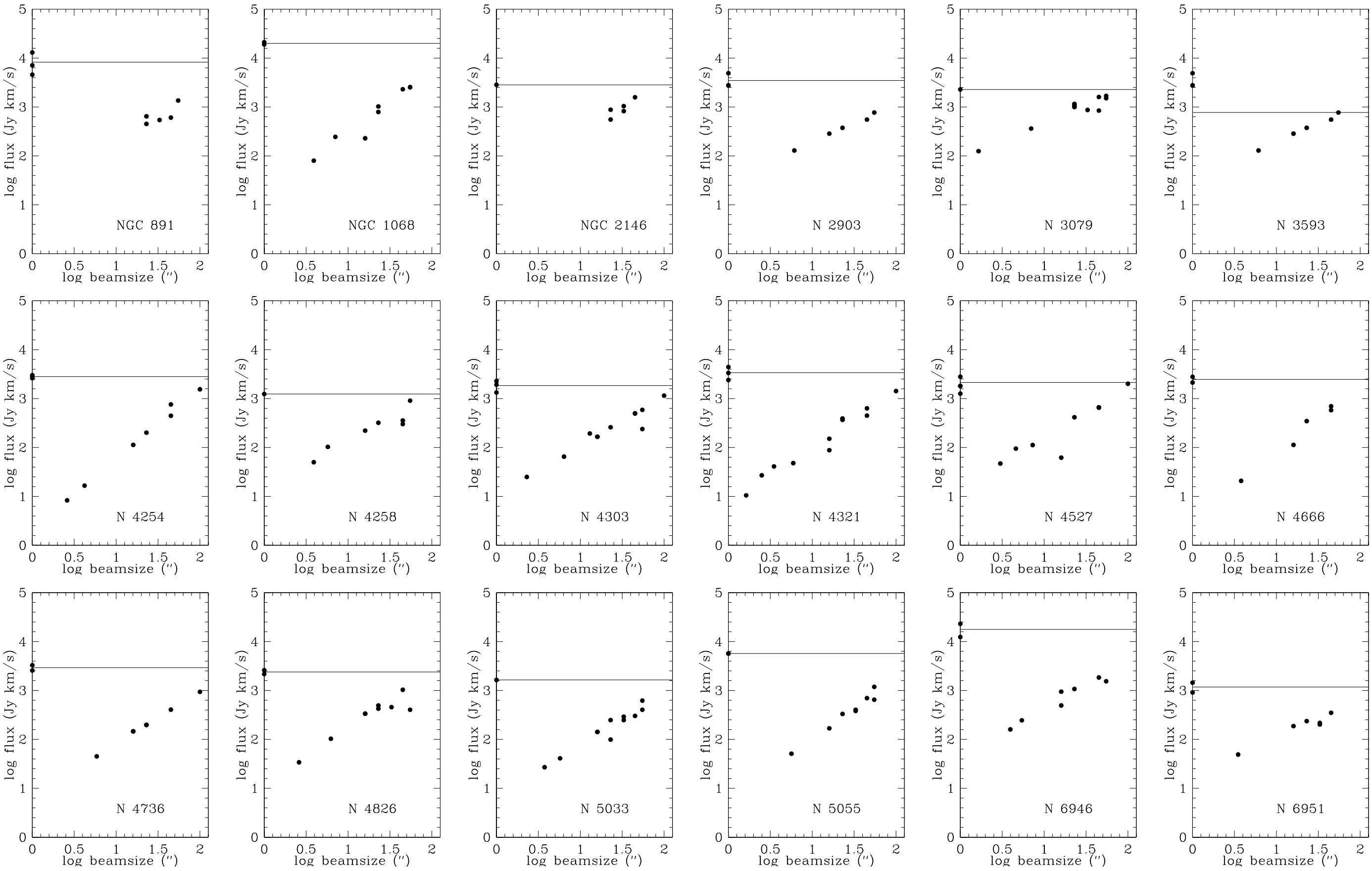

Fig. 7. J=1-0 ^{12}CO multi-aperture photometry of galaxies observed with different telescopes. The points on the vertical axis refer to the integrated CO line flux of the entire galaxy. In each panel, their average is marked by a horizontal line. References to the measurements used in these diagrams and in the photometry analysis are given in Appendix A.

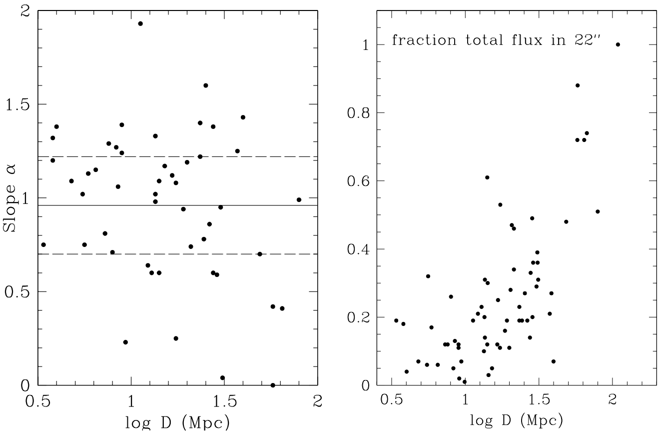

Fig. 8. Left: Slope α derived from J=1-0 ^{12}CO multi-aperture photometry as a function of galaxy distance. Completely unresolved galaxies have α = 0, and fully resolved galaxies have a constant CO surface brightness with α = 2. The solid line marks the mean value of the sample, the two dashed lines mark half-widths of the distribution. Right: Fraction of the total J=1-0 CO flux of the sample galaxies contained within a beam of FWHM 22" as a function of galaxy distance.

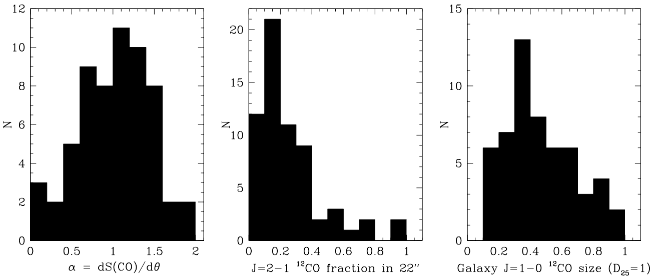

Fig. 9. Distributions of the sample galaxies as a function of (left) slope α, marking the change in measured J=1-0 CO flux as a function of increasing observing beam size, (center) the fraction f_{22} of the extrapolated total galaxy CO flux detected in a 22" beam, and (right) the extrapolated galaxy CO size as a fraction of the optical size (D_{25}) (see text).

5. CO radiative transfer modeling

The various transitions in our survey have been measured at different resolutions, but a meaningful comparison requires intensities at the same resolution. These are provided by the data measured directly (J=1-0, J=2-1) or indirectly (J=3-2, J=4-3) at a resolution of 22". Table 7 give all ratios in that aperture for all galaxies with at least two measured line ratios. Galaxies with a determination of the ^{12}CO-to-^{13}CO in the J=1-0 transition only are separately listed in Table 8. The ^{12}CO transition ratios in Cols. 3 through 5 of Table 7 have typical errors of 30%. The isotopologue ratios in Cols. 6 through 8 were determined by fitting each ^{13}CO to its corresponding ^{12}CO profile rather than by a division of the ^{12}CO and ^{13}CO intensities in Tables 2 through 4. By comparing the two methods, we find that the isotopologue ratios listed here indeed have typical uncertainties close to those

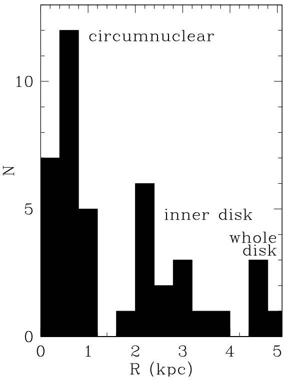

Fig. 10. Histogram of the intrinsic (beam-deconvolved) radii of the central concentrations in galaxy CO maps. Three characteristic radii are distinguished (see text).

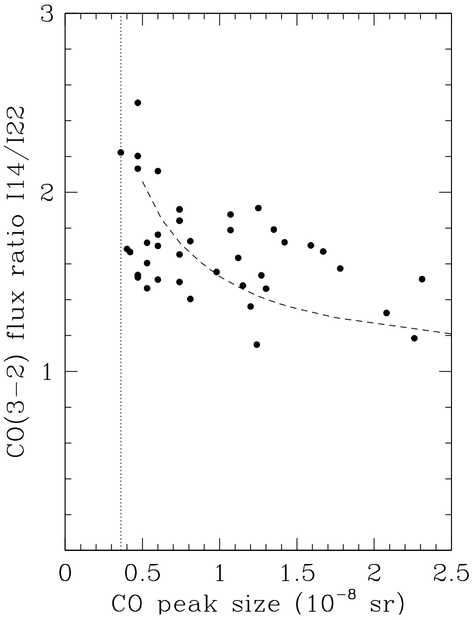

Fig. 11. Intensity ratio of J=3-2 ^{12}CO emission in beams of 22" and 14" as a function of the effective surface area of the central CO concentration taken from Table 6. Very extended emission has a ratio of unity, and fully unresolved (point-like) sources have a ratio of 2.25. The vertical line corresponds to the surface area of a 14" beam. The dashed curve indicates the relation expected for circular Gaussian sources without contamination by more extended emission.

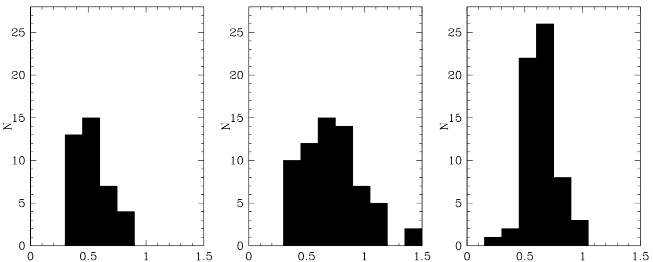

Fig. 12. Left: Histogram of J=2-1 CO intensity ratios in beams of 45" and 22". Center: Same for J=2-1 in 22" and 11". Right: Same for J=3-2 CO in 22" and 14" beams.

suggested in Section 2.4. In section 3.5 we noted that the ^{12}CO-to-^{13}CO isotopologue ratio is effectively independent of aperture in the J=1-0 and J=2-1 transitions (cf. Appendix B), and we have assumed that this is also true for the J=3-2 ratios measured in 14" apertures. Complementary values taken from the literature are identified by footnotes.

From the previous section, we determined that this normalized beam covers between 3% and 11% of the total CO surface area of the sample galaxies. When we restrict the sample to galaxies with distances between 10 Mpc and 40 Mpc, we obtain the same result. The fraction f_{22} of all CO flux contained in an aperture of 22" (Col. 2 of Table 7) is much higher, on average 26%. As expected, Fig. 8 shows that the individual values increase with increasing distance D. The distribution of individual f_{22} values is also shown in Fig. 9.

We have modeled the data in Table 7 with the statistical equilibrium radiative transfer code *RADEX* (Van der Tak *et al.* 2007). It provides model line intensities as a function of three input parameters per molecular gas phase: gas kinetic temperature $T_{\rm k}$, molecular hydrogen density $n_{\rm H_2}$, and the CO column density per unit velocity N(CO)/dV. Each combination of physical parameters uniquely determines a set of line intensities and ratios. The opposite is not true because the same line ratio may result from different combinations of physical input parameters. Reverse tracing is therefore not a unique process. Nevertheless, by comparing for each galaxy as many observed line ratios as possible to extensive grids of precalculated model line ratios, we may constrain and identify the physical parameters that best describe the actual conditions.

The large linear beam sizes that apply to galaxy center observations encompass molecular gas clouds at distinctly different temperatures and densities, which require more than one model gas phase to produce acceptable fits to the observations (see, e.g., Israel & Baas, 1999; Papadopoulos & Seaquist, 1999; Israel, 2009a, b). Good model fits are easily obtained for data sets containing only ^{12}CO observations, but the high degree of degeneracy between H$_2$ temperature and density renders such excellent fits non-unique and not very useful. Not even long ^{12}CO ladders (such as those extending up to J=13-12 obtained with *Herschel*-SPIRE) provide significant constraints (e.g., see Meijerink *et al.*, 2013). Fortunately, the degeneracy can be broken by measuring lines with low optical depth such as ^{13}CO in addition to the mostly optically thick ^{12}CO lines at the cost, however, of more physical parameters to be determined. Such combinations of ^{12}CO with related species yield constraints that although still not unique, are much tighter than those based on ^{12}CO alone.

We have modeled our data under the assumption that the emission is dominated by two distinct model gas phases. This is an important and necessary improvement over models assuming homogeneous single-phase gas that tend to provide a poor fit to the data when overconstrained. With only two gas phases, however, an ambiguity in temperature and density remains. It would be more realistic to model the gas with a smoothly changing temperature and density over a range of phases. This is, however, unfeasible even with the present relatively extensive data set because including more gas-phase components rapidly increases the number of unconstrained free parameters, which renders the result less rather than more realistic.

To simplify matters, we assumed that both gas phases have the same fixed isotopologue abundance, and we considered abundances of 40 and 80, respectively. In nearby galaxies such as NGC 253, NGC 4945, M 82, IC 342, and NGC 1068 the lower value seems appropriate (Henkel et al. 1994, 1998; Bayet *et al.* 2004; Henkel *et al.* 2014; Giannetti *et al.* 2014; Tang *et al.* 2019). The higher value may be more appropriate to (some of) the more distant very luminous galaxies such as NGC 5135, NGC 6240, NGC 7469, and Mrk 231 (e.g., Henkel *et al.* 2014; Sliwa *et al.* 2014; Tunnard *et al.* 2015; see also Israel *et al.* 2015).

Table 7. Line intensity ratios normalized to 22" aperture[a]

NGC IC	f_{22}	Transition ratio ^{12}CO(2-1) =1			Isotopologue ratio ^{12}CO/ ^{13}CO			NGC IC	f_{22}	Transition ratio ^{12}CO(2-1) = 1			Isotopologue ratio ^{12}CO/ ^{13}CO		
		1-0	3-2	4-3	1-0	2-1	3-2			1-0	3-2	4-3	1-0	2-1	3-2
(1)	(2)	(3)	(4)	(5)	(6)	(7)	(8)	(1)	(2)	(3)	(4)	(5)	(6)	(7)	(8)
253	19	0.76	0.63	0.68	12.7	10.7	11.7	4030	19	1.20	0.5	...	6.6	9.9	10.1
278	19	1.07	0.71	0.43	9.0	8.1	8.0	4038	19	0.66	0.75	...	12.8	15.8	13.2
470	..	1.22	0.79	...	15.0	15.3	...	4039	23	1.31	0.69	...	22.0	12.9	14.6
520	29	1.19	0.35	...	14.2	16.8	9.5	4051	23	1.71	1.35	...	18	21	...
613	..	0.94	0.8	...	11.5	14.6	11.3	4102	53	0.83	0.5	...	12.5	12.6	12.7
628	19	1.2	0.6	...	6.3	9.7	...	4254	7	1.08	0.6	...	8.9	9.4	5.0
660	21	1.11	0.68	0.66	14.0	17.0	12.4	4258	26	1.04	0.42	...	15[1,2]	...	...
891	7	2.2	0.32	...	7.8	10.2	10.9	4293	61	1.34	0.8	...	11.9	6.5	14.9
908	11	1.62	0.4	...	8.7	9.9	6	4303	14	1.29	0.54	...	18.1	12.2	16.4
972	..	.0.95	0.55	...	11.6	12.8	15.7	4321	12	1.47	0.63	...	10.0	10.7	10.8
Maf2	..	.0.89	0.73	0.63	8.0	8.5	13.0	4414	12	1.37	0.51	...	7.5	8.5	7
1055	10	1.42	0.4	...	7.3	8.9	11.4	4457	31	1.09	0.69	...	15	20	24
1068	5	0.70	0.42	0.65	11.8	12.8	15.2	4527	20	0.85	0.4	...	13.3	17.6	10
1084	16	0.98	0.5	...	13.2	8.8	10.0	4536	39	0.98	1.0	...	18.8	11.0	16.1
1097	12	1.14	0.90	...	10.5	18.8	...	4631	12	1.28	0.67	...	15.1	15.3	6.9
1365	..	1.05	0.69	...	11.1	11.5	12.2	4666	14	1.39	0.68	0.29	9.7	10.3	14.5
I342	3	0.93	0.70	0.64	10.2	7.4	10.8	4736	7	0.98	0.63	...	9.9	10.1	14.9
1614	27	1.34	2.21	...	30.0	...	...	4826	18	0.89	0.49	0.65	8.3	7.2	8.4
1792	72	0.94	0.5	...	7.0	7.5	8.0	4945[3]	0.8	0.65	...	15.7	13.2	9.9	
1808	..	0.95	1.03	...	16.5	12.6	17.1	5033	11	1.25	0.57	...	9.1	7.2	11.7
2146	..	1.15	0.89	...	15.0	8.7	13.6	5055	5	1.28	0.5	...	7.5	8.3	8.4
2273	25	1.01	0.65	...	10.5	12.2	...	5135	..	1.64	1.33	...	23	11	22
2415	49	...	...	...	...	11.2	20.0	5194	2	0.89	0.59	0.46	6.7	9.1	8.5
2559	34	0.57	...	...	9.9	11.5	22.4	5236	4	0.90	0.59	0.44	13.6	8.6	10.0
2623	51	0.70	0.73	...	7	5	...	Circ[4]	1.2	0.5	0.3	16	10	...	
2903	12	1.34	0.91	...	11.2	8.6	12.5	5713	30	0.80	0.49	...	14.9	11.5	16.3
3034	17	1.04	0.83	0.60	18.4	10.8	9.0	5775	36	1.39	0.58	...	9.1	9.4	...
3044	..	1.12	0.50	...	13.5	8.8	...	6000	36	0.98	0.7	...	13.7	10.1	...
3079	47	1.18	0.5	0.70	15.8	14.6	7.9	6240	100	1.00	1.14	...	29	40	26.5
3175	...	1.25	0.67	...	10.6	10.8	14.3	6764	..	1.33	0.93	...	19	24	...
3227	28	0.60	0.89	...	17.8	13.5	16.9	6946	6	0.95	0.49	0.46	13.7	14.3	10.6
3310	19.	0.90	1.38	...	12.4	12.0	15.2	6951	19	1.27	1.20	...	10.5	7.4	15.2
3504	33	1.08	0.67	...	13.1	11.3	13.4	7331	3	2.4	0.46	...	6[2,5]	6.2	5.7
3593	32	1.51	0.4	...	12.4	9.1	13.8	7469	74	1.06	0.79	0.90	17	17	23
3627	6	1.00	0.66	...	13.3	11.8	12.1	7541	21	0.47	0.4	...	8.2	11.5	10.3
3628	13	1.25	0.70	0.55	12.0	11.9	9.1	7552	...	...	...	...	10.8	9.1[6]	...
3690	50	1.07	0.62	0.73	23.2	20.0	...	7714	27	0.8	0.5	...	5.5	9.4	...

Note: [a]: See Section 5.
References: 1. Cox & Downes (1996); 2. Krips *et al.* (2010); 3. Dahlem *et al.* (1993); 4. Hitschfeld *et al.* (2008); 5. Vila-Vilaro *et al.* (2015); 6. Aalto *et al.* (1995).

Table 8. Galaxies with J=1-0 isotopologue ratio only

NGC (1)	$I_{^{12}\mathrm{CO}}/I_{^{13}\mathrm{CO}}$ (2)	NGC (3)	$I_{^{12}\mathrm{CO}}/I_{^{13}\mathrm{CO}}$ (4)	NGC (5)	$I_{^{12}\mathrm{CO}}/I_{^{13}\mathrm{CO}}$ (6)
1433	7.0	2369	14.9	4444	8.0
1448	13.0	2397	11.9	6221	12.0
1482	13.9	3256	25	6300	20
1559	5.8	3556	12.5	7552	10.8
1566	16.0	3620	14.0	7590	12.0
1672	10.6	3621	16.0	7771	13.9

For any particular set of line ratios, the *RADEX* model-fit line intensity, column density gradient, spatial density, and temperature in the two phases do not vary independently. The beam-averaged CO column density is sensitive only to the combined effect of these variations, and its resulting dispersion of about 30% is much lower than the uncertainty in each of the individual constituent model parameters, as illustrated in Table C.1.

The fraction of gas-phase carbon contained in CO is a function of the actual total carbon column densities N_{C}. We determined for each phase the fractional CO abundance [CO]/[C] as well as the total beam-averaged carbon column densities $\mathrm{N_C}$ using the chemical models presented by van Dishoeck & Black (1988) and updated by Visser *et al.* (2009). The detailed results of the two-phase modeling are given in Table C.2, where we present for each galaxy the model solution closest to the observations, regardless of the other possible model ratios within the observational error.

These results were combined to derive the beam-averaged fractional CO abundance [CO]/[C] and the beam-averaged total carbon column density N_{C} (Cols. 2 and 3) in Table D.1 for both of the assumed isotopologue abunandances. The beam-averaged CO column density N_{C} is the given by the producte:

$N_{\rm CO} = N_{\rm C} \times \frac{[\rm CO]}{[\rm C]}$. Out of 72 galaxies, 64 (90%) are successfully modeled with a [^{12}CO]/[^{13}CO] abundance of 40, and 28 galaxies (39%) even require this abundance for successful modeling. Only 8 galaxies (11%) need to be modeled with a high isotopological ratio of 80 instead. Half of the galaxy sample can be modeled with either ratio, but in most cases, the lower ratio of 40 provides better fits. Four galaxies (NGC 1614, NGC 4293, NGC 4527, and NGC 5236) have poor fits at either abundance.

6. Gas-phase carbon budget

6.1. Carbon monoxide fraction

The distribution of the fractional CO abundances is shown in Fig. 13 for the two isotopological abundances 40 (left) and 80 (center), with average values $f_{\rm CO} = 0.28$ and $f_{\rm CO} = 0.38$ and standard deviations of 0.18 and 0.17, respectively. We constructed the combined distribution (right) by averaging the results for the galaxies that could be fit at either ratio and by taking the single result for the galaxies that could not. The combined distribution has an average value $f_{\rm CO} = 0.33$. The standard deviation 0.16 exceeds the uncertainty in the individual values and represents an intrinsic spread of the ratios. The final adopted beam-averaged fractional CO abundances and gas-phase total carbon column densities are summarized in Table 9 (Cols. 2 and 3).

In Table 10 we have selected the data for all galaxies for which [CI] and [CII] measurements are also available. On average, molecular carbon represents only one-third of all gas-phase carbon in the observed galaxies. The remainder is atomic carbon either in neutral (C°) or in ionized form (C^+). The [CI] and [CII] line fluxes that are needed to further investigate this are found in the literature.

Figure 13 CO fraction of all C

6.2. Neutral atomic carbon fraction

We took central [CI] line data from the compilations by Israel *et al.* (2015), Kamenetzky *et al.* (2016), and Lu *et al.* (2017). Most of these were fluxes obtained with the SPIRE instrument onboard the ESA *Herschel* Space Observatory [5] in a 35" aperture. We expressed them as integrated main-beam brightness temperatures in units of $\rm K\,km\,s^{-1}$, reduced to our 'standard' beam by assuming identical [CI] and ^{12}CO distributions and filling factors and using the multi-aperture CO data in Tables 2 and 3 to estimate the 35" → 22" beam conversion factors (typically between 1.1 and 2.2). The resulting [CI] line intensities are given in Table 10.

We cannot derive two-phase atomic carbon column densities in the same way as the carbon monoxide column densities without additional assumptions because only two [CI] transitions are available for analysis. Fortunately, the [CI] intensities scale quite well with the observed ^{12}CO intensities. We are uncertain of the cause, but it is reasonable to expect that the [CI] emission either results from photodissociation of the CO clouds in the beam or from material that is left over in the formation of these CO clouds. In either case, neutral carbon and carbon monoxide are closely related and associated with the same H_2 gas. We therefore used the H_2 densities, kinetic temperatures, and relative filling factors from the CO analysis (Table C.2) as *RADEX* input to determine model [CI] intensities. From these, we derived beam-averaged column densities of [CI] in the same way as those of CO. This procedure is less critical for [CI] than for CO. With energy levels of 24 and 39 K and a critical density of 10^3 cm^{-3}, the [CI] emission is thermalized and close to being optically thin, roughly proportional to the C° column, and only weakly dependent on temperature and density (Schilke *et al.* 1993, Stutzki *et al.* 1997). We calculated neutral carbon column densities separately for the J=1-0 and the J=2-1 transitions and for the two isotopologue abundances. As expected, the average column densities are identical for the two [CI] transitions, and use of the parameters of the ^{12}CO/^{13}CO = 40 case yields column densities lower than those for the ^{12}CO/^{13}CO = 80 case by a factor of 0.6 (standard deviation 35%), reflecting the corresponding decrease in average optical depth. The final [CI] column densities in Table 10 are the averages of the independent determinations, as are the fractional [C°]/[C] abundances; their uncertainty is about 40%. The original SPIRE measurements are quite accurate, therefore most of this uncertainty must be due to assumptions in the analysis.

Our previous single gas-phase modeling of [CI] and CO intensities of galaxy centers (Israel *et al.* 2015) suggested a significantly higher CO-to-C° ratio. However, the two studies measured different quantities. In the earlier study we used line ratios of the mid-level J transitions of ^{12}CO, representing the more highly excited gas. We did not scale these results with line intensity, and the derived column densities were not corrected for the differentiating effects of beam filling factor and cloud velocity width. They sampled purely local conditions rather than the global conditions derived here.

The average gas-phase neutral atomic carbon fraction is 0.31. When we leave out the very high fractions derived for NGC 1365 (0.93) and NGC 5135 (0.86), the average drops to 0.26. In general, the [CI] fraction is somewhat below the CO fraction. The derived [CI] fraction exceeds that of CO in less than 20% of all cases

6.3. Ionized atomic carbon fraction

Ionized carbon [CII] line measurements useful for our purpose have been carried out with the PACS instrument (Poglitsch *et al.* 2010) onboard the ESA *Herschel* Space Observatory at a resolution of 11" in square pixels of 9.4" × 9.4" size. We used the compilations published by Fernández-Ontiveros (2016), Croxall *et al.* (2017), Díaz-Santos *et al.* (2017), and Herrera-Camus *et al.* (2018). We interpolated intensities in the central nine PACS pixels (28.2" × 28.2") and in the single central pixel to those expected in an intermediate 22" aperture. We also extrapolated central PACS pixel intensities to those expected in a 22" aperture assuming the emission to be point-like, with consistent results.

CO and [CI] emission can only originate in a neutral gas, but [CII] emission can also come from an ionized gas. The fraction of the [CII] emission from the neutral gas f_{CII} relevant to our analysis is estimated from the *Herschel* intensities of the [NII] 122μm (PACS) and 205μm (SPIRE) lines in the usual way; for a detailed description of this procedure and mapping results on many of the sample galaxies, see Croxall *et al.* (2017). Typically, 20% of the [CII] emission comes from ionized gas, and the neutral gas fractions of interest to us range from 0.57 to 0.92 (mean 0.81, average 0.75, with a standard deviation 0.21). Table 10 provides normalized and corrected [CII] intensities $I[CII]$ available for all galaxies in which [CI] has also been measured. In three cases, the actual fraction of [CII] emission arising from neutral

---

[5] *Herschel* was an ESA space observatory with science instruments provided by European-led Principal Investigator consortia and with important participation by NASA.

Table 9. Physical properties of 22” central regions

NGC	Carbon		Hydrogen			NGC	Carbon		Hydrogen			NGC	Carbon		Hydrogen		
IC	$\frac{[CO]}{[C]}$	N_C	N_{H_2}	M_{gas}	X	IC	$\frac{[CO]}{[C]}$	N_C	N_{H_2}	M_{gas}	X	IC	$\frac{[CO]}{[C]}$	N_C	N_{H_2}	M_{gas}	X
		e17	e21	e7				e17	e21	e7				e17	e21	e7	
	%	cm^{-2}		$M_\odot$	$X_\circ$		%	cm^{-2}		$M_\odot$	$X_\circ$		%	cm^{-2}		$M_\odot$	$X_\circ$
(1)	(2)	(3)	(4)	(5)	(6)	(1)	(2)	(3)	(4)	(5)	(6)	(1)	(2)	(3)	(4)	(5)	(6)
253	30	210	21	8	0.10	2903	36	15	2.2	3	0.07	4457	59	9	1.1	...	0.10
470	40	5	0.3	12	0.04	3034	39	83	8.1	14	0.06	4527	87	50	...	18	0.23
520	15	20	1.8	42	0.08	3044	09	3	0.2	...	0.06	4536	28	10	0.6	18	0.05
613	45	21	1.8	...	0.13	3079	30	42	4.0	35	0.08	4631	22	4	0.2	...	0.02
628	60	8	0.7	...	0.50	3175	34	12	1.0	4	0.11	4666	28	15	1.4	...	0.09
660	44	55	5.4	22	0.17	3227	28	5	0.3	4	0.02	4736	32	9	0.6	0.4	0.07
891	14	36	3.6	12	0.12	3310	34	2	0.2	2	0.10	4826	47	14	1.2	0.4	0.07
908	42	12	1.0	...	0.17	3504	39	9	0.8	14	0.08	4945	35	125	15	...	0.11
972	30	13	0.8	23	0.06	3593	17	19	2.2	2	0.14	5033	21	9	0.6	4	0.06
Maf2	48	34	3.2	2	0.07	3627	48	10	1.1	1	0.08	5055	24	21	1.9	3	0.14
1055	23	26	1.7	...	0.11	3628	21	80	7.7	11	0.19	5135	20	9	0.7	58	0.09
1068	34	36	3.5	40	0.10	3690	22	22	1.9	...	0.15	5194	56	24	2.4	...	0.25
1084	35	6	0.4	...	0.06	4030	20	12	1.0	...	0.12	5236	19	31	2.9	0.9	0.08
1097	51	47	4.2	57	0.16	4038	42	15	1.1	15	0.11	5713	23	12	1.0	0.5	0.10
1365	43	60	6.0	98	0.12	4039	14	8	0.6	9	0.06	5775	20	9	0.7	15	0.07
I342	37	21	2.0	2	0.06	4051	23	17	1.6	5	0.35	6000	23	15	1.2	26	0.08
1614	11	11	0.7	82	0.09	4102	30	15	1.3	11	0.09	6240	09	7	0.5	...	0.04
1792	51	7	0.4	...	0.08	4254	51	7	0.3	23	0.04	6764	21	11	0.9	...	0.20
1808	32	16	1.4	7	0.05	4258	22	9	0.7	2	0.08	6946	38	43	3.9	2	0.08
2146	29	31	2.7	27	0.07	4293	24	4	0.4	...	0.05	6951	22	15	1.4	2	0.24
2273	37	4	0.2	7	0.05	4303	18	10	0.8	4	0.08	7331	61	16	1.4	...	0.45
2559	16	12	1.0	14	0.07	4321	29	34	3.3	14	0.20	7469	49	6	0.3	...	0.03
2623	38	4	0.2	50	0.06	4414	23	14	1.2	...	0.12	7541	83	19	1.5	...	0.27

Notes: N_H = 2000 N_C for the adopted gas-phase carbon abundance (Appendix C). M_{gas} = 1.35 M_H allowing for the presence of helium.

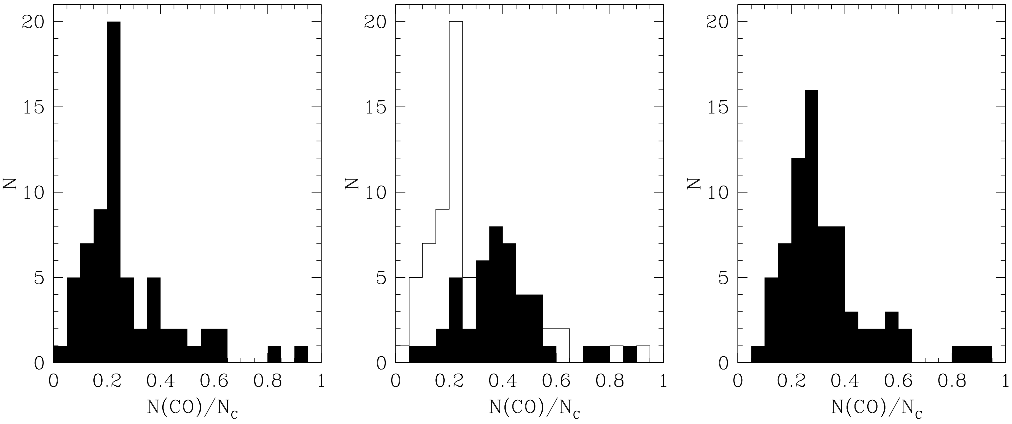

Fig. 13. Distribution of the fraction of all carbon contained in CO. Left: Results for an isotopological ratio of 40. Center: Results for an isotopological ratio of 80; for comparison, the distribution for the ratio of 40 is shown as well (unshaded). Right: Most probable distribution derived from both data sets (see text). Typically, one-third of the gas-phase carbon is in CO and two-thirds is in atomic or ionic form.

gas could not be determined; here we inserted the average value, denoted by a colon.

The analysis of ionized carbon is more problematical than that of the neutral carbon in the preceding section. Because the [CII] emission can be more extended and associated with dense hydrogen gas that is not traced by [CI] or CO emission, the CO parameters that we used to guide our [CI] analysis are now of little use. The 158μm [CII] line is the only strong C^+ emission line in the far-infrared, and if it is optically thin, the line-of-sight column density N_{C+} is related to the line intensity $I_{[CII]}$ (in K km s^{-1}) by Eq. (1) from Pineda *et al.* (2013): $N_{C+} = I_{[CII]} \times (3.05 \times 10^{15} (1 + 0.5(1 + 2840/n) e^{91.2/T})$. The temperatures and densities of the [CII]-emitting gas cannot be determined directly because there are three unknown parameters and only one equation. The equation provides a lower limit $N_{C+} = 4.6 \times 10^{15}$ I(CII) to the column density in the high-temperature, high-density limit, but no upper limit. We calculated C^+ column densities (Col. 6 of Table 10) for a more reasonable temperature T_k = 100 K and density $n(H_2)$ = 3000 cm^{-3}, so that $N_{C+} = 1.04 \times 10^{16}$ I(CII), doubling the high-T, high-n limit. The corresponding fractional abundances [C^+]/[C] are listed in Col. 12 of Table 10. They show a large spread; in particular, the values for NGC 2146, M 82, and NGC 4536 are quite high, which might indicate that their [CII] emission comes from gas that is denser and hotter than we have assumed. The derived central C^+/C fractions and the galaxy FIR luminosities are correlated, with considerable scatter. Because we calculated ionized carbon column densities for fixed temperatures and densities,

Table 10. Gas-phase carbon fractions

Name	$f_{[CII]}$	I[CII]	$I(CI)_{1-0}$	$I(CI)_{2-1}$	$N(C^+)$	$N(C^\circ)$	N(CO)	N_C	$\frac{[CO]}{[C]}$	$\frac{[C^\circ]}{[C]}$	$\frac{[C^+]}{[C]}$	Sum
			$K\,km\,s^{-1}$			$10^{17}\ cm^{-2}$						
(1)	(2)	(3)	(4)	(5)	(6)	(7)	(8)	(9)	(10)	(11)	(12)	(13)
253	0.86	569	256	154	59	70	66	215	0.30	0.33	0.28	0.91
891	0.58	53	8	4.8	6.6	4.0	5.0	36	0.14	0.11	0.18	0.43
1068	0.74	111	65	52	12	19	13	36	0.33	0.57	0.28	1.18
1097	0.72	52	21	15	5.4	13	25	47	0.51	0.28	0.12	0.91
1365	0.73	128	64	51	13	56	26	60	0.43	0.93	0.22	1.58
1482	0.90	88	6	4.8	9.2	2.6	2.0	18	0.11	0.15	0.53	0.79
1614	0.90	43	7	7	4.5	1.3	1.7	11	0.14	0.12	0.41	0.67
2146	0.89	431	24	29	45	5.8	9.0	31	0.28	0.20	1.57	2.05
2623	0.75	31	3	3	3.2	1.0	1.5	4	0.38	0.25	0.76	1.39
3034	0.60	892	123	185	93	27	33	83	0.39	0.33	1.12	1.74
3079	0.8:	86	28	...	8.9	5.6	10	42	0.30	0.14	0.22	0.66
3227	0.84	18	16	8	1.9	3.0	1.5	5	0.30	0.60	0.38	1.28
3627	0.89	27	11	3.3	2.8	5.1	5.1	11	0.47	0.47	0.25	1.19
3690	0.89	125	14	7	13	2.6	2.9	22	0.13	0.12	0.60	0.85
4038	0.89	47	4	3.6	4.9	1.6	5.7	15	0.42	0.12	0.38	0.92
4039	0.8:	55	6	2.4	5.7	0.7	1.2	9	0.14	0.08	0.67	0.89
4051	0.76	5	12	2.4	0.5	3.9	3.9	17	0.23	0.23	0.03	0.49
4254	0.65	15	6	1.2	1.6	2.9	3.6	7	0.51	0.41	0.22	1.14
4321	0.62	17	8	2.4	1.8	2.8	10	34	0.29	0.08	0.05	0.42
4536	0.92	94	2	3.2	9.8	1.4	2.7	10	0.28	0.14	0.98	1.40
4631	0.81	36	5	1.5	3.7	0.6	0.9	4	0.22	0.15	0.90	1.23
4736	0.77	12	6	3.6	1.2	3.0	2.7	9	0.32	0.33	0.13	0.78
4826	0.57	24	11	3.3	2.5	4.2	6.6	14	0.47	0.30	0.18	0.95
4945	0.8:	356	114	103	37	27	47	125	0.30	0.20	0.28	0.78
5055	0.77	12	8	2.4	1.2	2.4	5.0	21	0.24	0.11	0.06	0.41
5135	0.90	55	19	7.6	5.7	7.8	1.8	9	0.20	0.86	0.63	1.69
5194	0.60	18	5	2.0	1.9	6.5	13	24	0.56	0.72	0.21	1.49
5236	0.82	190	19	11	20	3.6	5.9	31	0.19	0.12	0.65	0.96
5713	0.90	46	3	1.2	4.8	1.8	2.7	12	0.24	0.18	0.48	0.90
6240	0.89	58	15	11	6.0	4.6	0.6	9	0.09	0.66	0.86	1.61
6946	0.82	45	17	5.1	4.7	7.3	18	34	0.38	0.24	0.15	0.77
7331	0.82	21	6	1.8	2.2	6.8	9.8	16	0.61	0.43	0.14	1.18
7469	0.81	37	16	8	3.8	2.5	2.9	1	0.49	0.42	0.61	1.52

Note: All data are reduced to the same 22" aperture. Column 1: Galaxy name; Cols. 2, 3, and 6: fraction, intensity, and column density of observed [CII] emission originating in neutral gas (see section 6.3); Cols. 4, 5, and 7: intensities and column density of the observed [CI] emission (see section 6.2); Cols. 8 and 9: CO and total carbon column densities (see Table C.2); Cols. 10, 11, and 12: relative contribution of CO, C°, resp. C^+ to total gas-phase carbon; Col. 13: sum of the three preceding columns; its deviation from unity is a measure of their accuracy, especially that of the least secure C^+ fraction (sections 6.3, 6.4).

this is loosely related to a correlation between [CII] and FIR intensities. No other clear pattern seems to emerge from the data in Table 10, consistent with significant variation in the physical conditions of the ISM and morphology even in galaxies that otherwise appear similar.

6.4. Carbon budget in galaxy centers

The combined column density of the three individual carbon gas-phase components listed in Col. 13 in Table 10 is generally close to the total gas-phase column density derived independently of the analysis of the ^{12}CO and ^{13}CO intensities sample (Table C.2). The average ratio of the two values is 1.06, with a standard deviation of 0.45. The consistency of these results underlines the validity of the analysis that produced them.

The relative amounts of the three gas components vary significantly among the observed galaxies, but the average fractional CO, C°, and C^+ contributions to the total C are quite similar. The respective contributions in the 33 galaxies are 0.32, 0.31, and 0.43, with standard deviations of 0.13, 0.23, and 0.36, respectively. The three forms of carbon occur in comparable amounts in the gas phase. Slightly less than one-third of all gas-phase carbon is in molecular form, and somewhat less than half of all gas-phase carbon is ionized.

As argued in section 6.1, the beam-averaged carbon monoxide column density is well constrained. In section 6.2, we argued that the [CI] emission arises from the same molecular gas, so that the beam-averaged neutral carbon column densities should likewise be robust. If the actual CO-to-C and C^o-to-C ratios were constant across the sample, the standard deviations would represent the measurement error in their determination. More realistically, they serve as upper limits to the uncertainty in the actual individual cases. The ionized carbon column densities are not so robust because they depend more strongly on assumptions. As we showed, there is a firm lower limit corresponding to very hot (T_k >250 K) and dense ($n_{H_2} > 10^5$ cm^{-3}) gas, so that the column densities in Table 10 can be lowered by a factor of two at most. In contrast, the [CII] line measurements do not define an upper limit. For instance, column densities would be higher by a factor of ten for modest temperatures $T_k \approx 50$ K and low densities

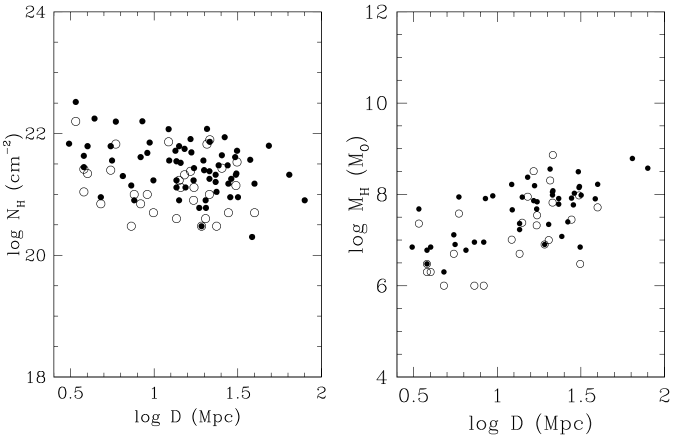

Fig. 14. Calculated beam-averaged column densities N_H (left) and central gas masses M_H (right) as a function of distance D. Filled circles: Values based on the preferred 'nominal' carbon abundance. Open circles: Values bases on extrapolated maximum carbon abundances (see text). All values are based on an assumed isotopological ratio of 40.

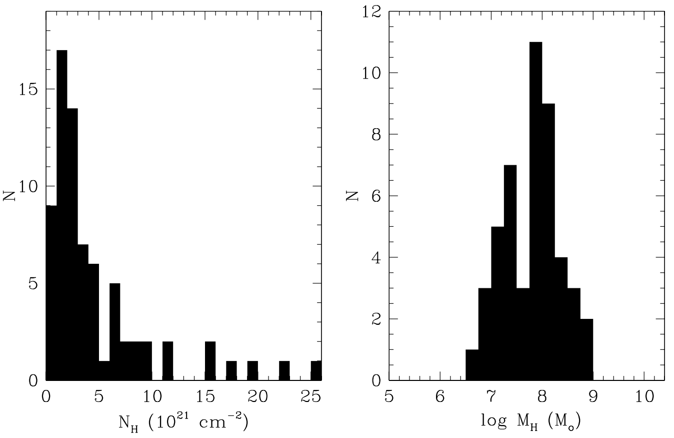

Fig. 15. Distribution of the total hydrogen column densities (left) and total hydrogen masses (right). See text for sample definition and errors.

$n_{H_2} \approx 300$ cm^{-3}. This is very unlikely because it requires the total carbon column densities N_C derived before to be underestimated by factors of five, incompatible with the models used. The corresponding very small CO fractions would also seem incompatible with the high-metallicity environment of galaxy centers as they are more characteristic of low-metallicity objects such as the Magellanic Clouds (Requena-Torres *et al.* 2016). As it is, modest temperature decreases to 60 K, or equally modest density decreases to 1000 cm^{-3}, implying 70% higher [CII] column densities, delineate the limits of what is feasible in view of the various uncertainties associated with Table 10.

7. Hydrogen column density and mass

Total hydrogen column densities N_H would follow directly from the carbon column densities N_C if the gas phase carbon-to-hydrogen abundance were directly known, which is not the case. Instead, we must infer this abundance from our knowledge of (i) the relative oxygen abundance [O]/[H], (ii) the relative carbon abundance [C]/[O], and (iii), the fraction δ_C of all carbon that is in the gas phase rather than locked up in dust grains. Based on the detailed discussion in Appendix D, we adopt for all galaxy centers a metallicity of twice that of the solar neigborhood, identical [C] and [O] abundances and a carbon depletion factor $\delta_C = 0.5 \pm 0.2$. This yields a 'nominal' (N) gas phase ratio $N_H/N_C = (2 \pm 1) \times 10^3$. In Table D.1 we list the implied beam-averaged total hydrogen column densities N_H for a range of assumptions, as well as the derived molecular hydrogen column densities N_{H_2} and overall hydrogen gas masses M_H. The adopted nominal values are summarized in Table 9. The beam-averaged molecular hydrogen column densities N_{H_2} (Col. 4) are corrected for the (small) contribition by HI. The total gas masses M_{gas} (Col. 5) incorporate a 35% contribution by helium. As discussed in Appendix D, the uncertainty in individual values of N_H and M_H, hence also in N_{H_2} and M_{gas}, is a factor of slightly more than two.

In Fig. 14 we plot N_H and M_H as a function of galaxy distance D for both the nominal N and the extrapolated E carbon abundance. The Galactic abundance case G is not shown, but would be represented by points offset from the nominal abundance points by +1.7 in the log. The hydrogen gas column densities peak in the center, causing beam-averaged column column densities to decrease with galaxy distance as ever larger linear areas are covered by the fixed 22" beam. At the same time, the encompassed hydrogen mass increases with distance when the beam includes ever larger areas of the galaxy disk.

Figure 15 shows the distributions of N_H and M_H. We merged the two isotopological abundance data sets and averaged values where appropriate. The column densities have a well-defined peak at about $N_H = 1.5 \times 10^{21}$ cm^{-2}, with a tail to higher values primarily caused by long sight-lines through highly tilted galaxies. The mass distribution shows a wide range of values from 10^6 M$_\odot$ to 10^9 M$_\odot$ with a broad peak around a few times 10^7 M$_\odot$ and a narrow peak around 10^8 M$_\odot$. Fig 14 shows that with a few exceptions, the higher masses are all found in galaxies at distances of 10 Mpc or more and mostly refer to the 'inner disks' in Fig. 10. The lower masses are found over a wider range of distances, from 4 to 25 Mpc, and thus characterize both 'circumnuclear disks' and low-mass 'inner disks'.

8. CO as a tracer of H_2

8.1. Conversion factors X(CO), X[CI], and X[CII]

We are now in a position to consider to what extent CO, [CI], or [CII] line intensyies trace H_2 molecular gas column densities. In Fig. 16 we plot the N_{H_2} column densities from Table 9 as a function of the J=1-0 CO, [CI], and [CII] line intensities from Tables 2 and 10. In each panel, the dashed line marks the relation between the two quantities with a slope corresponding to the X factor. Because the same molecular hydrogen column densities are plotted as a function of the observed line intensities, the results are not subject to the uncertainties that plague the determination of neutral and ionized carbon column densities discussed in Sections 6.2 and 6.3. The distribution of the individual X values is shown in Fig. 17 for each line. Inasmuch as the dispersion exceeds the observational error, the dispersion around the mean X value is an important quantity to judge the relative performance of each of the three lines in predicting the molecular gas column density.

The individual I_{CO}-to-$N(H_2)$ ratios occur in a fairly narrow range, ten times below the commonly assumed Milky Way solar neighborhood conversion factor $X_{MW} = 2.0 \times 10^{20}$ cm^{-2}/ K km s^{-1}. A linear regression fit on I_{CO} and $N(H_2)$ yields a high-quality solution ($r^2 = 0.78$) corresponding to a conversion factor that is very close to the average of the individual I_{CO}-to-$N(H_2)$ ratios: $X(CO) = (1.9 \pm 0.2) \times 10^{19}$ cm^{-2}/ K km s^{-1} .

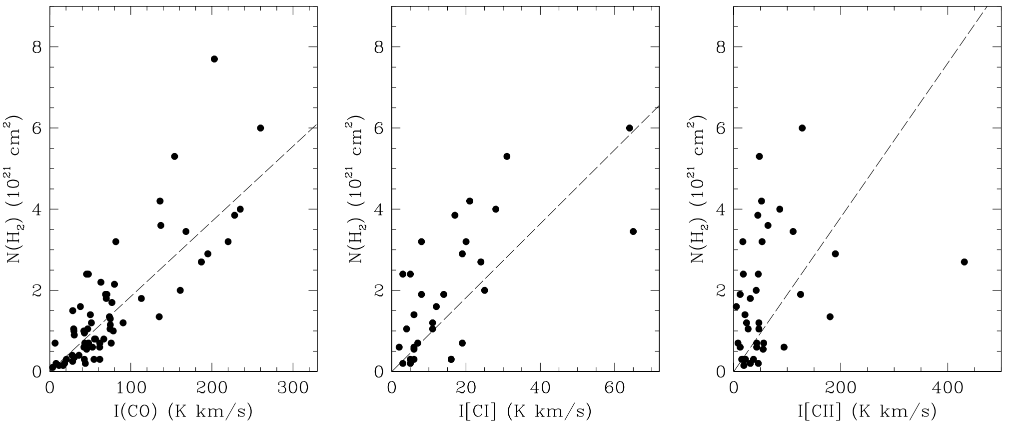

Fig. 16. Column densities N_{H_2} as a function of (left) CO, (center) [CI], and (right) [CII] intensities. Points representing the nearby bright galaxies NGC 253, NGC 3034 (M82), and NGC 4945 are outside the box limits. Dashed lines are linear regression fits to all data points, including these galaxies. The fits correspond to conversion factors X(CO) = 1.9 × 10^{19} cm^{-2}/ K km s^{-1} and X[CI] = 9.1 × 10^{19} cm^{-2}/ K km s^{-1}. There is no meaningful fit for $I(CII)$.

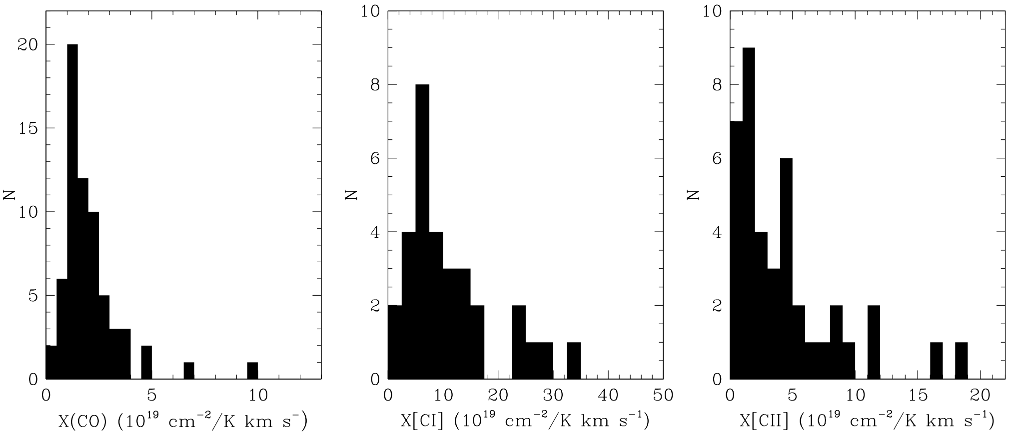

Fig. 17. From left to right: Distributions of the CO-to H$_2$, [CI]-to H$_2$, and [CII]-to H$_2$ conversion factors X(CO), X[CI], and X[CII]. See text for sample definition and errors.

The average X-factor applicable to galaxy centers is quite robust and well defined even when individual CO-to-hydrogen conversion factors are still subject to uncertainties of a factor of two.

A similar regression fit on the much lower intensities of the neutral carbon line (Fig 16 central panel) yields a five times higher value X [CI] = $(9 \pm 2) \times 10^{19}$ cm^{-2}/ K km s^{-1}>. The average of the individual values is almost twice as high, with a large standard deviation. This is caused by the cluster of low-intensity, low-column-density points in the lower left corner of the central panel in Fig. 16, and it suggests that [CI] intensities are useful but less reliable as N(H$_2$) indicators than CO.

The linear regression fit on all [CII] intensities gives a value (1.9 ± 0.5) × 10^{19} cm^{-2}/ K km s^{-1} with very low significance (r^2 = 0.07). The average is more than twice as high, $(4.4 \pm 0.8) \times 10^{19}$ cm^{-2}/ K km s^{-1}. These [CII] intensities include a contribution from ionized gas. If corrections were included, the $N_{H_2}/I(CII)$ slopes would be steeper by about 20%, but the relative distribution of points would suffer little change. In any case, from both Figs. 17 and 16 it follows that the present data do not define a clear-cut single value for X([CII]).

Following Wada & Tomisaka (2005), we also considered the ^{12}CO J=3-2 intensities as a tracer for N(H$_2$). Their three-dimensional, non-LTE radiative transfer calculations for circumnuclear molecular gas disks predict that the J=3-2 line is more useful than the J=1-0 line as a tracer for N(H$_2$) and they suggest a conversion factor of ∼ 2.7 × 10^{19} cm^{-2}/ K km s^{-1} for this transition. Our linear regression fit yields a value (2.1 ± 0.4) × 10^{19} cm^{-2}/ K km s^{-1}. There is considerable scatter around this value and the average comes out higher, at (3.1 ± 0.3) × 10^{19} cm^{-2}/ K km s^{-1}. We conclude that the X(CO3-2) value calculated by Wada & Tomisaka (2005) is very close to the actual value following from our work, but that X(CO1-0) is still the better performer, contradictory to their expectations.

In a previous paper, Israel *et al.* (2015) discussed the suggestion by Papadopoulos *et al.* (2004) and others that [CI] line emission might provide a tracer of molecular hydrogen at least as good as CO emission. The above discussion, and indeed inspection of the CO, and [CI] panels in Figs. 17 and 16, establishes that the scatter is somewhat greater in the [CI] diagrams and that the X[CI] distribution is less strongly peaked than the X(CO) distribution. This result confirms and expands our earlier conclusion that the J=1-0 ^{12}CO line should be preferred over the [CI] line as a molecular gas tracer if both are available. If only the [CI] line is accessible, as may be the case for redshifted objects, it should be regarded as an acceptable substitute, provided an adequate calibration can be established for the differing environmental conditions.

The scatter in the [CII] diagrams is much greater than that in either the ^{12}CO or [CI] counterparts, and our data do not establish a convincing unique value of X [CII]. It follows that [CII] intensities are not a useful tracer of extragalactic molecular gas column densities, and given the minor contribution of HI, are not a useful tracer of total gas either.

8.2. Low *X(CO)* and H$_2$ *mass in galaxy centers*

In the above, we have come to the conclusion that molecular hydrogen column densities and masses in the centers of galaxies are an order of magnitude lower than suggested by the 'standard' conversion factor. This conclusion depends to some extent on the correctness of the carbon abundances assumed in the derivation. If, for instance, these were substantially lower, as in the Pilyugin *et al.* (2014) calibration already mentioned, the distribution of the individual X factors would still be similar to that depicted in Fig. 17, but it would be shifted upward to a mean value X(CO) = 5×10^{19} $\mathrm{cm^{-2}/\,K\,km\,s^{-1}}$. Even then, the conversion factors would still be over four times lower than the local Milky Way disk factor $X_{\circ}$.

Our results fit the historical downward trend of the published values of X in galaxy centers as opposed to galaxy disks.Sandstrom *et al.* (2013) studied the disks of 26 nearby galaxies, many in common with our survey. They derived a more or less constant factor $X = 1.95 \times 10^{20}$ from ^{12}CO(2-1), FIR, and HI emission, but suggested a lower central X. Follow-up J=1-0 ^{12}CO and ^{13}CO observations of nine nearby galaxies led Cormier *et al.* (2018) to a similar result, with a low average center $X \sim 0.15\,X_{\circ}$ which, fortuitously, happens to be close to our result. Even lower X factors of about $0.05\,X_{\circ}$ are now discussed for the more extreme case of optically thin CO gas outflows from the centers of nearby luminous galaxies (Alatalo *et al.* 2011; Sakamoto *et al.* 2014; Oosterloo *et al.* 2017)

As the low X value of the ISM in the center of our own galaxy is thus revealed to be characteristic of galaxy centers in general, it is instructive to take a closer look at the well-studied Central Molecular Zone (CMZ) in the Milky Way. The density of most of the gas in the CMZ is not very high. High-density molecular tracers other than CO are generally subthermally excited, implying densities of only $\sim 10^4$ $\mathrm{cm^{-3}}$ (Jones *et al.* 2012). Observations of J=1-0 ^{12}CO and its optically thin isotope C^{18}O have shown very complex molecular gas distributions characterized by moderate or low optical depths (Dahmen *et al.* 1998) on large scales. Observations of several ^{12}CO and ^{13}CO transitions (but not including the J=1-0 transition) rule out excitation by a single component and instead suggest the superposition of various warm gas phases (Requena-Torres *et al.* 2012). Requena-Torres and collaborators performed a two-component LVG analysis, analogous to the one in this paper, that suggested a dominant phase with $T_{\mathrm{kin}} \approx 200$ K and a density $n(\mathrm{H_2}) \sim 3 \times 10^4$ $\mathrm{cm^{-3}}$ and a minor phase (20-30% by mass) with a higher $T_{\mathrm{kin}} \approx$ 300-500 K, $n(\mathrm{H_2}) \sim 2 \times 10^5$ $\mathrm{cm^{-3}}$. The lack of the low-J transition biases their analysis to higher densities and temperatures, whereas our coverage of all lower transitions up to J=3-2 or J=4-3 samples the lowest temperatures in phase 1, but may underestimate phase 2 temperatures.

The bulk of the CMZ molecular gas has temperatures T_{kin} = 50 - 120 K, and the average gas temperature outside the densest clouds is 65 ± 10 K (Ao *et al.* 2013, Ginsburg *et al.* 2016). Both the temperature range and the average temperature are very similar to those of our sample of galaxy centers (cf. Table C.2), for which we find a mass-weighted mean temperature $T_{\mathrm{kin}} = 55 \pm 5$ K. The emission-weighted mean gas density of the galaxy centers in our sample, $n_{\mathrm{H_2}} = (1.8 \pm 0.6) \times 10^4$ $\mathrm{cm^{-3}}$, is likewise similar to the values obtained for the CMZ.

Requena-Torres *et al.* (2012) concluded that the gas sampled by them is not organized by self-gravity, is unstable against tidal disruption, and is transient in nature. Velocity dispersions of clouds in the Galactic center region are five times higher than those of clouds in the disk (Miyazaki & Tsuboi, 2000). This, the widespread presence of shocked gas emitting in the J=2-1 SiO line (Hüttemeister *et al.* 1998), and the high but variable gas temperatures throughout the CMZ noted by Requena-Torres *et al.* (2012) indicate that the dense gas is dominated by turbulent heating. Neither heating by UV photons nor by cosmic rays can be important on global scales in the CMZ (Ao *et al.* 2013, Ginsburg *et al.* 2016), as we have also concluded in the individual cases of NGC 253 and NGC 3690 after detailed modeling of molecular line data (Rosenberg *et al.* 2014a, b).

The picture that emerges of the molecular gas in the CMZ, and by implication also in the observed galaxy centers, is very different from the picture of the star-forming molecular gas in the disk of the Milky Way and other galaxies. In the CMZ, molecular gas appears to occur mostly in extended diffuse clouds with modest optical depths in CO but with relatively high surface filling factors. This warm gas does not only rotate rapidly around the nucleus, but is also continuously stirred up and rather turbulent, even though the precise mechanisms are not yet clear (see, e.g., the review by Mills, 2017).

That CO-to-$\mathrm{H_2}$ conversion factors are much lower for molecular gas in galaxy centers than in galaxy disks can be understood in terms of different physical properties. For instance, Stacey *et al.* (1991) already suggested that higher excitation temperatures were responsible for the drop in X(CO) implied by their [CII] measurements. Downes & Solomon (1998) speculated that the central CO in luminous galaxies is only moderately opaque and highly turbulent. They also believed it to be subthermally excited, but higher J CO intensities show this to be an oversimplification. More recently, models and simulations have started to elucidate the effects of different environments on empirical quantities such as X. In one example, Bell *et al.* (2006) used photon-dominated region (PDR) time-dependent chemical models to show that increases in density, cosmic-ray ionization rate, metallicity, and turbulent velocity all act to depress X-values. Bell et al. (2007) explicitly noted that application of their models to M 51 and NGC 6946 yielded results that are very close to those obtained by us and ascribed the low X values primarily to high density and metallicity. In another example, Narayanan *et al.* (2011) combined smoothed particle hydrodynamics (SPH) simulations of galaxy disks with physical and radiative transfer ISM models and the CO-to-$\mathrm{H_2}$ conversion factor in star-forming and merger galaxy disks. Although their results do not directly apply to galaxy centers, they do draw attention to the significant dependence of X on kinetic temperature and velocity dispersion.

The bulk of the gas in galaxy centers is, like that in the CMZ, carbon rich, moderately dense, warm, and turbulent. With respect to $\mathrm{H_2}$ column density, the higher CO abundance and emissivity increase the CO line intensity, whereas lower CO mean optical depth imply lower $\mathrm{H_2}$ column densities relative to CO intensity. Thus, in galaxy centers, the molecular gas radiates in CO with much enhanced efficiency. The gains thus made by galaxy center molecular gas with respect to disk gas can be quantitatively estimated from the model dependencies $X \propto T^{-1/2}$ and $X \propto \sigma^{-1/2}$ derived for the CO-to-$\mathrm{H_2}$ conversion factor by Shetty *et al.* (2011). The thrice higher carbon gas phase abundance leads to a three times lower X. The elevated average kinetic temperature of 55 K lowers X by a further factor of two. Most of the central CO is of modest optical depth, and taking our cue from the five times higher CMZ velocity dispersions, another drop in X by a factor of 2.2 is to be expected. Taking all together, we would expect $X \approx 1.5 \times 10^{19}$ $\mathrm{cm^{-2}/\,K\,km\,s^{-1}}$ (or $0.075\,X_{\circ}$), which is very close to the average value $X \approx 1.9 \times 10^{19}$ ($\mathrm{cm^{-2}/\,K\,km\,s^{-1}}$) from Section 8.1. This agreement shows that the conditions causing the low value of central X are reasonably well understood. It also shows that no single cause prevails; all three contributing factors are of a similar magnitude, and all three are needed.

9. Conclusions

1. We determined intensities of galaxy centers in the lowest J transitions of ^{12}CO and ^{13}CO. Out of a total of 126 galaxies 112, 103, 88, and 24 were measured in the J=1-0, J=2-1, J=3-2, and J=4-3 transitions of ^{12}CO, respectively, as well as 89, 71, and 61 in the J=1-0, J=2-1, and J=3-2 transitions of ^{13}CO, respectively. In 15 galaxies, only the J=1-0 transition was measured and 30 galaxies lack ^{13}CO measurements[6].
2. Multi-aperture J=1-0 ^{12}CO fluxes from the survey and the literature show that CO luminosities increase roughly linearly with observing beam size. The extrapolated CO-emitting gas extends to $\sim$ 40% of the optical size D_{25} and $\sim$ 25% of the HI size. The molecular gas is thus much more concentrated than the atomic gas.
3. The ^{12}CO J=1-0 to J=4-3 transition ladder has relative intensities 1.00 : 0.92 : 0.70 : 0.57. The mean isotopologue ^{12}CO-to- ^{13}CO intensity ratios are 13.0 ± 0.7 (J=1-0), 11.6 ± 0.6 (J=2-1), 12.8 ± 0.6 (J=3-2), but individual values may be as low as 5 and as high as 25.
4. For more than 70 galaxies, physical parameters of a two-phase gas were determined with the use of non-LTE radiative transfer models (*RADEX*). On average, only one-third of the gas-phase carbon ($32 \pm 8\%$) is found to reside in CO. The full gas-phase carbon budget was determined for 45 galaxies, using literature data for neutral and ionized carbon line intensities. The intensities of the [CI] and ^{12}CO lines are closely related; on average, neutral carbon C° accounts for somewhat less of the gas-phase carbon ($30 \pm 4\%$). Somewhat more than one-third of the gas-phase carbon is available for ionized carbon C^+. This condition is met if [CII] emission originates in a moderately dense and warm ($n \geq 3000$ cm^{-3}, $T \geq 100$ K) gas.
5. Averaged over a 22" beam, mean total hydrogen column densities are $N_{\rm H} = (3.3 \pm 0.2) \times 10^{21}$ cm^{-2} and mean molecular hydrogen column densities are $N({\rm H_2}) = (1.5 \pm 0.2) \times 10^{21}$ cm^{-2}. Total gas masses of central molecular zones up to one kiloparsec radius are typically a few times 10^7 M$_\odot$, whereas the total molecular gas masses of the inner disk are typically 10^8 M$_\odot$.
6. The observed J=1-0 CO intensities and the derived $N({\rm H_2})$ values yield CO-to H$_2$ conversion factors with a well-defined mean value $X(CO) = (1.9 \pm 0.2) \times 10^{19}$ cm^{-2}/ K km s^{-1}. This is a factor of ten below the 'standard' solar neighborhood Milky Way factor $X_{\rm MW}$. The mean [CI]-to H$_2$ conversion factor is $X[CI] = (9 \pm 2) \times 10^{19}$ cm^{-2}/ K km s^{-1}. There is no meaningful conversion factor for [CII].
7. Use of a conversion factor based on J=3-2 ^{12}CO line intensities yields results that are better than those obtained with [CI], but not as good as those derived from the J=1-0 ^{12}CO line.
8. From comparisons with the well-studied CMZ in the Milky Way galaxy, it appears that the order-of-magnitude decrease of the CO-to- H$_2$ conversion factor in the central molecular zones of nearby other galaxies with respect to canonical galaxy disk conversion factors is caused in equal parts by the higher gas-phase carbon abundances in galaxy centers, elevated kinetic gas temperatures, and high molecular cloud velocity dispersions.

---

[6] The raw JCMT data are publicly available from the CADC JCMT Science Archive at https://www.cadc-ccda.hia-iha.nrc-cnrc.gc.ca/en/jcmt/ . Neither SEST nor IRAM data are archived, but the processed galaxy data from this paper can be downloaded in CLASS format from ftp://ftp.strw.leidenuniv.nl/pub/israel/data/galaxyfiles

Acknowledgements

Some of the SEST and IRAM observations and most of the JCMT observations were made in service mode. With gratitude I acknowledge my indebtedness to the many colleagues and facility staff, above all the JCMT operators, who over many years helped to collect the large and unique data base described in this paper. It is fitting to commemorate the generous advice and assistance of Lars E.B. Johansson (SEST) and Fred Baas (JCMT), both of whom sadly died before they could see the results. I also thank Thijs van der Hulst for supplying his unpublished SEST observations of NGC 613, NGC 1097, and NGC 1365 as well as Rodrigo Herrera-Camus for sharing his machine-readable [CII] data in advance of publication. Critical comments by the referee, Jonathan Braine, led to a substantial improvement of the paper. We made extensive use of the JCMT archive part of the facilities of the Canadian Astronomy Data Centre operated by the National Research Council of Canada with the support of the Canadian Space Agency.

References

Aalto, S., Black, J.H., Booth, R.S., & Johansson, L.E.B., 1991a, *A&A* 247, 291
Aalto, S., Black, J.H., Johansson, L.E.B., & Booth, R.S., 1991b, *A&A* 249, 326
Aalto, S.; Booth, R. S.; Black, J. H.; & Johansson, L. E. B. 1995, *A&A* 300, 369
Adler, D.S., & Liszt, H.S., 1989 *ApJ* 339, 836
Alatalo, K., Blitz, L., Young, L.M., et al., 2011, *ApJ* 755, 88
Albrecht, M., Kr ugel, E., & Chini, R., 2007, *A&A* 462, 575
Ao, Y., Henkel, C., Menten, K.M., et al., 2013, *A&A* 550, A135
Baan, W.A., Hagiwara, Y., & Hofner, P., 2007 *ApJ* 661, 173
Bajaja, E., Wielebinski, R., Reuter H.-P., Harnett, J., & Hummel, E., 1995, *A&A Suppl* 114, 147
Bayet, E., Gerin, M., Phillips, T.G., & Contursi, A., 2004, *A&A* 427, 45
Becker, R., & Freudling, W., 1991, *A&A* 252, 454
Berg, D.A., Skillman, E.D., Henry, R.B.C., Erb, D.K., & Carigi, L., 2016, *ApJ* 827, 126
Blanc, G.A., Schruba, A., Evans, N.J., et al., 2013, *ApJ* 764, 117
Blitz, L., Bloemen, J.B.G.M., Hermsen, W., & Bania, T.M., 1985, *A&A* 143, 267
Bosma A., 1981, *AJ* 86, 1791
Braine, J., Combes, F., Casoli, F., et al., 1993a, *A&A Suppl* 97, 887
Braine, J., Combes F., & van Driel W., 1993b, *A&A* 280, 451.
Braine, J., Guelin, M., Dumke, M., Brouillet, N., Herpin, F., & Wielebinsky, R., 1997, *A&A* 326, 963
Brand, J., Wouterloot, J., Becker, R., & Stirpe, G.M., 1989, *A&A* 211, 315
Braun R., Walterbos R.A.M., Kennicutt Jr. R.C., & Tacconi L.J., 1994, *ApJ* 420, 558
Brinks, E., Skillman, E.D., Terlevich, R.J., & Terlevich, E., 1997, Ap&SS, 248, 23
Bushouse, H.A., Lord, S.D., Lamb, S.A., Werner, M.W., & Lo, K.Y., 1999, unpublished preprint arXiv:astro-ph/9911186
Cayatte, V., van Gorkom J.H., Balkowski C, & Kotanyi C., 1990, *AJ* 100, 604
Casasola, V., Hunt, L.K., Combes, F., García-Burillo, & Neri, R., 2011, *A&A* 527, 92
Casoli, F., Dupraz, C., Combes, F., & Kazès, I., 1991, *A&A* 251, 1
Casoli, F., Dupraz, C., & Combes, F., 1992, *A&A* 264, 49
Casoli, F., & Gerin, M., 1993, *A&A* 279, L41
Chengalur, J.N., Salpeter E.E., & Terzian Y., 1994, *AJ* 107, 1984
Chini, R., Krügel, E., & Steppe, H., 1992, *A&A* 255, 87
Chini, R., Krügel, E., & Lemke, R., 1996, *A&A Suppl* 118, 47
Chung, A., van Gorkom, J.H., Kenney, J.D.P., Crowl, H., & Vollmer, B., 2009, *AJ* 38, 1741
Chung, E.J., Rhee, M.-H., Kim, H., Yun, M.S., Heyer, M., & Young, J.S. 2009 *ApJS* 184, 199
Claussen, M.J.M & Sahai, R., 1992, *AJ* 103, 1134
Cormier, D., Bigiel, F., Jiménez-Donaire, M.J., et al., 2018, *MNRAS* 475, 3909
Costagliola, F., Aalto, S., Rodriguez, M.I.and 10 co-authors, 2011, *A&A* 528, A30
Cox, P.,& Downes, D., 1996, *ApJ* 473, 219
Crosthwaite, L.P.,Turner, J.L., & Ho, P.T.P, 2000, *AJ* 119, 1720
Crosthwaite, L.P., & Turner, J.L., 2007, *AJ* 134, 1827
Croxall, K.V., Smith, J.D., Pellegrini, E.., and 17 co-authors, 2017, *ApJ* 845, 96
Curran, S.J., Johansson, L.E.B., Bergman, P., Heikkilä, A., & Aalto, S., 2001 *A&A* 367, 457
Dahlem, M., Aalto, S., Klein, U., Booth, R., Mebold, U., Wielebinski, R., & Lesch H., 1990, *A&A* 240, 237

Dahlem M., 1992, *A&A* 264, 483

Dahlem, M., Golla, G., Whiteoak, J.B., Wielebinski, R., Hüttemeister, S., & Henkel, C., 1993, *A&A* 270, 29

Dahmen, G., Hüttemeister, S., Wilson, T.L., & Mauersberger, R., 1998, *A&A* 331, 959

Davies, R.I., Tacconi, L.J., Genzel, R., 2004, *ApJ* 602, 148

Díaz-Santos, T., Armus, L., Charmandaris, V., and 20 co-authors, 2017, *ApJ* 846, 32

Dettmar, R.-J., & Heithausen, A., 1989, *ApJL* 344, L61

Devereux, N., Taniguchi, Y., Sanders, D.B., Nakai, N., & Young, J.S., 1994, *AJ* 107, 2006

Downes, D., & Solomon, P.M., 1998 *ApJ* 507, 615

Dumke, M., Nieten, Ch., Thuma, G., Wielebinski, R., & Walsh, W., 2001, *A&A* 373, 853

Eckart, A., Cameron, M., Jackson, J.M., et al., 1991, *ApJ* 372, 67

Elfhag, T., Booth, R.S., Höglund, B., Johansson, L.E.B., & Sandquist, 1996, *A&A Suppl* 115, 439

Encrenaz, P.J., Stark, A.A., Combes, F., & Wilson, R.W., 1979, *A&A* 78, L1

Esteban, C., García-Rojas, J.., Carigi, L., et al., 2014, *MNRAS* 443, 624

Fernández-Ontiveros, J.A., Spinoglio, L., Pereira-Santaella, M., Malkan. M.A., Andreani, P., & Dasyra, K.M., 2016, *ApJS* 226, 19

Garcia-Barreto, J.A., Dettmar, R.-J., Combes, F., Gerin, M.,& Koribalski, B., 1991, *Rev. Mex. A&A* 22, 197

Garay, G., Mardones, D., & Mirabel, I.F., 1993, *A&A* 277, 405

García-Burillo, S., Sempere, M.J., Combes, F., & Neri, R., 1998, *A&A* 333, 864

García-Burrillo, S., Sempere, M.J., Combes, F., Hunt, L.K., Neri, R., 2000, *A&A* 363, 869

Garciá-Burillo, S., Combes, F., Hunt, L.K., and 8 co-authors, 2003, *A&A* 407, 485

Garnett, D.R., Shields, G.A., Peimbert, M., et al., & Terlevich R.J., 1999, *ApJ* 513, 168

Garnett, D.R., Edmunds, M.G., Henry, R.B.C., Pagel, B.E.J., & Skillman, E.D., 2004, *AJ* 128, 2772

Gerin, M., Nakai, N., Combes, F., 1988, *A&A* 203, 44

Gerin, M., Casoli, F., & Combes, F., 1991, *A&A* 251, 32

Gerin, M., & Liszt H., 2017, *A&A* 600, A48

Giannetti, A., Wyrowski, F., Brand, J., et al., 2015, *A&A* 570, A65

Ginsburg, A., Henkel, C., Ao, Y., et al., 2016, *A&A* 586, A50

Glenn, J., & Hunter, T.R., 2001 *ApJ* 135, 177

Golla & Wielebinsky, 1994, *A&A* 286, 733

Haan, S., Schinnerer, E., Mundell, C.G., Garcia-Burillo, S., & Combes, F., 2008, *AJ* 135, 232

Hafok, H., & Stutzki, J., 2003, *A&A* 398, 959

Harrison, A., Henkel, C., & Russell, A., 1999, *MNRAS* 303, 157

Heckman, T.M., Blitz, L., Wilson, A.S., Armus, L., & Miley, G.K., 1989, *ApJ* 342, 735

Helfer, T., & Blitz, L, 1995, *ApJ* 450, 90

Helfer, T.T., Thornley, M.D., Regan, M.W., et al., 2003, *ApJS* 145, 259

Henkel, C., Whiteoak, J.B., Nyman, L.-A., & Harju, J., 1990, *A&A* 230, L5

Henkel C., Whiteoak J.B., & Mauersberger R., 1994 *A&A* 284, 17

Henkel C., Chin Y.-N, Mauersberger R. & Whiteoak J.B., 1998 *A&A* 329, 443

Henkel C., Asiri, H., Aalto, S., et al., 2014 *A&A* 565, A3

Herrera-Camus, R., Sturm, E., Gracía-Carpo J., and 13 co-authors, 2018, *ApJ* , 861, 94

Hibbard, J.E., van Gorkom, J.H., Rupen, M.P., & Schiminovich, D., 2001, in ASP Conf. Ser. 240, (ASP, San Francisco), 659

Hitschfeld, M., Aravena, M., Kramer, C., et al., 2008, *A&A* 479, 75

Houghton, S., Whiteoak, J.B., Koribalski, R., Booth, R., Wiklind, T., & Wielebinski, R., 1996, *A&A* 325, 923

Huchtmeier, W.K., & Tammann, G.A., 1992, *A&A* 257, 455

Huchra, J., & Burg, R., 1992, *ApJ* 393, 90

Hurt, R.L., Turner, J.L.;, & Ho, P.T.P., 1996, *ApJ* 466, 135

Hüttemeister, S., Dahmen, G., Mauersberger, R., Henkel, C., Wilson, T.L., & Martín-Pintado, J., 1998, *A&A* 334, 646

Irwin, J.A., 1994 *ApJ* 429 618

Israel, F.P., White, G.J., Baas, F., 1995, *A&A* 302, 343

Israel, F.P., Baas, F., 1999, *A&A* 351, 10

Israel, F.P., Baas, F., 2001, *A&A* 371, 433

Israel, F.P., Baas, F., 2002, *A&A* 383, 82

Israel, F.P., Baas, F., 2003, *A&A* 404, 495

Israel, F.P., Baas, F., 2006, *A&A* 445, 907

Israel, F.P., 2009a, *A&A* 493, 525

Israel, F.P., 2009b, *A&A* 506, 689

Israel, F.P., 2015, *A&A* 578, A95

Jenkins, E.B., 2009, *ApJ* 700, 1299

Jones, P.A., Burton, N.G., Cunningham, M.R., Tothill, N.F.H., & Walsh, A.J., 2012, *MNRAS* 419,2961

Jörsäter, S., & van Moorsel, G.A., 1995, *AJ* 110, 2037

Kamenetzky, J., Rangwala, N., Glenn, J., Maloney, P.R., & Conley, A., 2016, *ApJ* 829, 93

Kaneko, N., Morita, K., Fukui, Y., and 5 co-authors, 1989, *ApJ* 337, 691

Kenney, J.D., & Young, J.S., 1988, *ApJS* 66, 261

Knapen, J.H., Cepa, J., Beckman, J.E., Soledad del Rio, M., & Pedlar, A., 1993, *ApJ* 416, 563

Knapen, J.H., Whyte, L.F., de Blok, W.J.G., & van der Hulst, J.M., 2004, *A&A* 423, 481

Koda, J., Sofue, Y., Kohno, K., Nakanishi, H., Onodera, S., Okumura, S.K., & Irwin, J.A., 2002, *ApJ* 537, 105

Koda, J., & Sofue, Y., 2006, *PASJ* 58, 299

Kohno, K., Kawabe, R., & Vila-Vilaró, B., 1999, *ApJ* 511, 157

Kohno, K., Vila-Vilaró, B., Sakamoto, S., Kawabe, R., Ishizuki, S., & Matsushita, S., 2003, *PASJ* 55, 103

Komugi, S., Sofue, Y., Kohno, K., Nakanishi, H., Onodera, S., Egusa, F., & Muraoka, K., 2008, *ApJS* 178, 225

Krause, M., Fendt, C., & Neininger, N., 2007, *A&A* 467, 1037

Kregel, M., & Sancisi, R., 2001,*A&A* 386, 59

Krips, M., Crocker, A.F., Bureau, M., Combes, F., & Young, L.M., 2010, *MNRAS* 407, 2261

Kuno, N., Tosaki, T., Nakai, N., & Nishiyama, 1997, *PASJ* 49, 725

Kuno, N., Nishiyama, K., Nakai, N., et al., 2000 *PASJ* 52, 775

Kuno, N., Sato, N., Nakanishi, H., et al., 2007, *PASJ* 59, 117

Liszt, H.S., & Dickey, J.M., 1995, *AJ* 110 998

Lu, N., Zhao, Y., Díaz-Santos, T., and 18 co-authors, 2017, *ApJS* 230, 1

Lucero, D.M., Carignan, C., Elson, E.C., *et al.*, 2015, *MNRAS* 450, 3935

Lundgren, A.A., Wiklind, T., Olofsson, H., & Rydbeck, G., 2004, *A&A* 413, 505

Maiolino, R., & Rieke, G.H., 1995, *ApJ* 454, 95

Maiolino, R., Ruiz, M., Rieke, G.H., & Papadopoulos, P., 1997, *ApJ* 485, 552

Maloney, P., & Black, J.H., 1988, *ApJ* 325, 389

Maloney, P., 1990, *ASSL* 161, 493

Mao, R.Q., Henkel, C., Schulz, A., and 5 co-authors, 2000, *A&A* 358, 433

Mao, R.-Q., Schulz, A., Henkel, C., Mauersberger, R., Muders, D., & Trung, D.-V, 2010, *ApJ* 724, 1336

Martín, S., George, M.R., Wilner, D.J., Êspada, D., 2010, *AJ* 139, 2241

Mason, A.M., & Wilson, C.D., 2004, *ApJ* 612, 860

Mauersberger R., Henkel C., Walsh, W., & Schulz, A., 1999 *A&A* 341, 256

Meijerink, R., Kristensen, L.E., Weisz, A., and 28 co-authors, *ApJL* 762, L16

Mills, E.A.C., 2017, Proc. of Science, arXiv:170505332v1

Miyazaki, A., & Tsuboi, M., 2000, *ApJ* 536, 357

Mok, A., Wilson, C.D., Golding, J., et al., 2016, *MNRAS* 456, 4384

Morokuma-Matsui, K., Sorai, K., Watanabe Y., & Kuno, N., 2014, *PASJ* 67, 2

Moustakas, J., & Kennicutt, R.C., 2006, *ApJ* 651, 155

Moustakas, J., Kennicutt, R.C., & Tremonti, C.A., 2010, *ApJS* 190, 233

Mulder P.S., & van Driel W., 1993, *A&A* 272, 63

Mulder, P.S., van Driel W., & Braine J., 1995, *A&A* 300, 687

Muraoka, K., Sorai, K., Kuno, N., and 16 co-authors, 2016 *PASJ* 68, 9

Mundel, C.G., Pedlar, A., Axon, D.J., Meaburn, J., & Unger, S.W., 1995, *MNRAS* 277, 641

Nakai, N., & Kuno, N., 1995, *PASJ* 47, 761

Narayanan, D., Krumholz, M., Ostriker, E.C., & Hernquist, L., 2011, *MNRAS* 418, 664

Nishiyama, K, & Nakai, N., 2001, *PASJ* 53, 713

Ogle, P.M., Lanz, L., & Appleton, P.N., 2014 , *ApJL* 788, L33

Oka, T., Hasegawa, T., Hayashi, M., Handa, T., & Sakamoto, S., 1998, *ApJ* 493, 730

Oka, T., Onodera, Y., Nagai, M., Tanaka, K., Matsumura, S., & Kamegai, K., 2012, *ApJS* 201, 14

Olofsson, H., & Rydbeck, G., 1984, *A&A* 134, 36

Ondrechen, M.P., & van der Hulst, J.M., 1989a *ApJ* 342, 29

Ondrechen, M.P., van der Hulst J.M., & Hummel E., 1989b, *ApJ* 342, 39

Oosterloo, T., Oonk, J.B.R., Morganti, R., et al., 2017, *A&A* 608, A38

Ott, M., Whiteoak, J.B., Henkel, C., & Wielebinsky, R., 2001, *A&A* 372, 463

Paglione, T.A.D., Wall, W.F., Young, J.S., and 6 co-authors, 2001, *ApJS* 135, 183

Papadopoulos, P.P., & Seaquist, E.R., 1998, *ApJ* 492, 521 1995, *A&A* 300, 3698

Papadopoulos, P.P., & Seaquist, E.R., 1999, *ApJ* 516, 114

Papadopoulos, P.P., & Allen, M.A., 2000, *ApJ* 537, 631

Papadopoulos, P.P., Thi, W.F., & Viti, S., 2004, *MNRAS* 351, 147

Papadopoulos, P.P., van der Werf, P.P., Xilouris, E.M.,, Isaak, K.G., Gao, Y., & Mühle, S., 2012, *MNRAS* 426, 260

Peimbert, M., Peimbert, A., & Delgado-Inglada, G., 2017, *PASP* 129:082001

Petitpas, G.R., & Wilson, C.D., 2000, *ApJL* 538, L117

Petitpas, G.R., & Wilson, C.D., 2003, *ApJ* 587, 649

Pineda, J.L., Langer, W.D., Velusamy, T., & Goldsmith, P.F., 2013, *A&A* 554, A103

Pilyugin, L.S., Grebel, E.K., & Mansson, L., 2012, *MNRAS* 424, 231

Pilyugin, L.S., Grebel, E.K., & Kniazev, A.Y., 2014, *AJ* 147, 131

Puche, D., Carignan C., & van Gorkom J.H., 1991, *AJ* 101, 456

Rand R.J., 1994, *A&A* 285, 833

Rampazzo, R., Alexander, P., Carignan, C., et al., 2006, *MNRAS* 368, 851

Regan, M.W., & Vogel, S.N, 1995, *ApJ* 449, 576

Regan, M.W., Sheth, K., Vogel, S.N., 1999 *ApJ* 526, 97

Reuter, H.-P., Sievers, A.W., Pohl, M., Lesch, H./, & Wielebinski, R., 1996, *A&A* 306, 721

Remy, Q., Grenier, I.A., Marshall, D.J., & Casandjian. J.M., 2017, *A&A* 601, A78

Requena-Torres, M.A., Güsten, R., Weisz, A., et al., 2012, *A&A* 542, L21

Richmond, M.W., & Knapp, G.R., 1986, *AJ* 91, 517

Rickard L.J, Turner, B.E. & Palmer P, 1985 *AJ* 90, 1175

Rickard, L. J, & Blitz, L., 1985, *ApJL* 292, L57

Robertson, P., Shields, G.A., Davé, R., Blanc, G.A., & Wright, A., 2013, *ApJ* 773, 4

Röllig, M., Abel, N.P., Bel, T., and 21 co-authors, 2007, *A&A* 467, 187

Rosenberg, M.J.F., Kazandjian, M.V., van der Werf, P.P., et al., 2014a, *A&A* 564, A126

Rosenberg, M.J.F., Meijerink, R., Israel, F.P., van der Werf, P.P., Xilouris, E.M., & Weisz, A., 2014b, *A&A* 568, A90

Saikia, D.J., Unger, S.W., Pedlar, A. *et al.*, 1990, *MNRAS* 245, 397

Sage, L.J., 1993, *A&A Suppl* 100, 537

Sakamoto, K., Okumura, S., Minezaki, T., Kobayashi, Y., & Wada, K., 1995, *AJ* 110, 2075

Sakamoto, K., Okumura, S.K., Ishizuki, S., & Scoville, N.Z., 1999, *ApJS* 124, 403

Sakamoto, S., Handa, T., Sofue, Y., Honma, M., & Sorai, K., 1997, *ApJ* 475, 134

Sakamoto, K., Ho, P.T.P., & Peck, A.B., 2006, *ApJ* 644, 862

Sakamoto, K., Ho, P.T.P., Mao, R.-Q., Matsushita, S., & Peck, A.B., 2007, *ApJ* 654, 782

Sakamoto, K., Aalto, S., Combes, F., Evans, A., & Peck, A., 2014, *ApJ* 797, 90

Sanders, D.B..& Mirabel, I.F., 1985 *ApJL* 298, L31

Sanders, D.B., Scovile, N.Z., & Soifer, B.T., 1991, *ApJ* 370, 158

Sandqvist, Aa, Elfhag, T., & Jörsäter, S., 1988, *A&A* 201, 223

Sandqvist, Aa, Jörsäter, S., & Lindblad, P.O., 1995, *A&A* 295, 585

Sandquist, Aa, 1999, *A&A* 343, 367

Sandstrom, K.M., Leroy, A.K., Walter, F., et al., 2013, *ApJ* 777, 5

Sauty, S., Casoli, F., Boselli, A., et al., 2003, *A&A* 411, 381

Schilke, P., Carlstrom, J.E., Keene, J., & Phillips, T.G., 1993, *ApJL* 417, L67

Schulz, A., Henkel, C., Muders, D., Mao, R.Q., Röllig. M., Mauersberger, R., 2007 *A&A* 466, 467

Scoville, N.Z., Young, J.S., & Lucy, L.B., 1983, *ApJ* 270, 443

Seaquist, E.R., & Clark, J., 2001, *ApJ* 552, 133

Sempere, M.J., & García-Burillo, S., 1997, *A&A* 325, 769

Shetty, R., Glover, S.C., Dullemond, C.P., Ostriker, E.C., Harris, A.I., & Klessen, R.S., 2011, *MNRAS* 415, 3253

Shibatsuka, T., Matsushita, S., Kohno, K., & Kawabe, R., 2003, *PASJ* 55, 87

Shostak, G.S., & van der Kruit P.C., 1984 *A&A* 132, 20

Skillman, E.D., Kennicutt, R.C., Shields, G.A., & Zaritsky, D., 1996, *ApJ* 462, 147

Sliwa, K., Wilson, C.D., Krips, M., et al., 2013, *ApJ* 711, 126

Sliwa, K., Wilson, C.D., Iono, D., Peck, A., & Matsushita, S., 2014, *ApJL* 796, L15

Smith, P.A., Brand, P.W.J.L., Mountain, C.M., Puxley, P.J., & Nakai, N., 1991, *MNRAS* 252, 6P

Smith B.J., & Wallin J.F., 1992, *ApJ* 393, 544

Sodroski, T.J., Odegard, N., Dwek, E., et al., 1995, *ApJ* 452, 262

Sofue, Y., Doi, M., Krause, M., Nakai, N., & Handa, T., 1989, *PASJ* 41, 113

Sofue, Y., Wakamatsu, K., Taniguchi, Y., & Nakai, N., 1993a, *PASJ* 45, 43

Sofue, Y., & Nakai, N, 1993b, *PASJ* , 45, 139

Sofue, Y., Tomita, A., Honma, M, & Tutui, Y., 1999, *PASJ* 51, 737

Sofue, Y., Koda, J., Nakanishi, H. Onodera, S., Kohno, K., Tomita, A., & Okumura, S., 2003, *PASJ* 55, 17

Sofue, Y., Koda, J., Nakanishi, H., & Hidaka, M., 2003, *PASJ* , 55, 75

Solomon, P.M., Downes, D,. Radford, S.J.E., & Barrett, J.W., 1997, *ApJ* 478, 144

Sorai, K., Nakai, N., Kuno, N., Nishiyama, K, & Hasegawa, T., 2000, *PASJ* 52, 785

Stacey, G.J., Geis, N., Genzel R., et al., 1991, *ApJ* 373, 423

Stanford, S.A., & Wood D.O.S., 1989, *ApJ* 346, 712.90

Stanford, S.A., 1990, *ApJ* 358, 153

Stark, A.A., Knapp, G.R., Bally, J., Wilson, R.W., Penzias, A. A., & Rowe, H.E., 1986, *ApJ* 310, 660

Stark, A.A., Elmegreen, B.G., & Chance, D., 1987, *ApJ* 322, 64

Stutzki, j., Graf, U.U., Haas, S., and 10 co-authors, 1997, *ApJL* 477, L33

Swaters, R.A., Sancisi, R., & van der Hulst, J.M., 1997, *ApJ* 491, 140

Tacconi L.J., & Young J.S., 1986, *ApJ* 308, 600

Tacconi, L.J., Tacconi-Garman, L.E., Thornley, M., & van Woerden, H., 1991, *A&A* 252, 541

Tan, Q.H., Gao, Y., Zhang, Z.Y., Xia, X.Y., 2011, *RAA*, 11, 787

Tang, X.D., Henkel, C., Menten, K.M., and 16 co-authors, 2019, *A&A* 629, A6

Taramopoulos, A., Payne, H., & Briggs, F.H., 2001, *A&A* 365, 360

Tilanus R.P.J., & Allen R.J., 1991, *A&A* 244, 8

Tilanus R.P.J., & Allen R.J., 1993, *A&A* 274, 707

Tinney, C.G., Scoville, N.Z., Sanders, D.B., & Soifer, B.T., 1990, *ApJ* 362, 473

Tunnard R., Greve, T.R., García-Burillo, J., et al., 2015, *ApJ* 815, 114

van Albada, G.D., 1980, *A&A* 90, 128

van Dishoeck, E.F., & Black, J.H., 1988, *ApJ* 334, 771

van Driel, W., & van den Broek, A.C., 1991, *A&A* 251, 431

van Driel, W., Combes F., Casoli F., and 16 co-authors, 1995, *AJ* 109, 942.

van der Hulst, J.M., 1979, *A&A* 71, 131

van der Kruit, P.C., & Freeman, K.C., 2011, *ARAA* 49, 301

van der Tak, F.F.S., Black, J.H., Schöier, F.L., Jansen, D.J., van Dishoeck, E.F. 2007, A&A 468, 627

van Moorsel, G.A. 1983, *A&A Suppl* 54, 1

Verheijen, M.A.W., & Sancisi, R., 2001, *A&A* 370, 756

Vila-Costas, M.B., & Edmunds, M.G., 1992, *MNRAS* 239, 121

Vila-Vilaro, B., Cepa, J., & Zabludoff, A., 2015, *ApJS* 218, 28

Visser, R., van Dishoeck, E.F., & Black, J.H., 2009, *A&A* 503, 323

Wada, K., & Tomisaka, K., 2005, *ApJ* 619, 93

Walter, F., Dahlem, M., & Lisenfeld, U., 2004, *ApJ* 606, 258

Warmels, R.H., 1988, *A&A Suppl* 72, 57

Weisz, A., Neininger, N., Hüttemeister, S., & Klein, U., 2001, *A&A* 365, 571

Weliachew, L., Casoli, F., & Combes, F., 1988 *A&A* 199, 29

Wevers, B.M.H.R., van der Kruit P.C., & Allen R.J., 1986, *A&A Suppl* 66, 505

Whiteoak, J.B., Dahlem, M., Wielebinski, R., & Harnett, J.I., 1990, *A&A* 231, 25

Wilding, T., Alexander P, & Green D.A., 1993, *MNRAS* 263, 1075.

Wilson, C.D., Scoville, N., Madden S.C., Charmandarias, V., 2000, *ApJ* 542, 120

Wilson, C.D., Warren, B.E., Israel, F.P., et al., 2012, *MNRAS* 424, 3050

Wong, T., & Blitz, L., 2000, *ApJ* 540, 771

Yamashita, T., Komugi, S., Matsuhara, H., and 7 co-authors, 2017, *ApJ* 844, 96

Yao, L., Seaquist, E.R., Kuno, N., & Dunne, L., 2001, *ApJ* 588, 771

Young, J.S., & Scoville, N.Z., 1984, *ApJ* 287, 153

Young, Y.S., & Sanders, D.B., 1986, *ApJ* 302, 680

Young, J.S., Clausen, M.J., & Scoville, N.Z., 1988, *ApJ* 324, 115

Young, J.S., Xie, S., Tacconi, L., and 16 co-authors, 1995, *ApJS* 98, 219

Yun, M.S., Ho P.T.P., & Lo K.Y., 1993, *ApJL* 411, L17

Yun, M.S., & Hibbard, J.E., 2001 *ApJ* 550 104

Zaritsky, D., Kennicutt, R.C., & Huchra, J.P., 1994, *ApJ* 420, 87

Zhang, X., Wright M., & Alexander P., 1993, *ApJ* 418, 100

Zhang, Z-Y., Henkel, C., Gao, Y, et al., 2014, *A&A* 568, A122

Zhu, M., Seauquist, E.R., & Kuno, N., 2003, *ApJ* 588, 243

Appendix A: CO survey results and literature data

Appendix A.1: J=1-0 fluxes versus observing beam size

Table A.1 collects J=1-0 ^{12}CO data from this paper and from the literature as a function of observing beam size. Column 2 identifies the telescope used. The beam size is listed in Col. 3; 'total' indicates the extrapolated line flux of the whole galaxy taken from the reference cited. Column 4 gives the line flux in units of Jy km s^{-1}. The factors required to convert flux density into temperature are given in a footnote. In all cases where two or more fluxes (including the new measurements from this paper) are available at the same resolution, their average (marked 'ave') is also given in Col. 4. In Col. 5 we list the ratio of our new value to this average. The IRAM fluxes presented in this paper are extracted from profiles with generally better S/Ns and better baselines than those taken from the literature. For the same galaxy and the same aperture, fluxes given in the literature can differ by as much as a factor of two. Given this spread, we did not attempt to identify discrepant fluxes **or to eliminate** them from the compilation.

The average ratios of the fluxes for beam sizes of 45" and 22" measured by us to those collected from the literature are given in Table A.3. They are close to unity and have modest standard deviations. This shows that the results of the present survey and those of previous work are consistent. The data in Table A.1 have been used to construct Fig. 7.

Appendix A.2: Comparison CO(2-1) and CO(3-2) survey results

The literature provides far fewer data for the J=2-1 and J=3-2 CO transitions. Braine *et al.* (1993a) used the IRAM telescope with early receivers and backends to measure a large number of galaxies in the J=2-1 transition, of which 17 are in common with our survey. They convolved small maps to match the J=2-1 intensities to the J=1-0 beam. These are compared to the JCMT J=2-1 measurements in Table A.2. Our results are somewhat higher on average, but the dispersion (standard deviation) is significant. The other large extragalactic IRAM J=2-1 survey by Albrecht *et al.* (2007) unfortunately has few objects in common with our survey, as is the case for the JCMT J=3-2 survey by Yao *et al.* (2003). Of more interest are the J=3-2 CO surveys conducted with the 10m Heinrich Hertz Submillimeter Telescope (HHSMT) with a beam size of 22" (Mauersberger *et al.* 1999; Dumke *et al.* 2001; Mao *et al.* 2010), which have several galaxies in common with our survey. Data from the latter two surveys are also summarized in Table A.2 together with JCMT intensities from maps convolved to 22". We disregarded the Mauersberger *et al.* (1999) results because they are superseded by the Mao *et al.* (2010) survey and suffer from serious calibration and pointing issues. To a lesser extent, these also plague the later two surveys, as inspection of Cols. 6 and 7 shows. This issue is discussed in more detail by Mao *et al.* (2010). It is therefore not surprising that the ratios of the HHSMT to the JCMT intensities vary either way by factors of up to 2.5. Notwithstanding the relatively large dispersions, the average intensities are quite consistent.

Appendix B: Observed and literature isotopologue ratios

Large-scale extragalactic ^{13}CO hence ^{12}CO/^{13}CO isotopologue surveys are lacking in all J transitions. There are, however, a

Table A.1. J=1-0 fluxes in different beams

NGC (1)	Tel^{a} (2)	Beam (” (3)	Flux^{b} Jy km s^{-1} (4)	 (5)	Ref (6)
134	SEST	45	432		18
	SEST	45	297		20
	SEST	45	323		TP
	ave	45	351±41	(0.92)	
253	BTL	total	44000		9
	FCRAO	total	21060		15
	ave	total	32530±11470		
	FCRAO	45	10790		15
	FCRAO	45	6767		61
	SEST	45	7130		64
	SEST	45	6067		TP
	ave	45	7689±1057	(0.79)	
	IRAM	22	5295		61
	IRAM	22	4289		63
	IRAM	22	4841		TP
	ave	22	4808±291	(1.01)	
	NOB	16	595		11
	NOB	16	756		62
	ave	16	675±81		
278	FCRAO	total	480		15
	FCRAO	45	328		15
	OSO	33	101		18
	IRAM	22	85		23
	IRAM	22	96		TP
	ave	22	91±6	(0.93)	
	NOB	16	43		11
	NOB	16	36		13
520	FCRAO	total	1260		15
	NRAO	total	1260		1
	ave	total	1260±0		
	FCRAO	45	903		5
	FCRAO	45	696		15
	SEST	45	531		TP
	ave	45	710±108	(0.75)	
	OSO	33	344		20
	IRAM	22	211		24
	IRAM	22	278		TP
	ave	22	245±34	(1.14)	
	NOB	16	94		11
613	SEST	45	661		18
	SEST	45	448		25
	SEST	45	473		TP
	ave	45	527±67	(0.90)	
	IRAM	22	328		TP
628	NRAO	total	2611		2
	FCRAO	total	2160		15
	ave	total	2386±226		
	NRAO	55	198		2
	NRAO	55	207		3
	ave	55	203±5		
	FCRAO	45	96		15
	IRAM	22	31		TP
	IRAM	22	19		23
	ave	22	25±6	(0.76)	
	NOB	16	10		11
	NOB	16	15		13
	ave	16	13±3		
	BIMA	6.2	10		58
660	FCRAO	total	2840		15
	BTL	total	2800		9
	ave	total	2820±20		
	NRAO	55	497		4
	FCRAO	45	1793		5
	FCRAO	45	884		15

Table A.1. continued

NGC (1)	Tel (2)	Beam (” (3)	Flux Jy km s^{-1} (4)	(5)	Ref (6)
660	SEST	45	730		TP
	ave	45	1136±332	(0.64)	
	OSO	33	1271		20
	IRAM	22	724		TP
	IRAM	22	465		23
	ave	22	595±130	(1.22)	
695	FCRAO	total	220		15
	NRAO	55	210		7
	FCRAO	45	200		15
891	BTL	total	13000		9
	NRAO	total	7105		2
	FCRAO	total	4570		15
	ave	total	8225±2497		
	NRAO	55	1355		2
	FCRAO	45	607		15
	0SO	33	542		18
	IRAM	22	644		TP
	IRAM	22	451		23
	ave	22	548±97	(1.18)	
908	FCRAO	total	1330		15
	FCRAO	45	436		15
	SEST	45	234		18
	SEST	45	452		TP
	IRAM	22	140		TP
	NOB	16	22		11
	ave	45	374±70	(1.21)	
972	FCRAO	total	690		15
	FCRAO	45	406		15
	IRAM	22	314		TP
1055	FCRAO	total	2800		15
	FCRAO	45	947		15
	SEST	45	544		TP
	ave	45	746±202	(0.73)	
	OSO	33	260		18
	IRAM	23	361		TP
	IRAM	23	216		23
	ave	23	289±73	(1.25)	
1068	BTL	total	19000		9
	FCRAO	total	21060		15
	ave	total	20030±1030		
	NRAO	55	2555		6
	NRAO	55	2520		21
	FCRAO	45	2306		15
	IRAM	22	790		TP
	IRAM	22	1025		23
	ave	22	908±118	(0.87)	
	NOB	16	229		66
	BIMA	7.1	245		58
	BIMA	3.9	80		65
1084	FCRAO	total	920		15
	FCRAO	45	266		15
	SEST	45	220		18
	SEST	45	374		TP
	ave	45	287±46	(1.30)	
	IRAM	22	143		TP
	IRAM	22	146		23
	ave	23	145±2	(0.99)	
1097	BTL	total	5400		9
	FCRAO	45	158		15
	SEST	45	920		TP
	IRAM	22	639		TP
1365	NRAO	55	1680		6
	NRAO	55	1700		21
	NRAO	55	1670		69

Table A.1. continued

NGC (1)	Tel (2)	Beam (” (3)	Flux Jy km s^{-1} (4)	(5)	Ref (6)
1365	ave	55	1683±9		
	SEST	45	2035		18
	SEST	45	2117		68
	SEST	45	1928		TP
	ave	45	2026±55	(0.95)	
	IRAM	22	1222		TP
1433	SEST	45	321		25
	SEST	45	276		TP
	ave	45	299±22	(0.92)	
1482	FCRAO	total	560		15
	NRAO	55	284		7
	FCRAO	45	462		15
	SEST	45	645		18
	SEST	45	443		19
	SEST	45	442		22
	SEST	45	293		TP
	ave	45	460±102	(0.64)	
	IRAM	22	151		22
	NOB	16	89		11
1614	FCRAO	total	290		15
	NRAO	55	301		7
	FCRAO	45	242		15
	SEST	45	163		17
	SEST	45	291		18
	SEST	45	227		20
	SEST	45	270		TP
	ave	45	239±22	(1.13)	
	IRAM	22	203		TP
	IRAM	22	61		17
	IRAM	22	212		80
	ave	22	159±49	(1.28)	
1667	NRAO	55	130		7
	NRAO	55	280		6
	NRAO	55	244		21
	ave	55	218±45		
1672	SEST	45	855		25
	SEST	45	444		TP
	ave	45	650±205	(0.68)	
1808	SEST	45	1512		20
	SEST	45	1604		26
	SEST	45	1739		TP
	ave	45	1618±66	(1.07)	
	IRAM	22	635		TP
2146	FCRAO	total	2840		15
	FCRAO	45	1579		15
	OSO	33	824		18
	OSO	33	1042		20
	ave	33	933±109		
	IRAM	22	879		TP
	IRAM	22	555		23
	ave	22	717±162	(1.23)	
2273	FCRAO	total	160		15
	FCRAO	45	137		15
	NRAO	45	105		21
	ave	45	121±16		
	IRAM	22	78		TP
2369	SEST	45	674		18
	SEST	45	702		20
	SEST	45	493		TP
	ave	45	623±80	(0.79)	
2397	SEST	45	276		19
	SEST	45	269		22
	SEST	45	314		TP
	ave	45	286±17	(1.10)	

Table A.1. continued

NGC (1)	Tel (2)	Beam (” (3)	Flux $Jy\,\mathrm{km\,s^{-1}}$ (4)	(5)	Ref (6)
2559	FCRAO	total	1100		15
	FCRAO	45	743		15
	SEST	45	626		18
	SEST	45	607		TP
	ave	45	659±43	(0.92)	
	IRAM	22	369		TP
2623	FCRAO	total	170		15
	NRAO	55	170		1
	NRAO	55	170		5
	NRAO	55	168		7
	ave	55	169±1		
	FCRAO	45	202		5
	FCRAO	45	161		15
	ave	45	182±21		
	IRAM	22	86		TP
	NOB	16	96		81
2798	FCRAO	total	440		15
	FCRAO	45	246		15
	OSO	33	75		18
	NOB	16	27		14
2903	BTL	total	4900		9
	NRAO	total	2783		2
	FCRAO	total	2740		15
	ave	total	3474±712		
	PMO	55	783		82
	NRAO	55	770		2
	ave	55	777±7		
	FCRAO	45	553		15
	IRAM	22	375		TP
	NOB	16	285		13
	BIMA	6	129		58
2992	NRAO	55	116		5
	NRAO	55	154		21
	ave	55	135±19		
	SEST	45	155		TP
	NOB	16	25		13
3034	FCRAO	total	18240		15
	PMO	55	7070		82
	FCRAO	45	6670		15
	OSO	33	3116		71
	IRAM	22	3007		70
	IRAM	22	3196		TP
	ave	22	3102±95	(1.03)	
	NOB	16	1001		11
3079	FCRAO	total	2280		15
	NRAO	55	1509		21
	NRAO	55	1684		76
	ave	55	1597±88		
	FCRAO	45	1602		15
	SEST	45	845		20
	ave	45	1224±379		
	OSO	33	870		18
	IRAM	22	996		23
	IRAM	22	1019		73
	IRAM	22	1105		TP
	IRAM	22	1153		80
	ave	23	1068±37	(1.03)	
	OVRO	7	362		75
	NMA	1.7	125		74
3175	SEST	45	371		18
	SEST	45	357		TP
	ave	45	364±7	(0.98)	
	IRAM	22	201		TP
3227	BTL	total	960		9

Table A.1. continued

NGC (1)	Tel (2)	Beam (” (3)	Flux $Jy\,\mathrm{km\,s^{-1}}$ (4)	(5)	Ref (6)
3227	NRAO	55	450		1
	NRAO	55	432		21
	IRAM	22	254		23
	IRAM	22	290		TP
	ave	22	272±18	(1.07)	
	NOB	16	18		14
3256	SEST	45	1539		20
	SEST	45	1305		27
	SEST	45	1297		TP
	ave	45	1380±79	(0.94)	
3281	NRAO	55	<84		6
	NRAO	55	<58		21
	SEST	45	26		TP
3310	FCRAO	total	140		15
	NRAO	55	85		76
	FCRAO	45	50		15
	IRAM	22	17		23
	IRAM	22	37		TP
	ave	22	27±10	(1.37)	
	NOB	16	22		14
3351	FCRAO	total	700		15
	FCRAO	45	338		15
	OSO	33	233		18
	IRAM	22	80		23
	BIMA	6.3	31		58
3504	BTL	total	1500		9
	FCRAO	total	410		15
	ave	total	807±426		
	NRAO	55	511		4
	NRAO	55	193		5
	ave	55	352±159		
	FCRAO	45	317		15
	SEST	45	390		22
	ave	45	365±30		
	IRAM	22	265		TP
	NOB	16	247		11
3556	FCRAO	total	850		15
	FCRAO	45	330		15
	OSO	33	149		18
	IRAM	22	253		TP
	NOB	16	38		11
3593	FCRAO	total	910		15
	NRAO	total	634		2
	ave	total	772±138		
	NRAO	55	567		2
	FCRAO	45	431		15
	SEST	45	463		TP
	ave	45	447±16	(1.04)	
	OSO	33	267		18
	IRAM	22	297		TP
	NOB	16	113		11
3620	SEST	45	902		18
	SEST	45	894		TP
	ave	45	898±4	(1.000	
3627	BTL	total	8300		9
	FCRAO	total	4660		15
	ave	total	6480±1820		
	PMO	55	542		82
	NRAO	55	1150		29
	FCRAO	45	786		15
	SEST	45	516		TP
	PDBI	42	668		29
	ave	45	657±78	(0.79)	
	PDBI	22	359		29

Table A.1. continued

NGC (1)	Tel (2)	Beam (” (3)	Flux $Jy\,\mathrm{km\,s^{-1}}$ (4)	 (5)	Ref (6)
3627	IRAM	22	343		29
	IRAM	22	423		23
	IRAM	22	378		30
	IRAM	22	350		TP
	ave	22	370±14	(0.95)	
	NOB	16	168		28
	BIMA	6.5	129		58
3628	BTL	total	10000		9
	FCRAO	total	3800		15
	ave	total	5867±2530		
	PMO	55	1130		82
	NRAO	55	935		4
	ave	55	1033±98		
	FCRAO	45	1604		15
	SEST	45	1416		TP
	ave	45	1510±94	(0.94)	
	IRAM	22	954		TP
	IRAM	22	611		23
	ave	22	783±171	(1.22)	
3690	FCRAO	total	610		15
	NRAO	55	610		1
	NRAO	55	140		5
	FCRAO	45	449		15
	IRAM	22	264		24
	IRAM	22	323		TP
	ave	22	294±29	(1.10)	
	NOB	16	29		11
4030	FCRAO	total	1050		15
	FCRAO	45	271		15
	SEST	45	437		TP
	ave	45	354±83	(1.23)	
	IRAM	22	198		TP
4038	FCRAO	total	1150		15
	NRAO	55	557		5
	FCRAO	45	676		15
	SEST	45	567		20
	ave	45	622±55		
	IRAM	22	220		TP
	NOB	16	67		11
	OVRO	3.9	91		31
4039	FCRAO	total	920		15
	FCRAO	45	685		15
	SEST	45	594		20
	ave	45	640±46		
	IRAM	22	214		TP
	NOB	16	173		11
	OVRO	3.9	32		31
4051	BTL	total	790		9
	FCRAO	total	740		15
	ave	total	765±25		
	NRAO	55	259		21
	FCRAO	45	218		15
	IRAM	22	178		TP
	BIMA	5.9	39		58
4102	FCRAO	total	660		15
	NRAO	55	350		5
	FCRAO	45	404		15
	OSO	33	339		18
	IRAM	22	351		TP
	NOB	16	277		13
4254	BTL	total	2611		8
	FCRAO	total	3000		16
	FCRAO	total	2830		10
	ave	total	2814±113		

Table A.1. continued

NGC (1)	Tel (2)	Beam (” (3)	Flux $Jy\,\mathrm{km\,s^{-1}}$ (4)	 (5)	Ref (6)
4254	BTL	100	1547		8
	FCRAO	45	445		16
	SEST	45	758		TP
	ave	45	602±157	(1.26)	
	IRAM	22	201		TP
	NOB	16	113		11
	NMA	4.2	17		31
	NMA	2.6	8		12
4258	FCRAO	total	1240		15
	NRAO	55	906		3
	FCRAO	45	301		15
	SEST	45	356		TP
	ave	45	329±28	(1.08)	
	IRAM	22	320		33
	NOB	16	221		34
	BIMA	5.7	103		58
	PDBI	3.9	50		32
4293	FCRAO	total	279		16
	FCRAO	45	265		16
	IRAM	22	169		TP
	NOB	16	161		11
4303	BTL	total	1332		8
	FCRAO	total	2280		16
	FCRAO	total	1920		10
	ave	total	1844±339		
	BTL	100	1148		8
	NRAO	55	238		4
	NRAO	55	588		76
	NMA	45	494		36
	FCRAO	45	500		16
	ave	45	497±3		
	IRAM	22	259		TP
	NOB	16	166		11
	NMA	13	193		35
	BIMA	6.4	65		58
	NMA	2.3	25		12
4321	BTL	total	4412		8
	FCRAO	total	3340		16
	FCRAO	total	2390		10
	ave	total	3381±584		
	BTL	100	1423		8
	FCRAO	45	630		16
	SEST	45	448		TP
	ave	45	539±9	(0.83)	
	IRAM	22	392		TP
	IRAM	22	367		23
	IRAM	22	384		36
	ave	22	381±7	(1.03)	
	NOB	16	151		11
	NOB	16	88		39
	ave	16	120±32		
	BIMA	5.9	48		58
	ALMA	3.5	41		44
	NMA	2.5	27		38
	PDBI	1.6	11		37
4385	FCRAO	total	70		15
	FCRAO	45	54		15
4388	BTL	total	992		8
	FCRAO	total	230		16
	ave	total	611±381		
	BTL	100	227		8
	NRAO	55	233		21
	FCRAO	45	113		16
	SEST	45	163		TP

Table A.1. continued

NGC (1)	Tel (2)	Beam (" (3)	Flux $Jy\,\mathrm{km\,s^{-1}}$ (4)	(5)	Ref (6)
4388	ave	45	138±25	(1.18)	
4414	FCRAO	total	2740		15
	NRAO	total	1498		2
	ave	total	2119±621		
	NRAO	55	973		2
	FCRAO	45	729		15
	OSO	33	271		18
	IRAM	22	242		TP
	IRAM	22	268		23
	IRAM	22	249		40
	ave	22	253±10	(0.96)	
	NOB	16	190		11
4457	FCRAO	total	490		15
	FCRAO	45	197		15
	IRAM	22	139		TP
4527	BTL	total	2794		8
	FCRAO	total	1800		15
	ave	total	2247±447		
	BTL	100	2008		8
	FCRAO	45	1260		10
	FCRAO	45	662		15
	SEST	45	656		TP
	ave	45	859±200	(0.76)	
	IRAM	22	414		TP
	NOB	16	62		11
	NMA	7.3	112		43
	NMA	4.6	95		42
	NMA	3.0	47		42
4536	FCRAO	total	740		16
	NRAO	55	368		5
	FCRAO	45	390		10
	FCRAO	45	424		16
	SEST	45	280		TP
	ave	45	365±53	(0.77)	
	OSO	33	288		18
	IRAM	22	290		TP
	NOB	16	290		11
	NMA	2.1	28		12
4565	BTL	100	545		47
	OSO	33	138		18
	IRAM	22	56		23
	NOB	16	35		46
4593	NRAO	55	<175		6
	NRAO	55	86		21
	SEST	45	32		TP
	IRAM	22	35		TP
4631	BTL	total	5200		9
	FCRAO	total	1740		15
	PMO	55	546		82
	NRAO	55	329		4
	FCRAO	45	549		15
	IRAM	22	227		19
	IRAM	22	206		TP
	ave	22	217±10	(0.95)	
4647	BTL	total	2872		8
	FCRAO	total	600		16
	ave	total	1736±1136		
	BTL	100	712		8
	FCRAO	45	210		16
	NOB	16	62		11
4666	SEST	total	2780		48
	FCRAO	total	2130		15
	ave	total	2455±325		
	FCRAO	45	696		15

Table A.1. continued

NGC (1)	Tel (2)	Beam (" (3)	Flux $Jy\,\mathrm{km\,s^{-1}}$ (4)	(5)	Ref (6)
4666	SEST	45	580		TP
	ave	45	638±58	(0.91)	
	IRAM	23	346		TP
	NOB	16	113		11
	OVRO	3.8	218		48
4736	BTL	total	3280		9
	FCRAO	total	2560		15
	ave	total	2920±360		
	BTL	100	938		9
	PMO	55	252		82
	FCRAO	45	405		15
	IRAM	22	198		TP
	IRAM	22	197		49
	ave	22	198±1	(1.00)	
	NOB	16	146		11
	BIMA	5.9	45		50
4826	BTL	total	2600		9
	FCRAO	total	2170		15
	ave	total	2385±215		
	NRAO	55	403		4
	FCRAO	45	1033		15
	ave	45	718±315		
	OSO	33	456		20
	IRAM	22	425		TP
	IRAM	22	493		52
	ave	22	459±34	(0.93)	
	NOB	16	336		11
	BIMA	6.2	103		58
	PDBI	2.6	34		51
5033	FCRAO	total	1640		15
	NRAO	55	403		6
	NRAO	55	620		21
	ave	55	512±109		
	FCRAO	45	302		15
	OSO	33	291		18
	OSO	33	248		20
	ave	33	270±22		
	IRAM	22	248		TP
	IRAM	22	99		23
	ave	22	174±74	(1.42)	
	NOB	16	142		11
	BIMA	5.7	41		58
	NMA	3.8	27		53
5055	NRAO	total	5719		2
	FCRAO	total	5670		15
	ave	total	5695±25		
	PMO	55	508		82
	NRAO	55	648		2
	NRAO	55	1184		3
	ave	55	780±206		
	FCRAO	45	697		15
	OSO	33	382		18
	OSO	33	403		20
	ave	33	393±10		
	IRAM	22	331		TP
	NOB	16	168		54
	BIMA	5.7	51		58
5135	NRAO	55	375		6
	NRAO	55	389		7
	NRAO	55	442		21
	ave	55	402±20		
	SEST	45	340		TP
	IRAM	22	291		TP

Table A.1. continued

NGC	Tel	Beam (”	Flux Jy km s^{-1}		Ref
(1)	(2)	(3)	(4)	(5)	(6)
5194	BTL	total	16000		9
	FCRAO	total	9210		15
	ave	total	12605±3395		
	PMO	55	1050		82
	FCRAO	45	1234		15
	IRAM	22	224		TP
5236	BTL	total	26000		9
	FCRAO	total	16320		15
	ave	total	21160±4840		
	NRAO	55	1197		5
	FCRAO	45	2050		15
	SEST	45	2400		79
	SEST	45	1486		TP
	ave	45	1979±266	(0.75)	
	IRAM	22	917		TP
	NOB	16	86		11
5713	FCRAO	total	680		15
	NRAO	55	1043		76
	FCRAO	45	254		15
	SEST	45	318		TP
	ave	45	286±32	(1.11)	
	IRAM	23	213		TP
	NOB	16	77		11
5775	FCRAO	total	630		15
	NRAO	55	382		76
	FCRAO	45	314		15
	IRAM	22	225		TP
6000	FCRAO	total	1000		15
	NRAO	45	904		15
	SEST	45	392		18
	SEST	45	406		19
	SEST	45	407		22
	SEST	45	425		TP
	ave	45	507±110	(0.84)	
	IRAM	22	361		TP
	NOB	16	67		11
6090	FCRAO	total	200		15
	NRAO	55	151		7
	FCRAO	45	145		15
6215	SEST	45	192		19
	SEST	45	216		20
	SEST	45	192		22
	SEST	45	206		TP
	ave	45	202±6	(1.02)	
6221	SEST	45	589		20
	SEST	45	582		TP
	ave	45	586±4	(0.99)	
6240	FCRAO	total	300		15
	NRAO	55	315		7
	FCRAO	45	378		5
	FCRAO	45	239		15
	SEST	45	331		TP
	ave	45	316±40	(1.05)	
	IRAM	22	330		TP
	IRAM	22	277		24
	IRAM	22	345		80
	ave	22	317±21	(1.04)	
6764	NRAO	55	249		5
	OSO	33	86		18
	IRAM	22	142		TP
	IRAM	22	110		55
	ave	22	126±16	(1.13)	
6810	SEST	45	556		TP
	OSO	33	162		18

Table A.1. continued

NGC	Tel	Beam (”	Flux Jy km s^{-1}		Ref
(1)	(2)	(3)	(4)	(5)	(6)
6810	OSO	33	403		20
	ave	33	283±120		
6946	BTL	All	23000		9
	FCRAO	All	12370		15
	ave	All	17685±5315		
	NRAO	55	1540		77
	FCRAO	45	1842		15
	IRAM	22	1072		TP
	NOB	16	946		11
	BIMA	5.4	245		58
	BIMA	4.0	160		78
6951	BTL	total	1910		9
	FCRAO	total	1440		15
	ave	total	1675±235		
	FCRAO	45	350		15
	OSO	33	217		18
	OSO	33	202		20
	ave	33	210±8		
	IRAM	22	236		TP
	NOB	16	187		11
	NMA	3.5	49		56
7331	BTL	total	5600		9
	FCRAO	total	4160		15
	ave	total	4880±720		
	FCRAO	45	161		15
	OSO	33	250		18
	IRAM	22	179		23
	NOB	16	46		11
7469	FCRAO	total	240		15
	NRAO	55	420		6
	NRAO	55	336		7
	NRAO	55	338		21
	ave	55	374±25		
	FCRAO	45	238		15
	FCRAO	45	403		5
	SEST	45	202		TP
	ave	45	281±62	(0.72)	
	OSO	33	157		18
	IRAM	22	257		TP
	IRAM	22	296		80
	ave	22	277±20	(0.93)	
	NOB	16	27		14
7541	FCRAO	total	650		15
	NRAO	55	389		76
	FCRAO	45	341		15
	SEST	45	401		TP
	ave	45	371±30	(1.08)	
	OSO	33	626		18
	IRAM	22	134		TP
	NOB	16	118		11
7552	SEST	45	756		20
	SEST	45	792		57
	SEST	45	733		TP
	ave	45	760±17	(0.96)	
7582	SEST	45	567		20
	SEST	45	750		57
	SEST	45	614		TP
	ave	45	702±52	(0.87)	
7590	SEST	45	137		19
	SEST	45	138		22
	SEST	45	146		TP
	ave	45	140±3	(1.04)	
7674	FCRAO	total	350		15
	NRAO	55	140		7

Table A.1. continued

NGC (1)	Tel (2)	Beam (” (3)	Flux $Jy\,\mathrm{km\,s^{-1}}$ (4)	 (5)	Ref (6)
7674	FCRAO	45	168		5
	FCRAO	45	275		15
	ave	45	222±54		
7714	FCRAO	total	130		15
	NRAO	55	130		1
	NRAO	55	196		7
	ave	55	168±38		
	FCRAO	45	100		15
	SEST	45	42		17
	SEST	45	19		TP
	ave	45	54±24	(0.35)	
	IRAM	22	16		TP
	IRAM	22	58		17
	ave	22	37±20	(0.43)	
	NOB	16	7		14
7771	FCRAO	total	540		15
	NRAO	55	420		7
	FCRAO	45	381		15
	OSO	33	290		18
	IRAM	22	469		TP
	IRAM	22	462		24
	IRAM	22	489		80
	ave	22	473±8	(0.99)	
	NOB	16	323		81
I342	BTL	total	100000		9
	FCRAO	total	29220		15
	ave	total	64610±35390		
	FCRAO	45	1512		15
	NOB	16	478		11
	BIMA	5.3	97		57
Maf2	FCRAO	45	164		59
	IRAM	22	568		60

Notes:

[a] BTL: Bell Telephone Labs; SEST: Swedish-ESO Submillimeter Telescope; OSO: Onsala Space Observatory; IRAM: Institut Radio Astronomie Millimétrique - Pico Veleta); NOB: Nobeyama; FCRAO: Five Colleges Radio Observatory; NRAO: National Radio Astronomy Observatory; PMO: Purple Mountain Observatory; CSO: Caltech Submillimeter Observatory; SMA: Smithsonian Millimeter Array; OVRO: Owens Valley Radio Observatory; BIMA: Berkeley Illinois Maryland Array.

[b] Conversion factors S_{115GHz} –> T (see Papadopoulos *et al.* 2012): SEST S/T_A^*=27 Jy/K; OSO S/T_A^*=31 Jy/K; IRAM: S/T_A^*=6.3 Jy/K; NRAO/ARO: S/T_R^*=35 Jy/K; FCRAO/PMO: S/T_A^*=42 Jy/K; NOB: S/T_{mb}^*=2.4 Jy/K;

Table A.1. continued

references to Table A.1 1. Bushouse *et al.* 1999; 2. Sage, 1993; Adler & Liszt, 1989; Rickard, Turner, & Palmer, 1985; 5. Sanders & Mirabel, 1985; 6. Heckman *et al.* 1989; 7. Sanders, Scovile, & Soifer, 1991; 8. Stark *et al.* 1986; 9. Stark, Elmegreen, & Chance, 1987; 10. Chung *et al.* 2009; 11. Komugi *et al.* 2008; 12. Sofue *et al.* 2003a; 14. Sofue *et al.* 1994; 15. Young *et al.* 1995; 16. Kenney & Young, 1988; 17. Chini *et al.* 1992; 18. Elfhag *et al.* 1996; Chini, Krügel, & Lemke, 1996; 20. Aalto *et al.* 1995; 21. Maiolin *et al.* 1997; 22. Albrecht, Krügel, & Chini, 2007; 23. Braine *et al.* 1993a; 24. Solomon, Downes, & Radford, 1992; 25. Bajaja *et al.*, 1995; 26. Dahlem, *et al.* 1990; 27. Becker, & Freudling, 1991; 28. Morukama-Matsui *et al.* 2014; 29. Casasola *et al.* 2011; 30. Reuter *et al.* 1996; 31. Sofue *et al.* 2003b; 32. Krause *et al.* 2007; 33. Cox & Downes, 1996; 34. Sofue *et al.* 1989; 35. Koda & Sofue, 2006; 36. Sempere & García-Burillo, 1997; 37. García-Burillo *et al.* 1998; 38. Sakamoto *et al.* 1995; 39. Knapen *et al.* 1993; 40. Braine, Combes, & van Driel 1993; 41. Kawara *et al.* 1990; 42. Shibatsuka *et al.* 2003; 43. Sofue *et al.* 1993; 44. Vlahakis *et al.* 2013; Golla & Wielebinsky, 1994; 46. Sofue, & Nakai, 1992; 47. Richmond & Knapp, 1985; 48. Walter, Dahlem, & Lisenfeld, 2004; 49. Gerin, Casoli, & Combes, 1991; 50. Wong & Blitz, 2000; 51. Garciá-Burillo *et al.* 2003; 52. Casoli, & Gerin, 1993; 53. Kohno *et al.* 2003 54. Kuno *et al.* 1997; 55. Eckart *et al.* 1991; 56. Kohno, Kawabe, & Vila-Vilaró, 1999; 57. Claussen & Sahai, 1992; 58. Helfer *et al.* 2003; 59. Mason, & Wilson, 2004; 60. Weliachew, Casoli, & Combes, 1988; 61. Bayet *et al.* 2004; 62. Sorai *et al.* 2000; 63. Harrison, Henkel, & Russell, 1999; 64. Houghton *et al.* 1996; 65. Helfer & Blitz, 1995; 66. Kaneko *et al.* 1989 67. Scovile, Young, & Lucy, 1983; 68. Sandqvist, Jörsäter, & Lindblad, 1995; 69. Sandqvist, Elfhag, & Jörsäter, 1988; 70. Mao *et al.* 1988; 71. Olofson, & Rydbeck, 1984; 72. Young & Scoville, 1985; 73. Braine *et al.* 1997; 74. Koda *et al.* 2002; 75. Young, Clausen, & Scoville, 1988; 76. Tinney *et al.* 1990; 77. Crosthwaite & Turner, 2007; 78. Regan & Vogel, 1995; 79. Lundgren *et al.* 2004; 80. Costagliola *et al.* 2011; 81. Yamashita *et al.* 2017; 82. Tan *et al.* 2011.

significant number of J=1-0 ^{13}CO small-scale surveys and individual measurements from which isotopologue ratios can be constructed. In Table B.1 we collect these ratios for the J=1-0 transition as could be found in the literature for the galaxies in the present sample. For Cols. 3 through 10, we determined the ratio of each value to the corresponding value in Col. 2 (i.e., the ratio determined by the measurements in this paper). At the bottom of the table we present for each column the average of these ratios as well as its standard deviation. In all columns the average is close to unity, implying that for resolutions between 22” and 55”, the isotopologue ratio in the J=1-0 transition does not vary significantly with beam width. In Table B.2 we summarize the much more sparse data for the J=2-1 transition, as well as the ratios of the value determined in this paper to the literature value, their average, and their standard deviation. With one exception (J=1-0 AROKP), the standard deviations are all between 0.22 and 0.31.

These standard deviations represent the combined error of the isotopologue ratio derived from the literature and our value. In both transitions, our data are derived from simultaneous dual-frequency measurements, which compared to the literature data have well-defined baselines and relatively high S/Ns so that their contribution to the listed standard deviations is substantially below that of the literature values.

Appendix C: CO radiative transfer modeling

Our modeling assumes that the measured intensities are described by two distinct model gas phases. As noted in Section 5, this is an oversimplification, but two phases is the most that is allowed by the present data without introducing major additional assumptions. We preferred to fit the more diagnostic and more accurate ^{12}CO-to- ^{13}CO ratios, and we assumed that both phases have the same isotopological abundance. The modeling was accomplished by searching a grid of line intensity ratios resulting from the superposition of two model gas clouds with kinetic temperature T_k between 10 K and 150 K, densities n_{H_2} between $10^2\,\mathrm{cm^{-3}}$ and $10^5\,\mathrm{cm^{-3}}$, and CO velocity gradients $N(CO)/\mathrm{d}V$ between $6\times10^{15}\,\mathrm{cm^{-2}}/\,\mathrm{km\,s^{-1}}$ and $1\times10^{18}\,\mathrm{cm^{-2}}/\,\mathrm{km\,s^{-1}}$ for ratios matching the observed set, with the relative weights of

Table A.2. Galaxy center line intensities from JCMT, IRAM, and HHSMT

NGC IC	CO(2-1)			CO(3-2)			
	TP[a] J22"	B93[b] I22"	Ratio	TP[c] J22"	D01[c] H22"	M10[c] H22"	Ratio
(1)	(2)	(3)	(4)	(5)	(6)	(7)	(8)
253	1360	...	...	850	680	...	1.25[f]
278	19.6	17	1.15	14.0	15	...	0.93[f]
628	4.2	1.8	2.33	2.7	...	...	...
660	149	112	1.33	94.0	...	71.1	1.32
891	61.6	86	0.72	...	71	17.3	...
972	70.5	...	...	39.0	...	37.0	1.05
Maf2	247	...	...	179	139	157.1	1.14
1055	54.4	58	0.94	...	...	19.6	...
1068	239	240	1.00	101	...	116.0	0.87
1084	30.7	21	1.46	...	...	14.9	...
I342	173	...	...	121	148	...	0.82[f]
2146	164	138	1.19	137	172	66.9	0.80[f]
2559	69.7	...	...	40.3	...	37.3	1.08
2903	59.5	...	...	53.8	...	59.6	0.91
3034	657	...	...	548	770	1056	0.71[f]
3227	48.3	42	1.15	41.7	...	18.1	2.30
3310	8.7	9.5	0.92	11.7	...	6.9	1.64
3351	...	28	...	29.9	...	26.0	1.15
3627	74.3	77	0.96	48.7	...	33.4	1.46
3628	162	142	1.14	114	206	140.7	0.81
3690	64.4	...	...	40.3	...	36.4	1.11
3982	13.9	...	...	12.7	...	6.7	1.90
4038	63.6	...	...	52.0	...	44.0	1.18
4039	35	...	...	23.8	...	15.2	1.57
4258	44.3	...	...	32.7	...	64.4	0.51
4303	42.6	...	...	23.0	...	33.7	0.68
4321	55.6	57	0.98	35.3	...	56.9	0.62
4414	37.1	46	0.81	18.7	...	37.6	0.50
4457	27.5	...	...	19.0	...	20.3	0.94
4565	10.1	9	1.12	...	...	8.3	...
4631	34.3	...	...	23.2	37	17.7	1.31
4666	53.1	...	...	35.3	...	36.7	0.96
4736	42.7	...	...	27.4	...	21.3	1.29
4826	102	...	...	49.9	...	86.8	0.57
5033	42.5	33	1.29	24.1	...	16.7	1.44
5194	54.2	...	...	31.7	47	44.4	0.71
5236	251	...	...	137	234	153.9	0.89
6240	70.2	...	...	80.4	...	74.9	1.07
6946	240	...	...	117	129	132.3	0.88
7331	15.5	19	0.82	7.1	...	7.2	0.99
7469	52.0	...	...	40.7	...	35.2	1.16

Notes: [a]: This paper, measured JCMT intensities; [b]: Braine *et al.* (1993a) convolved IRAM intensities; [c]: This paper, convolved JCMT intensities; [d]: Dumke *et al.* (2001) peak intensities in HHST maps; [e]: Mao *et al.* (2010), measured HHST intensities; [f]: Ratio based on Dumke *et al.* (2010) intensity

the two as a free parameter. This parameter space contains the full range of physical conditions, from translucent gas to dense clouds, that the ^{12}CO and ^{13}CO transitions included in this paper are expected to distinguish. Because we consider only the lower J ^{12}CO and ^{13}CO transitions, our models lack sensitivity to molecular gas at the very high densities and temperatures that are sampled by the higher CO transitions or by molecular species such as HCN or HCO$^+$. Measurements of ^{12}CO and ^{13}CO at higher J would provide more information on very high-pressure molecular gas but would not add much to the present model results on the cooler and less dense lower-pressure gas of which the bulk of the molecular ISM consists.

Table A.3. Statistics of the line intensity comparisons[a]

Line	CO(1-0)	CO(1-0)	CO(2-1)	CO(3-2)
Telescope	SEST SEST	IRAM IRAM	JCMT IRAM	JCMT HHSMT
Beam size	S:S 45"	I:I 22"	J:I 22"	J:H 22"
(1)	(2)	(3)	(4)	(5)
Average	0.95	1.04	1.13	1.05
SD	0.31	0.29	0.37	0.43
n	43	27	17	36

Note: [a] Average: average ratio of value from this paper over literature values in same beam; SD: standard deviation; n: number of values in the average

Residual degeneracies occur in the majority of galaxies modeled and the observed ratios can usually be fit with a range of comparable solutions. Thus, the model solutions obtained are not unique but instead only constrain values to limited regions of parameter space. This is illustrated in Table C.1 where we show the search results for a few galaxies. Although each of the solutions is acceptable, individual fit parameters sometimes vary considerably. However, these variations are not independent and the final beam-averaged column densities resulting from the combination of the two phases normalized by the observed CO(2-1) line intensity is much less variable. The highest and lowest value differ by a factor of two or less, and dispersions are typically 30% or less.

In Table C.2 we list the model solution that was closest to the observations, even when other model ratios were only marginally different and within the observational error; for examples, again see Table C.1. We rejected solutions in which the denser gas component is also hotter than the more tenuous component because we consider the large pressure imbalances implied by such solutions physically implausible, certainly on the observed kiloparsec scales. Table C.2 gives the model H$_2$ gas volume densities $n_{\rm H_2}$ and kinetic temperatures $T_{\rm k}$ for each of the two phases as well as their relative contributions f_1:f_2 = f_{12} to the observed J=2-1 ^{12}CO intensity. Because of the residual degeneracy in the two-phase modeling, kinetic temperatures and gas densities are uncertain by factors of two and three, respectively. Moreover, because our analysis is limited to the lower three ^{12}CO and ^{13}CO transitions (only 14 galaxies were also observed in J=4-3 ^{12}CO), we cannot meaningfully distinguish temperatures above 100 K or densities above 10^4 cm^{-3}, even though our analysis may formally do so. The results in Table C.2 must therefore be taken as representative rather than individually accurate.

Notwithstanding this reservation, successful fits at either abundance generally suggest modest kinetic temperatures well below 100 K, typically between 20 K and 30 K for the densest phase, usually with densities above 3000 cm^{-3}. The less dense phase exhibits greater variety in temperature and density. In most galaxies, two-thirds or more of the J=2-1 ^{12}CO emission come from a single gas phase, often at relatively low kinetic temperatures of 10-30 K. Overall, no more than one-third of the detected J=2-1 ^{12}CO emission is contributed by high-density (n > 3000 cm^{-3}) gas. About one-third of the observed galaxies can be modeled with only a difference in density between the two phases, and another one-third with only a difference in temperature. The variation in molecular gas suggested by our modeling even in apparently similar galaxies will at least partly reflect the rapidly changing state of the molecular gas in galactic centers as a function of inflow and outflow rates, as well star formation and AGN activity. Each of these processes may significantly influence the balance of central gas phases in any particular galaxy on timescales much shorter than the Hubble time.

Appendix D: Hydrogen amount

Appendix D.1: H column density and mass

Total hydrogen column densities $N_{\rm H}$ would follow directly from the carbon column densities $N_{\rm C}$ if the gas phase carbon-to-hydrogen abundance were directly known, which is not the case. Instead, we must infer this abundance from our knowledge of (i) the relative oxygen abundance [O]/[H], (ii) the relative carbon abundance [C]/[O], and (iii), the fraction δ_C of all carbon that is in the gas phase rather than locked up in dust grains.

Optical spectroscopy of disk HII] regions has yielded oxygen abundances that are expressed as metallicities 12+log(O/H) for various galaxies. The results for 34 galaxies from our sample are summarized in Col. 4 of Table D.1. They are taken from the compilations of extragalactic HII region abundances by Vila-Costas & Edmunds (1992) and later publications based on similar methods (references given in the table) [7]. Unfortunately, individual measurements of HII regions in galaxy centers may suffer errors of up to factors of two. Frequently, no suitable HII regions occur in the very center of a galaxy. In these cases, central metallicities are deduced from a linear extrapolation of metallicity gradients to zero radius, but the non-negligible dispersion of individual abundances causes relatively large errors in the slopes of the metallicity gradient. In addition, there is some evidence that these gradients flatten at small radii so that linear extrapolations to zero radius overestimate the central metallicity. The data in Table D.1 define a mean zero-radius abundance 12+log(O/H)=9.2±0.2, which is three times the solar neighborhood metallicity. However, in view of the uncertainties involved, we consider an intermediate metallicity twice solar to be more reasonable. This implies an elemental ratio $[O]/[H] = 10^{-3}$, which we consider uncertain by a factor of one and a half.

The relation of carbon to oxygen, the carbon abundance [C]/[O], has been investigated at solar metallicity and below by various authors (e.g., Kobulnicky & Skillman, 1998; Garnett *et al.* 1999, 2004; Esteban *et al.* 2014, Berg *et al.* 2016). From solar metallicity downward, [C]/[O] drops linearly proportional to [O]/[H] to a metallicity of about a tenth solar and then flattens. The few available data suggest equal [C]/[H] and [O]/[H] abundances at metallicities just above solar. It is unlikely that the trend observed at subsolar abundances can be extrapolated much farther as this would quickly lead to unrealistically high carbon fractions. Accordingly, we assume equal carbon and oxygen abundances at supersolar metallicities, so that $[C]/[H] \approx 10^{-3}$.

A final source of uncertainty is the carbon-depletion factor $\delta_{\rm C}$. In galaxy disks, as much as two-thirds of all carbon may be tied up in dust particles, rendering it unavailable for the gas phase (see Jenkins, 2009). However, turbulence and shocks may cause substantial dust grain erosion in galaxy centers, leading to a higher carbon gas fraction. It is thus reasonable to adopt a depletion factor $\delta_{\rm C} = 0.5 \pm 0.2$. Taken together, these three considerationsC suggest that the best result is obtained with an intermediate 'nominal' (N) phase ratio $N_{\rm H}/N_{\rm C} = (2 \pm 1) \times 10^3$.

In Table D.1 we present the beam-averaged total hydrogen column densities $N_{\rm H}$ based on this nominal gas-phase carbon ratio (columns headed 'N'), which is taken to be the same for all galaxies unless otherwise noted. We present results for isotopologue ratios of 40 and 80, respectively, denoted by superscript. For comparison, we also list column densities ('E') assuming the individual extrapolated high gas-phase carbon abundance from Col. 5 to apply, as well as column densities ('G') assuming for all galaxies the same low solar neighborhood gas-phase carbon abundance. The 'E' and 'G' columns represent the extreme lower and upper limits.

Only the extrapolated case E total hydrogen column densities $N_{\rm H}$ in Table D.1 are based on individually determined carbon abundances; they have a dispersion of 0.09, corresponding to a factor 1.25. The case N as well as case G values are based on a fixed value for the whole sample. We assume that these are characterized by the same dispersion as case E. The mean values of the beam-averaged case N column densities for isotopological abundances of 40 and 80 differ by a factor of 1.6, thus introducing an error of 27% in the combined data set. Taking into account the uncertainty in the beam-averaged carbon column densities themselves (see Section 6.1), we find a combined uncertainty in each derived set of hydrogen column densities slightly over a factor of two.

The final uncertainty lies, however, in our choice of the assumed metallicity-dependent carbon abundance. We chose a nominal value (N) for $N_{\rm H}$ that is on average a factor of four higher than the extrapolated value (E) and is by definition a factor of three lower than the Galactic value (G) in Col. 3. This is a collective rather than an individual uncertainty, however.

Appendix D.2: H_2 *column density*

The column density of molecular hydrogen $N(H_2)$ follows from that of total hydrogen N_H after subtraction of the neutral hydrogen contribution N(HI). In Col. 9 of Table D.1 we list the HI column densities from the literature at resolutions similar to those of the normalized CO beam used in this paper; almost all were originally obtained with either the Westerbork Synthesis Radio Telescope (NL) or the Very Large Array (USA). Most of the HI column densities are relatively low. The few high values originate in strongly tilted galaxies where the long lines of sight include gas at large radii. Maps show that the distributions of CO and HI in galaxies are anticorrelated: CO usually peaks in the center where HI maps frequently exhibit clear central holes. For galaxies with $b/a \geq 0.6$, we took the actual N(HI) values from Col. 9, and for tilted galaxies with $b/a < 0.6$ as well as those where no HI data were found, we set N(HI) to 0.5×10^{21} cm^{-2}, the average for the galaxies with $b/a \geq 0.6$.

Beam-averaged molecular hydrogen column densities assuming nominal abundances are listed in Table D.1 for the two isotopological abundances. The values in Cols. 10 and 13 are corrected for the contribution of HI. We did not separately list uncorrected column densities as these are just the values in Col. 8 divided by two. For most galaxies, the HI contribution is minor, typically 15%. In a recent study, Gerin & Liszt (2017) reached an almost identical conclusion for the inner Milky Way ($R < 1.5$ kpc) using a completely different line of reasoning.

For carbon abundances as low as those of the Solar Neighbourhood (case G), the HI contribution is in fact negligible (typically $\leq 5\%$). However, if the carbon abundances were as high as suggested by the full extrapolation of the abundance gradients (case E), the total hydrogen column densities would be reduced to the levels of HI. This would leave no room for molecular

---

[7] Some studies (cf. Pilyugin *et al.* 2012, 2014) derive abundances that are systematically lower by a factor ~2.5. See the discussion by Peimbert *et al.* 2017

hydrogen, implying improbably high CO emissivities as well as improbably low gas-to-dust ratios. The high case E carbon abundances are therefore ruled out unless almost all carbon is in dust and very little in the gas phase. This is not expected in (dynamically) active environments such as galaxy centers.

The errors in the derived $N(\mathrm{H_2})$ values are almost identical to those discussed in the preceding section: about a factor of 2.5 for for the nominal (N) case and slightly less for the low abundance (G) case. This level of uncertainty is similar to the systematic uncertainty represented by the difference between the two cases.

Funally, we derived the CO-to-$\mathrm{H_2}$ conversion factors $X = N(\mathrm{H_2})/I_{\mathrm{CO}(1-0)}$ for the nominal carbon abundance with and without HI subtraction for each of the two isotopologue abundances considered. The real but relatively small effects of HI correction and isotopologue abundance are illustrated by Cols. 12 and 13 in Table D.1.

Table B.1. Detailed comparison of J=1-0 ^{12}CO/^{13}CO

NGC/IC	This	Telescope[a] and beam-width (arcsec)								Reference
	Paper	BTL	NRAO	AROKP	FCRAO	PMO	SEST	OSO	IRAM	
	22	100	55	55	45	45	45	33	22	
(1)	(2)	(3)	4)	(5)	(6)	(7)	(8)	(9)	(10)	(11)
253	12.7	11.4	16.6	...	11.9	...	...	...	...	4
278	9.0	...	...	11.3	...	...	...	...	...	28
520	14.2	...	...	...	...	...	...	11.5	...	10
628	6.3	...	6.7	10.8	...	...	...	...	9.9	8,28,31
660	14.0	...	...	...	...	...	...	14.0	16.5	6/10,26
891	7.8	...	8.4	9.9	...	...	...	...	8.5	8,28,19
1068	11.8	...	...	...	13.4/10.7	...	...	...	14	11,4,1
Maf2	8.6	...	9.0/8.2	...	...	...	...	...	...	8/12
I342	10.2	11.0	11.1/16.0	...	8.4/8.7	...	...	...	...	13,8/12,4/11
1365	11.1	...	6.4	...	...	...	...	...	13	23,5
1614	30.0	...	...	...	...	...	>26	...	29.4	10,26
1808	16.5	...	...	...	...	...	16.4	...	...	6/10
2146	15.0	...	...	...	14.9	...	...	12.2	...	4,6/10
2369	14.9	...	...	...	...	...	15	...	...	6
2903	11.2	...	9.5	11.3	12.8	...	...	...	12.3	8,28,2,31
3034	18.4	...	15.9	...	27.3	21.9	...	...	14.3	8,4,2,25
3044	13.5	...	...	6.3	...	...	...	...	...	28
3079	15.8	...	...	...	15.3	...	...	10.9	17.1	4,6/10,26
3227	17.8	...	...	...	...	...	...	...	17	5
3256	25	...	...	...	...	...	35/26	...	...	6/8/10/7
3556	12.5	...	...	14.3	8.7	...	...	...	12.5	28,4,26
3593	12.4	...	...	...	10.6	...	...	...	...	4
3627	13.3	...	10	...	11.2	10.4	...	...	15.2	8,4,2,31
3628	12.0	...	8.2	...	9.2	11.1	...	...	...	8,4,2
4030	6.6	...	...	7.7	...	...	...	...	...	28
4038	12.8	...	...	...	...	...	16	...	11	6,16
4039	22.0	...	...	...	...	...	19	...	...	6
4051	18	...	...	...	...	...	...	...	13/16.7	5/29
4254	8.9	...	...	11.5	...	...	...	...	8.4	31
4321	9.3	...	...	...	7.6	...	...	...	10.9	11,31
4414	7.5	...	6.3	...	...	...	...	...	9	18
4527	13.3	...	...	11.3	6.1	...	...	...	...	4,28
4631	15.1	...	...	...	16.3	10.5	...	...	11.5	4,2,19
4666	9.7	...	...	10.5	...	...	...	...	...	28
4736	9.9	...	8.3	...	...	7.2	...	...	...	8,2
4826	8.3	...	5.3	...	...	...	...	5.1	...	8,6/10
5033	9.1	...	...	...	...	...	...	9.3	8/8.4	6/10,5/29
5055	6.2	...	...	7.2	5.7	7.7	...	6.2	7.2	28,4,2,6/10,31
5135	23	...	...	...	...	...	...	...	26	5
5194	6.7	15.9	6.5	...	5.4/10.4	8.5	...	...	...	13,12,4/11,2
5236	13.7	15.8	13.1	...	11.0	...	...	...	...	13,12,11
5775	9.1	...	...	13.0	...	...	...	...	...	28
6221	12	...	...	...	...	...	18	...	...	6
6240	29	...	...	...	...	...	44	...	28.8/45	8,26/1
6764	19	...	...	...	...	...	...	...	11/17	5/20
6946	13.7	...	11.8/11.1	...	15.0/17.0	...	...	...	15.2	12/8,11/4,31
7469	17	...	...	...	...	...	...	...	20.8	26
7541	8.2	...	...	15.1	...	...	...	...	...	28
7552	10.8	...	...	...	...	...	14.2	...	...	6
7771	13.9	...	...	...	...	...	...	...	13.6	26

Notes: [a] BTL: Bell Telephone Labs; NRAO: Kitt Peak millimeter telescope operated by National Radio Astronomy Observatory; AROKP: Kitt Peak millimeter telescope operated by Arizona Radio Observatory; FCRAO: Five Colleges Radio Astronomy Observatory; PMO: Delingha Telescope operated by Purple Mountain Observatory; SEST: Swedish-ESO Submillimeter Telescope; OSO: Onsala Space Observatory; IRAM: Institut Radio Astronomie Millimétrique - Pico Veleta

Table B.2. Literature comparison of J=2-1 ^{12}CO/ ^{13}CO

NGC (1)	This Paper (2)	Lit. Value (3)	Ratio 4)	Telescope[a] (5)	Ref (6)
660	17.0	21.8	0.78	O	6,10
1068	12.8	10	1.28	J	1
1365	11.5	10/13	0.98	J/SMA	5/22
1808	12.6	15.5	0.81	S	6,10
2146	8.7	9.9	0.88	O	6,10
3034	10.8	11.9	0.91	J	24
3034	14.3	11.3	1.29	I	25
3227	13.5	25	0.54	J	5
3256	16	10/21/23/17	0.90	S/SMA	6,10,8/27
4039	12.9	12.0	13/13/10	C/J/I	3/15/16
4038	15.8	19.8	27/16/16	C/J/I	3/15/16
4051	21	14	1.50	J	5
4414	8.5	9	0.94	I	18
4736	10.1	13.6	0.74	C	3
4826	5.1	5.3	0.96	O	6,10
5033	8.3	6	1.38	J	5
5135	9.1	13	0.70	J	5
6240	40	53	0.75	J	1
6764	24	15	1.60	I	20
7331	6.2	6	1.03	I	29
7469	17	15	1.13	J	5

Notes: [a] S: Swedish-ESO Submillimeter Telescope (SEST); O: Onsala Space Observatory (OSO); I: Institut Radio Astronomie Millimétrique - Pico Veleta (IRAM); J: James Clerk Maxwell Telescope (JCMT); C: Caltech Submillimeter Telescope (CSO) SMA: Smithsonian Millimeter Array

Table B.2. continued

References to Tables B.1 and B.2 1. Papadopoulos *et al.* 2012; 2. Tan *et al.* 2011; 3. Glenn & Hunter 2001; 4. Paglione *et al.* 2001; 5. Papadopoulos *et al.* 1998; 6. Aalto *et al.* 1995; 7. Garay *et al.* 1993; 8. Casoli *et al.* 1992; 10. Aalto *et al.* 1991; 11. Young & Sanders 1986; 12. Rickard & Blitz 1985; 13. Encrenaz *et al.* 1979; 15. Zhu *et al.* 2003; 16. Schulz *et al.* 2007; 18. Braine, Combes & van Driel, 1993b; 19. Golla & Wielebinsky, 1994 20. Eckart *et al.* 1991; 21. Sakamoto *et al.* 1997; 22. Sakamoto *et al.* 2007; 23. Sandqvist *et al.* 1988; 24. Petitpas & Wilson 2000; 25. Mao *et al.* 2000; 26. Costagliola *et al.* 2011; 27. Sakamoto *et al.* 2014; 28. Vila-Vilaro *et al.* 2015; 29. Krips *et al.* 2010; 30. Muraoka *et al.* 2016; 31. Cormier *et al.* 2018.

Table B.3. J=1-0 ^{12}CO/ ^{13}CO comparison statistics

	J=1-0								J=2-1
Telescope[a]	BTL	NRAO	AROKP	FCRAO	PMO	SEST	OSO	IRAM	Div
Beam (”)	100	55	55	45	45	45	33	22	—
(1)	(2)	(3)	4)	(5)	(6)	(7)	(8)	(9)	(10)
Average[b]	0.83	1.13	0.92	1.11	1.09	0.86	1.22	1.00	0.99
SD	0.27	0.27	0.39	0.31	0.28	0.18	0.25	0.22	0.28
n	4	19	14	22	7	9	7	30	21

Notes: [a] BTL: Bell Telephone Laboraory (USA); NRAO: National Radio Astronomy Observatory (USA); AROKP: Arizona Radio Observatory Kitt Peak (USA); FCRAO: Five Colleges Radio Astronomy Observatory (USA); PMO: Purple Mountain Observatory (PRC) SEST: Swedish-ESO Submillimeter Telescope (Chile); OSO: Onsala Space Observatory (Sweden); IRAM: Institut Radio Astronomie Millimétrique (Spain) [b] Average of relative isotopologue ratios, i.e., values from Table 3 in this paper derived from literature values; SD: Standard deviation; n: number of values in average

Table C.1. Two-phase fitting: example

f1 (1)	n1 (2)	N1/dV (3)	T1 (4)	f2 (5)	n2 (6)	N2/dV (7)	T2 (8)	^{13}CO10 (9)	^{13}CO21 (10)	^{13}CO32 (11)	^{12}CO1 (12)	^{12}CO3 (13)	Mean T_{mb} (14)	Mean N/dV (15)	N(CO) 10^{17} cm^{-2} (16)
NGC 2903 $I_{CO(2-1)} = 59.5$ K km s^{-1}															
0.25	1e4	1e17	30	0.75	1e2	1e17	100	10.3	8.9	12.7	1.28	0.90	12.09	1.00	4.9
0.30	1e4	1e17	30	0.70	1e2	1e17	100	10.4	8.5	11.5	1.25	0.89	12.90	1.00	4.6
0.30	3e3	1e17	60	0.70	1e2	1e17	100	12.2	9.3	13.3	1.23	0.84	15.95	1.00	3.7
0.70	1e3	6e16	150	0.30	1e3	3e17	150	11.8	8.6	11.3	1.28	0.78	32.30	1.32	2.4
0.75	1e3	1e17	150	0.25	1e3	3e17	100	10.9	8.3	11.3	1.29	0.78	34.50	1.50	2.6
0.80	1e3	1e17	150	0.20	1e3	3e17	150	12.0	8.5	11.3	1.30	0.78	35.15	1.40	2.4
0.85	1e3	1e17	150	0.15	5e2	6e17	150	10.6	8.6	11.7	1.28	0.78	34.23	1.75	3.0
0.90	1e3	1e17	150	0.10	1e3	6e17	100	11.3	8.5	11.3	1.29	0.78	33.88	1.50	2.6
0.90	1e3	1e17	150	0.10	5e2	1e18	150	10.6	8.5	11.5	1.28	0.78	34.40	1.90	3.3
obs								11.2	8.6	12.5	1.34	0.91			
NGC 4736 $I_{CO(2-1)} = 42.7$ K km s^{-1}															
0.25	3e3	3e17	10	0.75	3e3	3e16	60	9.6	10.0	14.2	0.97	0.70	18.0	0.98	2.2
0.25	5e2	3e17	60	0.75	3e3	3e16	60	10.4	11.1	14.6	1.01	0.72	23.4	0.98	1.8
0.30	3e3	1e16	150	0.70	3e3	6e16	20	10.2	9.5	15.4	1.03	0.68	13.2	0.45	1.5
0.35	3e3	6e15	150	0.65	3e3	6e16	20	9.6	9.2	15.2	1.01	0.68	11.7	0.44	1.6
0.40	1e5	1e16	20	0.60	3e3	6e16	20	10.1	9.5	15.1	1.00	0.72	11.9	0.40	1.4
0.40	3e3	6e15	100	0.60	3e3	6e16	20	10.1	9.5	15.4	1.03	0.65	11.4	0.38	1.4
0.45	1e5	6e15	20	0.55	3e3	6e16	20	9.9	9.5	15.8	0.99	0.71	10.6	0.36	1.5
0.45	3e3	1e17	10	0.55	3e3	3e16	60	9.5	10.2	15.4	1.00	0.68	16.8	0.62	1.6
obs								9.9	10.1	14.9	0.98	0.63			
NGC 5033 $I_{CO(2-1)} = 42.5$ K km s^{-1}															
0.10	1e3	1e17	100	0.90	3e3	6e16	20	9.0	7.4	12.2	1.26	0.64	14.1	0.64	2.7
0.10	1e3	1e17	150	0.90	3e3	6e16	20	9.4	7.5	12.2	1.26	0.65	14.4	0.64	2.7
0.10	3e3	6e16	30	0.90	3e3	6e16	20	8.8	7.0	11.6	1.23	0.63	13.1	0.60	2.0
0.20	3e3	6e16	30	0.80	3e3	6e16	20	8.9	7.1	11.5	1.22	0.64	13.7	0.60	1.9
0.20	3e3	6e16	30	0.80	3e3	6e16	20	9.1	7.1	11.4	1.22	0.64	13.7	0.60	1.9
0.30	3e3	6e16	30	0.70	3e3	6e16	20	9.2	7.1	11.4	1.22	0.65	14.9	0.60	1.7
0.30	5e2	1e17	60	0.70	1e5	3e16	10	8.7	7.4	11.7	1.29	0.65	7.4	0.51	2.9
0.30	3e3	1e17	20	0.70	5e2	6e15	150	9.2	7.7	11.9	1.30	0.60	7.0	0.34	2.1
0.30	5e2	1e17	30	0.70	3e3	6e16	30	9.4	7.7	11.4	1.22	0.65	16.4	0.72	1.9
0.30	1e3	1e17	30	0.70	3e3	6e16	30	9.2	7.4	11.3	1.21	0.67	17.5	0.72	1.8
0.35	3e3	1e17	30	0.65	1e3	6e16	30	8.9	7.6	11.3	1.28	0.64	15.4	0.74	2.0
0.35	3e3	6e16	30	0.65	3e3	6e16	20	9.3	7.1	11.3	1.21	0.65	14.6	0.60	1.8
0.35	3e3	6e16	30	0.65	1e4	3e16	10	9.6	7.0	11.3	1.22	0.63	9.8	0.42	1.8
0.35	1e3	1e17	30	0.65	3e3	6e16	30	9.0	7.4	11.4	1.21	0.67	17.3	0.77	1.9
0.40	3e3	6e16	30	0.60	3e3	3e16	10	9.6	7.6	11.3	1.28	0.60	9.9	0.42	1.8
0.40	3e3	1e17	20	0.60	1e3	1e16	60	8.9	7.5	11.8	1.27	0.61	15.4	0.46	1.3
0.40	1e3	1e17	30	0.60	3e3	6e16	30	8.8	7.5	11.5	1.22	0.66	19.3	0.76	1.7
0.45	1e3	3e16	100	0.55	3e3	1e17	20	8.9	7.4	12.1	1.26	0.66	15.9	0.69	1.8
0.45	3e3	1e17	20	0.55	1e3	1e16	100	8.7	7.5	12.0	1.21	0.63	10.7	0.51	2.0
0.45	3e3	1e17	20	0.55	1e3	6e16	60	8.7	7.4	12.1	1.28	0.66	16.4	0.78	2.0
0.45	1e3	3e16	60	0.55	3e3	1e17	20	8.8	7.4	11.8	1.28	0.63	13.4	0.69	2.2
obs								9.1	7.2	11.7	1.25	0.57			

Note: The solution used in Table C.2 is marked in bold in the first column.

Table C.2. *RADEX* model results

Name	Size	$[^{12}CO]/[^{13}CO]=40$							$[^{12}CO]/[^{13}CO]=80$						
	d_{22}	n_1	T_1	n_2	T_2	f_{12}	$N(CO)$ 10^{17}	$\frac{[CO]}{[C]}$	n_1	T_1	n_2	T_2	f_{12}	$N(CO)$ 10^{17}	$\frac{[CO]}{[C]}$
	kpc	cm^{-3}	K	cm^{-3}	K		cm^{-2}		cm^{-3}	K	cm^{-3}	K		cm^{-2}	
(1)	(2)	(3)	(4)	(5)	(6)	(7)	(8)	(9)	(10)	(11)	(12)	(13)	(14)	(15)	(16)
253	0.4	3e3	60	3e3	150	15:85	38	0.23	1e4	20	3e3	60	15:85	94	0.37
278	1.2	1e5	20	1e2	150	50:50	2.3	0.39	...	...	...	...	...	...	...
470:	3.4	1e5	20	5e2	150	45:55	0.7	0.13	5e2	50	1e3	150	40:60	1.8	0.45
520	3.2	5e2	30	1e4	20	30:70	3.0	0.15	...	...	...	...	...	...	...
613	2.1	1e5	60	5e2	20	20:80	3.2	0.18	1e3	30	1e4	20	10:90	16	0.71
628:	1.1	3e3	20	1e2	30	50:50	4.8	0.60	...	...	...	...	...	...	...
660	1.3	1e5	60	1e2	80	10:90	9.4	0.16	1e5	100	1e2	100	15:85	37	0.72
891	1.0	1e5	20	5e2	20	10:90	5.0	0.14	...	...	...	...	...	...	...
908	2.1	1e5	30	1e2	20	15:85	5.0	0.42	...	...	...	...	...	...	...
972	2.4	1e3	60	1e4	20	30:70	2.1	0.23	3e3	20	3e3	30	10:90	6.3	0.37
Maf2	0.3	1e3	100	1e4	30	10:90	16	0.48	...	...	...	...	...	...	...
1055	1.4	1e5	20	5e2	20	10:90	6.0	0.23	...	...	...	...	...	...	...
1068	1.6	3e3	30	3e3	150	10:90	6.2	0.22	1e5	10	3e3	150	45:55	19	0.45
1084	2.0	1e4	20	3e3	60	90:10	0.9	0.30	1e5	10	3e3	30	25:75	3.1	0.39
1097:	1.8	1e5	60	1e2	60	15:85	9.4	0.26	1e5	60	1e2	60	30:70	44	0.76
1365	2.3	1e2	100	1e5	20	40:60	22	0.37	1e4	10	1e4	20	35:65	29	0.49
342	0.4	1e3	20	3e3	100	30:70	7.8	0.37	...	...	...	...	...	...	...
1482::	2.7	1e5	10	1e2	30	20:80	1.3	0.06	3e3	20	5e2	20	10:90	2.0	0.15
1614:	6.8	3e3	150	5e2	10	10:90	1.5	0.14	...	...	...	...	...	...	...
1792	1.6	1e4	10	1e4	20	15:85	3.6	0.51	...	...	...	...	...	...	...
1808	1.3	1e5	60	1e3	150	45:55	1.8	0.10	3e3	25	3e3	125	50:50	7.6	0.54
2146	1.8	1e3	150	1e5	10	40:60	5.3	0.21	3e3	60	1e2	100	40:60	13	0.36
2273:	3.0	1e3	30	1e3	150	10:90	0.8	0.19	1e3	60	1e5	10	15:85	1.7	0.55
2559	2.3	1e4	60	1e4	10	45:55	1.9	0.16	...	...	...	...	...	...	...
2623:	8.4	1e4	30	3e3	100	15:85	1.5	0.38	...	...	...	...	...	...	...
2903	0.8	1e3	100	1e3	150	10:90	2.7	0.38	1e3	150	1e2	150	10:90	7.3	0.33
3034	0.6	1e5	60	1e3	150	10:90	20	0.25	3e3	150	3e3	30	15:85	46	0.53
3044:	2.2	1e5	10	1e3	60	25:75	0.4	0.13	1e5	10	3e3	30	15:85	0.2	0.05
3079	2.2	1e5	100	1e2	30	10:90	8.3	0.14	1e3	60	3e3	20	10:90	11	0.45
3175	1.5	1e4	20	5e2	150	15:85	1.6	0.23	3e3	100	5e2	10	15:85	7.7	0.45
3227	2.2	3e3	60	1e4	60	20:80	0.8	0.21	1e4	50	1e5	10	15:85	2.1	0.35
3310	2.0	1e5	100	1e3	100	20:80	0.5	0.27	3e3	30	1e4	30	20:80	0.4	0.41
3504	3.0	1e2	60	3e3	60	40:60	3.5	0.44	3e3	30	3e3	30	25:75	3.4	0.34
3593	0.6	3e3	20	5e2	100	15:85	2.2	0.12	1e5	10	5e2	20	50:50	4.2	0.21
3627	0.7	1e5	20	5e2	30	45:55	3.7	0.37	1e5	10	1e3	60	40:70	6.5	0.59
3628	0.9	1e5	30	1e2	30	20:80	17	0.21	...	...	...	...	...	...	...
3690:	5.2	1e5	30	1e2	150	15:85	1.6	0.05	1e2	50	3e3	100	50:50	4.2	0.38
4030	2.8	1e4	20	3e3	10	30:70	2.4	0.20	...	...	...	...	...	...	...
4038	2.5	1e4	150	1e2	100	30:70	5.5	0.50	3e3	20	1e4	20	15:85	5.9	0.33
4039	2.5	3e3	60	5e2	100	25:75	0.7	0.09	3e3	60	5e2	100	15:85	1.7	0.19
4051:	1.4	...	...	...	...	...	...	...	1e2	50	5e2	20	10:90	3.9	0.23
4102	1.8	1e5	10	3e3	60	10:90	2.9	0.22	1e4	20	3e3	60	10:90	6.5	0.38
4254	4.2	1e5	10	1e4	20	15:85	3.6	0.51	...	...	...	...	...	...	...
4258::	0.9	...	...	...	...	...	...	...	1e5	10	3e3	30	25:75	2.0	0.22
4293	1.5	1e3	150	1e3	60	25:75	1.0	0.24	...	...	...	...	...	...	...
4303	1.5	3e3	10	3e3	30	50:50	1.1	0.12	1e5	10	3e3	20	30:70	2.5	0.23
4321	1.5	1e4	30	1e2	60	10:90	6.5	0.21	1e5	10	1e2	150	20:80	14	0.37
4414::	1.0	1e5	30	5e2	20	15:85	3.2	0.23	...	...	...	...	...	...	...
4457	1.4	...	...	...	...	...	...	...	1e4	60	1e2	100	20:80	5.3	0.59
4527	1.4	...	...	...	...	...	...	...	1e4	10	1e4	20	10:90	44	0.87
4536	3.3	1e2	100	3e3	100	45:55	2.2	0.20	3e3	100	1e5	10	40:60	3.2	0.35
4631	0.8	1e3	60	1e4	20	25:75	0.9	0.22	...	...	...	...	...	...	...
4666	2.9	5e2	100	5e2	100	10:90	3.3	0.22	3e3	30	5e2	30	25:75	5.4	0.34
4736	0.5	1e5	20	3e3	20	40:60	1.4	0.36	3e3	20	3e3	30	30:70	3.9	0.28
4826	0.4	1e5	10	3e3	100	35:65	6.5	0.47	...	...	...	...	...	...	...
4945	0.5	3e3	30	1e4	20	20:80	22	0.20	3e3	60	1e4	20	20:80	71	0.50
5033	1.8	3e3	30	3e3	20	25:75	1.9	0.21	...	...	...	...	...	...	...
5055	0.9	1e5	20	5e2	20	25:75	5.0	0.24	...	...	...	...	...	...	...
5135	6.1	...	...	...	...	...	...	...	3e3	30	1e5	10	25:75	1.8	0.20
5194	1.0	1e5	10	3e3	20	15:85	13	0.56	...	...	...	...	...	...	...
5236	0.4	1e4	20	3e3	60	40:60	5.9	0.19	...	...	...	...	...	...	...
5713	3.3	3e3	10	1e4	10	30:70	2.4	0.18	1e4	30	1e5	10	35:65	2.9	0.29

Table C.2. continued

(1)	(2)	(3)	(4)	(5)	(6)	(7)	(8)	(9)	(10)	(11)	(12)	(13)	(14)	(15)	(16)
5775:	3.1	1e3	100	1e3	20	20:80	0.20	1.8	...	...	...	...	...	...	...
6000:	3.3	3e3	60	3e3	30	50:50	0.17	1.9	3e3	100	1e5	10	25:75	0.29	4.6
6240	11.6	...	...	...	...	...	...	...	1e4	20	1e2	125	15:85	0.09	0.6
6746:	4.1	...	...	...	...	...	...	...	1e4	30	1e2	100	10:90	0.21	2.3
6946	0.6	1e3	60	1e4	20	20:80	0.22	6.8	1e5	10	1e4	20	20:80	0.53	29
6951	2.6	1e4	20	1e2	100	35:65	0.22	3.3	...	...	...	...	...	...	...
7331	1.5	1e5	10	1e2	150	15:85	0.61	9.8	...	...	...	...	...	...	...
7469	7.1	...	...	...	...	...	...	...	5e2	50	3e3	100	35:65	0.49	2.9
7541	4.0	1e5	10	1e4	30	10:90	0.83	16	...	...	...	...	...	...	...
7714:	4.1	3e3	10	3e3	60	45:55	0.22	0.2	...	...	...	...	...	...	...

Note: Column 1: Name; a single colon denotes that one of three isotopologue ratios is lacking, a double colon denotes that two are lacking; Col. 2: projected linear diameter (in kpc) of a 22" aperture at galaxy distance from Table 1; Cols. 3 through 9 contain two-phase modeling results assuming an intrinsic ^{12}CO/^{13}CO abundance of 40; Cols. 10 through 16 assume an abundance of 80 (see text). Columns 3 and 10: n_1 is the H_2 volume density of the first gas phase; Cols. 4 and 11: T_1 is the kinetic gas temperature T_k of the first gas phase; Cols. 5 and 12: n_2 is the H_2 volume density of the second gas phase; Cols. 6 and 13: T_2 is the kinetic gas temperature T_k of the second gas phase; Cols. 7 and 14: f_{12} is the relative contributions of gas phases 1 and 2 to the observed velocity-integrated J=2-1 ^{12}CO emission; Cols. 8 and 15: $\frac{[CO]}{[C]} = N(CO)/N_C$ is the fraction of all gas-phase carbon in CO. Columns 9 and 16: N_C is the beam-averaged column density of all gaseous carbon in units of 10^{17} cm^{-2}.

Table D.1. Physical parameters of molecular gas in galaxy centers

NGC	$\frac{[CO]}{[C]}$	N_C	Abundance		N_H			N_{HI}	N_{H_2}	M_H	$X=N_{H_2}/I_{CO}$		Ref
		(10^{17} cm^{-2})	O	C	(10^{21} cm^{-2})					(10^7 $M_\odot$)	(10^{19} cm^{-2}/ K km s^{-1})		
	40-80	40-80			E^{40}	G^{40}	N^{40}-N^{80}		N_h^{40}-N_h^{80}	N^{40}-N^{80}	N^{40}-N^{80}	N_h^{40}-N_h^{80}	
(1)	(2)	(3)	(4)	(5)	(6)	(7)	(8)	(9)	(10)	(11)	(12)	(13)	(14)
253	0.23-0.37	165-254	9.17	9.32	16	104	33-51	0.7	16-25	5-7	1.6-2.5	1.6-2.4	A,B,G,1,2
278	0.39 ...	6 ...	9.30	9.54	0.3	3.5	1.1 ...	1.1	...	...	2.7 ...	...	F,3,8
470	0.45 0.35	5-4	...	...	...	3.0	0.9-0.8	...	0.3-0.2	9-8	1.7-1.5	0.9-0.6	...
520	0.15 ...	20 ...	...	...	...	13	4.1 ...	abs	1.8 ...	31 ...	1.8 ...	1.6 ...	4
613	0.18-0.71	18-23	...	...	...	12	3.5-4.6	...	1.5-2.1	...	2.5-3.3	2.2-3.0	...
628	0.60 ...	8 ...	9.30	9.54	0.6	5.0	1.7 ...	0.3	0.7 ...	...	11 ...	9.9 ...	A,B,G,5
660	0.16-0.72	59-51	9.10	9.21	7.3	37	12-10	abs	5.7-4.9	17-15	3.8-3.3	3.7-3.2	F,6
891	0.14 ...	36 ...	...	...	...	23	7.1 ...	6.4	3.6 ...	9 ...	2.6 ...	2.4 ...	7
908	0.42 ...	12 ...	...	...	...	7.8	2.5 ...	...	1.0 ...	...	4.1 ...	3.4 ...	...
972	0.23-0.37	9-17	9.11	9.23	1.0	5.6	1.8-3.4	1.7	0.7-0.9	11-22	1.3-2.5	1.0-1.3	F,8
Maf2	0.48 ...	34 ...	...	...	...	22	6.8 ...	1.1	3.2 ...	1 ...	1.6 ...	1.4 ...	9
1055	0.23 ...	26 ...	9.16	9.30	..	16	5.2 ...	...	1.7 ...	...	2.5 ...	2.2 ...	G
1068	0.22-0.45	28-43	9.24	9.43	2.1	18	3.9-8.6	0.3	2.7-4.2	24-36	1.6-2.6	1.6-2.5	B,G,10
1084	0.30-0.39	3-8	...	...	...	1.9	0.6-1.6	...	0.1-0.6	...	1.0-2.7	0.3-2.0	...
1097	0.26-0.76	36-58	9.27	9.48	2.4	23	7.3-12	1.0	3.1-5.3	32-52	2.7-4.3	2.3-3.9	E,G,11
1365	0.37-0.49	60-59	9.08	9.18	7.9	38	12-12	0.1	6.0-5.9	73-72	2.3-2.3	2.3-2.3	A,B,G,12,13
I342	0.37 ...	21 ...	9.35	9.61	1.1	14	4.3 ...	0.3	2.0 ...	1 ...	1.3 ...	1.2 ...	A,G,14
1614	0.06-0.15	11 ...	...	...	...	6.6	2.1 ...	abs	0.7 ...	61 ...	2.4 ...	1.7 ...	15
1792	0.51 ...	7 ...	...	...	...	4.2	1.3 ...	0.7	0.4 ...	...	2.3 ...	1.5 ...	16
1808	0.10-0.54	18-14	...	...	...	11	3.6-2.8	abs	1.5-1.2	5-4	1.3-1.0	1.1-0.8	17
2146	0.21-0.36	25-37	...	...	...	16	4.9-7.4	1.0	2.2-3.2	16-23	1.2-2.0	1.2-1.7	18
2273	0.19-0.55	4-3	...	...	...	2.7	0.9-0.5	0.4	0.2-0.1	6-4	2.5-1.6	1.4-0.4	8
2559	0.16 ...	12 ...	...	...	...	7.7	2.4 ...	...	1.0 ...	10 ...	1.6 ...	1.3 ...	...
2623	0.38 ...	4 ...	...	...	...	2.7	0.8 ...	abs	0.2 ...	37 ...	2.3 ...	1.1 ...	15
2903	0.38-0.33	7-22	9.36	9.63	0.4	4.6	1.4-4.4	0.8	2.5-1.8	1-2	0.9-2.8	0.6-2.2	A,B,D,G,19
3034	0.25-0.53	79-87	9.19	9.37	6.7	50	16-17	abs	7.7-8.5	9-11	1.2-1.3	1.1-1.2	E,20
3044	0.13-0.05	3-4	...	...	...	1.9	0.6-0.8	...	0.1-0.2	...	2.7-3.5	0.7-1.5	...
3079	0.14-0.45	59-25	9.12	9.25	6.7	38	12-5.0	abs	5.7-2.3	36-15	2.5-1.1	2.4-0.9	F,21
3175	0.23-0.45	7-17	...	...	...	4.2	1.3-3.4	...	0.4-1.5	2-4	1.5-4.0	1.0-3.4	...
3227	0.21-0.35	4-6	9.18	9.34	0.4	2.4	0.8-1.2	abs	0.2-0.4	2-3	0.6-1.0	0.3-0.6	G,22
3310	0.27-0.41	2-1	8.96	8.98	0.3	0.9	0.3-0.3	0.8	0.2-0.1	1-1	4.5-2.6	2.6-1.3	F,G,23,24
3504	0.44-0.34	8-10	9.26	9.47	0.5	4.8	1.5-2.0	0.1	0.7-0.9	8-11	1.4-1.8	1.3-1.7	F,G,25
3593	0.12-0.21	18-20	...	...	...	11	3.6-4.0	...	2.6-1.8	1-1	2.9-3.2	2.6-2.8	...
3627	0.37-0.59	10-11	...	...	...	6.4	2.0-3.0	0.1	0.8-1.3	0.7-0.7	1.4-2.0	1.2-1.8	26
3628	0.21 ...	80 ...	...	...	...	50	16 ...	abs	7.7 ...	8 ...	3.9 ...	3.8 ...	27
3690	0.05-0.38	32-11	...	...	...	20	6.3-2.2	abs	2.9-0.9	...	4.6-1.6	4.5-1.4	28
4030	0.20 ...	12 ...	...	...	...	7.8	2.5 ...	...	1.0 ...	...	2.9 ...	2.4 ...	...
4038	0.50-0.33	11-18	...	...	...	6.6	1.5-3.6	0.8	0.7-1.4	8-14	2.3-3.8	1.4-3.0	29
4039	0.09-0.19	8-9	...	...	...	5.0	1.6-1.8	0.8	0.6-0.5	6-7	1.7-2.0	1.2-1.1	29
4051	... 0.23	... 17	...	...	...	...	... 3.4	0.3	... 1.6	... 4	... 7.7	... 7.0	30
4102	0.22-0.38	13-17	9.16	9.30	1.3	8.5	2.7-3.4	abs	1.1-1.5	7-9	1.8-2.3	1.5-2.0	F,31
4254	0.51 ...	7 ...	9.28	9.50	0.5	4.7	1.5 ...	0.8	0.3 ...	17 ...	1.7 ...	0.8 ...	A-E,G,32,33
4258	... 0.22	... 9	9.13	9.27	...	...	... 1.9	2.4	... 0.7	... 1	... 2.3	... 1.6	B,G,34
4293	0.24 ...	4 ...	...	...	...	2.6	0.8 ...	abs	0.4 ...	...	1.1 ...	1.0 ...	35
4303	0.12-0.23	9-11	9.35	9.62	0.4	5.5	1.7-2.2	0.4	0.7-0.9	2-3	1.6-2.0	1.3-1.7	A-D,G,32,33
4321	0.21-0.37	31-37	9.31	9.56	1.7	20	6.2-7.4	0.4	2.9-3.5	9-10	3.8-4.5	3.6-4.3	A-C,E,G,36
4414	0.23 ...	14 ...	...	...	...	2.1	0.7-...	2.0	1.2 ...	...	2.7 ...	2.3 ...	37
4457	... 0.59	... 9	...	...	...	11	3.5-1.8	abs	1.5-0.6	...	3.2-1.6	2.7 1.2	35
4527	... 0.87	... 50	...	...	...	...	... 10	...	....	... 13	... 4.9	... 4.6	...
4536	0.20-0.35	11-9	9.07	9.17	1.4	6.6	2.1-1.7	abs	0.7-0.5	14-12	1.7-1.4	1.1-0.8	E,32
4631	0.22 ...	4 ...	8.92	8.92	1.0	2.6	0.8 ...	4.6	0.2 ...	...	0.9 ...	0.4 ...	E,G,38
4666	0.22-0.34	15-16	...	...	...	9.4	3.0-3.2	...	1.3-1.4	...	2.6-2.2	1.7-1.9	...
4736	0.36-0.28	4-14	9.03	9.10	0.7	2.8	0.9-2.0	0.3	0.3-0.9	0.2-0.3	1.0-2.4	0.7-2.0	B,D,G,39
4826	0.47 ...	14 ...	8.98	9.04	2.6	8.9	2.8 ...	1.1	1.2 ...	0.3 ...	1.6 ...	1.3 ...	E,40
4945	0.20-0.50	108-141	...	...	...	65	36-22	abs	18-11	....	2.4-1.5	2.8-1.5	41
5033	0.21 ...	9 ...	9.18	9.34	0.8	5.4	1.7 ...	1.1	0.6 ...	3 ...	1.6 ...	1.2 ...	B,G,19
5055	0.24 ...	21 ...	9.45	9.78	0.7	13	4.2 ...	1.3	1.9 ...	2 ...	3.0 ...	2.7 ...	A,B,G,19
5135	... 0.20	... 9	...	...	...	...	... 1.8	...	... 0.7	... 43	... 4.6	... 1.8	...
5194	0.56 ...	24 ...	9.39	9.70	1.0	15	4.8 ...	0.1	2.4 ...	...	5.0 ...	4.9 ...	A,B,D,G 42
5236	0.19 ...	31 ...	9.24	9.45	2.2	20	6.2 ...	0.3	2.9 ...	0.7 ...	1.6 ...	1.5 ...	A,B,G,43
5713	0.18-0.29	14-10	9.07	9.17	1.9	8.6	2.9-2.0	...	1.2-0.8	0.4- 0.3	3.2-1.8	2.7-1.4	E
5775	0.20 ...	9 ...	...	...	...	5.7	1.8 ...	7.5	0.7 ...	11 ...	1.9 ...	1.4 ...	44

Table D.1. continued

(1)	(2)	(3)	(4)	(5)	(6)	(7)	(8)	(9)	(10)	(11)	(12)	(13)	(14)
6000	0.17-0.29	11-16	...	...	...	6.9	2.2-3.2	...	15-22	0.9-1.4	1.5-2.1	1.2-1.8	...
6240	... 0.09	... 7	...	...	...	...	... 1.5	abs	... 1	...	... 1.1	... 0.7	45
6746	... 0.21	... 11	...	...	...	...	... 2.2	...	...	... 0.9	... 4.9	... 3.9	...
6946	0.22-0.53	31-54	9.22	9.40	2.5	20	6.2-11	0.8	1-2	2.7-5.0	1.4-2.4	1.2-2.2	A,B,G,46
6951	0.22 ...	15 ...	...	...	...	9.5	3.0 ...	0.2	1 ...	1.4 ...	3.0 ...	2.7 ...	47
7331	0.61 ...	16 ...	9.22	9.40	1.3	10	3.3 ...	1.2	...	1.4 ...	21 ...	9 ...	B,G,48
7469	... 0.49	... 6	...	...	...	...	... 1.3	abs	...	... 0.3	... 2.5	... 0.6	15
7541	0.83 ...	19 ...	...	...	...	12	3.7 ...	0.7	...	1.5 ...	6.6 ...	5.4 ...	49
7714	0.22 ...	1 ...	...	...	...	0.7	0.2 ...	1.3	...	... ...	1.1 ...	... ...	50

Notes:
Abundances in Cols. 4 and 5 are 12+log[O]/[H] and 12+log[C]/[H], respectively. In Cols. 6 through 8, total hydrogen column densities were derived assuming a carbon dust grain depletion factor of 0.5. In Cols. 10 through 13, values marked with subscript h are derived with correction for the HI contribution in Col. 9 for galaxies with a tilt b/a ≥ 0.6; a contribution N(HI)=0.5×10^{21} (see section 7.2) was assumed for all other galaxies including those lacking HI data. Mass listed is total hydrogen mass; to obtain total gas mass, multiply by 1.35. I(CO) is taken from Table 2. E(xtrapolated) is the lower limit assuming the extrapolated carbon abundance from Col. 5; G(alactic) is the upper limit assuming solar neighborhood carbon abundances; N(ominal) is the most representative intermediate carbon abundance discussed in the text. The small galaxies NGC 3310, NGC 4631, and NGC 4826 have much lower abundances than the other galaxies; for these we set N equal to G. Superscripts ^{40} and ^{80} denote results for isotopological abundances [^{12}CO]/[^{13}CO] = 40 and [^{12}CO]/[^{13}CO] = 80, respectively.
Entries in Col. 17 are as follows:
Reference to HI data: 1. Lucero *et al.* (2015); 2. Puche *et al.* (1991); 3. Knapen *et al.* (2004); 4. Stanford (1990); 5. Shostak *et al.* (1984) 6. van Driel *et al.* (1995); 7. Swaters *et al.* (1997); 8. WHISP database, hhttps://www. astro.rug.nl/ whisp/ 9. Hurt *et al.* (1996); 10. Brinks *et al.* (1997); 11. Ondrechen *et al.* (1989b); 12. Ondrechen *et al.* (1989a) 13. Jörsäter & van Moorsel (1995) 14. Crosthwaite *et al.* (2000); 15. Hibbard *et al.* (20001); 16. Dahlem (1992) 17. Saikia *et al.* (1990); 18. Taramopoulos *et al.* (2001) 19. Wevers *et al.* (1986); 20. Yun *et al.* (1993); 21. Irwin & Seaquist (1991) 22. Mundell *et al.* (1995); 23. Mulder *et al.* (1995); 24. Kregel *et al.* (2001); 25. van Moorsel G.A. (1983); 26. Zhang *et al.* (1993); 27. Wilding *et al.* (1993); 28. Stanford & Wood (1989); 29. van der Hulst (1979)' 30. Liszt & Dickey (1995); 31. Verheijen & Sancisi (2001); 32. Warmels (1988); 33. Cayatte *et al.* (1990); 34. van Albada (1980); 35. Chung *et al.* (2009) 36. Knapen *et al.* (1993) 37. Braine, Combes & van Driel (1993b); 38. Rand (1994); 39. Mulder & van Driel (1993); 40. Braun *et al.* (1994); 41. Ott *et al.* (2001); 42. Tilanus & Allen (1991); 43. Tilanus & Allen (1993); 44. Irwin (1994); 45. Baan *et al.* (2007); 46. Tacconi & Young (1986); 47. Haan *et al.* (2008); 48. Bosma (1981); 49. Chengalur *et al.* (1994); 50. Smith & Wallin (1992).
References to abundance data: A: Vila-Costas & Edmunds, 1992; B: Zaritzky *et al.* C. Skillman *et al.*, 1996; D. Moustakas & Kennicutt, 2006; E. Moustakas *et al.*, 2010; F. Robertson *et al.*, 2013; G. Pilyugin *et al.*, 2014.